Physik - Department

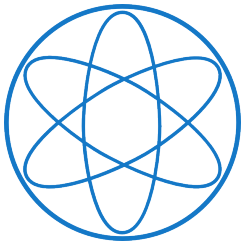

Lehrstuhl E12 für Experimentalphysik

A Calibration Experiment for the AGATA Pulse Shape Analysis

Diplomarbeit

Stefanie Klupp
29. April 2011

Technische Universität München

Abstract

In the near future, the AGATA spectrometer will play an important role in high resolution γ-ray spectroscopy. After the completion of the current Demonstrator phase, AGATA will consist of 180 highly segmented HPGe detectors covering nearly the full 4π solid angle. The main improvement of AGATA compared to currently existing γ-ray spectrometers is the ability to reconstruct γ-ray scattering paths to maximize the efficiency while keeping the very good peak to total ratio of arrays like Euroball or Gammasphere. The most important input of this so called γ-ray tracking are the γ-ray interaction points in the active germanium material which are determined by pulse shape analysis (PSA). The PSA is based on a comparison of the experimental signals to reference signals of a simulated pulse shape basis with known interaction points. Currently, it is implemented as a grid search algorithm and reconstructs one interaction point per segment, which corresponds to the energy weighted barycenter of all interaction positions in the segment.

In the scope of this thesis, an experimental method to determine the position resolution of the AGATA PSA for different signal bases was developed. This calibration experiment is based on the reconstruction of interaction points of annihilation γ-rays, detected in coincidence in two opposing AGATA crystals. The position resolution is extracted exploiting the fact that the 511 keV γ-rays are emitted back to back. For a quantitative determination of the resolution, the reconstructed interaction points were compared to the obtained interaction positions of a Geant4 based Monte Carlo simulation with adjustable position resolution which is based on two models: a Gaussian and a Laplace distribution. Different event selections allow studying the position resolution of single interaction points by selecting Compton scatterings of the 511 keV γ-rays from one segment into a neighboring segment as well as the resolution of the energy weighted barycenter using γ-rays which deposit their energy in a single segment for each crystal.

The concept of the calibration experiment was verified with experimental data using the first installed asymmetric triple clusters of the AGATA Demonstrator. A point-like ^{22}Na source provided the annihilation γ-rays from the positrons of the β^+-decay.

In the first test measurement the source was positioned in the center of the AGATA Demonstrator. Due to the symmetric setup, the mean position resolution of the two crystals A001 and A003 detecting the 511 keV γ-rays was determined for single interactions and barycenters for the two different signal bases ADL and JASS, currently used in AGATA. With a multi-parameter fit the position resolutions of individual crystals were extracted. All obtained position resolutions of the A001 and the A003 crystal fulfilled the requirements of AGATA (FWHM $<$ 5 mm for 1 MeV energy depositions). However, events featuring energy depositions in more than one segment of a crystal were found to have significantly worse resolutions due to the current implementation of the PSA algorithm.

The second test measurement was aimed at investigating the position resolution of a single crystal in more detail without using the multi-parameter fit. Thus, an asymmetric ^{22}Na source position was used to determine the position resolution of the A006 crystal independently of the resolutions of other detectors. To gain a deeper insight into the position resolution in different regions of the A006 crystal and its dependence on the used signal bases, the measurement was conducted with different source positions. Using single interactions in one segment of A006, position resolutions down to $\sigma = 1.0$ mm at 320 keV were obtained. Also local variations (σ = 1.0 - 2.6 mm) dependent on the signal bases ADL and JASS were quantified at 511 keV. Apart from that, it was shown that the position resolution for deposited energies between 100 and 300 keV is approximately inversely proportional to the square root of the energy.

Within the framework of this thesis it was demonstrated that the coincident detection of 511 keV γ-rays from β^+-annihilation is an appropriate and versatile tool to study the performance of the PSA in AGATA online. The method can not only be used in short breaks in between the experiments but also will allow for systematic investigations on spatial contributions to the position resolution and an optimization of the simulated signal bases.

Contents

Chapter 1

Introduction

In nuclear physics γ-ray spectroscopy is still one of the most powerful tools to study the single particle properties of the atomic nucleus. γ-rays carry important information about the nucleus which is essential not only for the validation of nuclear structure models. It is also exciting to search for new shell gaps far off the valley of stability, or in general to learn more about the interactions in the nucleus.

1.1 Challenges for γ-ray Spectrometers at Future Radioactive Beam Facilities

With new facilities like FAIR[1] in Germany or SPIRAL2 in France, beams of more and more exotic neutron to proton ratios already close to the regions of the r-process will be available at reasonable intensities. Hence, also astrophysical questions drive the development in γ-ray spectroscopy. In general, all experiments using those rare and expensive exotic beams have to be performed in inverse kinematics featuring a fast moving excited nucleus in the exit channel. Hence, all next generation γ-ray spectrometers have to fulfill three major requirements: a maximum of efficiency and resolution as well as a good position resolution for Doppler correction. Therefore, a European collaboration of ten countries decided to build the Advanced GAmma Tracking Array AGATA [1]. It is designed to meet the following demands which are necessary to achieve the ambiguous physics goals at future radioactive beam facilities. First of all, AGATA should have the maximum photopeak efficiency to ensure that most of the γ-rays are fully absorbed. This is especially important to detect even weak reaction channels. Therefore, a large amount of germanium with a full 4π coverage is desired. Furthermore, a good peak-to-total ratio P/T[2] is essential to identify weak channels in a γ-spectrum. To cope with high γ-ray multiplicities and with the immense background rate at high beam intensities, it is important that AGATA has a high granularity to detect individual γ-rays in different detection elements. The main challenge at FAIR will be that the exotic nuclei are moving with high velocities up to $\beta = 0.8$, $\beta = v/c$. Thus, the Doppler effect plays a crucial role as it results in shifted and broadened γ-ray lines in the γ-spectra of fast moving nuclei. The energy E_γ^{lab} of the γ-ray in the laboratory frame is given by a Lorentz transformation of the γ-ray energy E_γ^{rest} in the rest frame of the emitting nucleus [3]:

$$E_\gamma^{\mathrm{lab}} = E_\gamma^{\mathrm{rest}} \cdot \frac{1 - \beta \cos\theta}{\sqrt{1-\beta^2}}. \tag{1.1}$$

[1] FAIR: Facility for Antiproton and Ion Research

[2] The P/T ratio is defined as the ratio between the counts in the full energy peak and the total counts of a mono-energetic γ-ray spectrum [2].

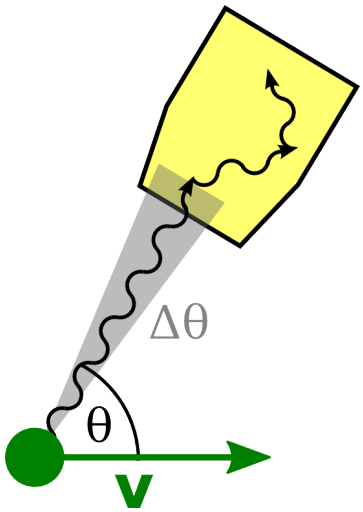

Fig. 1.1: Doppler effect. Due to the finite position resolution of the HPGe detector the direction of the incident γ-ray can only be determined with an accuracy of $\Delta\theta$. Thus, the γ-ray line in the spectrum is broadened according to eq. (1.2).

The angle θ corresponds to the emission direction of the γ-ray with respect to the velocity of the emitting nucleus in the laboratory frame (c.f. fig. 1.1). However, the emission direction of the γ-ray cannot be determined exactly leading to an error $\Delta\theta$. As a result, the γ-lines in the spectra are additionally broadened [3]

$$\Delta E_\gamma^{\text{lab}} = E_\gamma^{\text{rest}} \cdot \frac{\beta \sin\theta}{\sqrt{1-\beta^2}} \cdot \Delta\theta. \tag{1.2}$$

The angular resolution $\Delta\theta$ depends on the accuracy of the knowledge of the emission position of the γ-ray and the spatial resolution of its first interaction point in the germanium detector[3]. Hence, for a good Doppler correction of the γ-spectra, AGATA should be capable to determine the first interaction points of the γ-rays as precisely as possible. Thus, AGATA is based on the concepts of γ-ray tracking. This is a reconstruction of the full scattering path of each γ-ray hitting the detector. Hence, the first interaction point required for Doppler correction can be determined. Additionally, γ-ray tracking allows to add back the energy depositions of fully absorbed γ-rays and, therefore, feature the best possible P/T ratio. One important ingredient for the γ-ray tracking is the reconstruction of all γ-ray interaction positions with the corresponding energy depositions. This is done by a detailed analysis of the detected pulse shapes, the so called pulse shape analysis PSA (c.f. sec. 1.3). The scattering sequence is subsequently extracted using the interaction processes of γ-rays in the detector material germanium, namely photoelectric absorption, Compton scattering and pair production. As the Compton scattering is often dominating in the energy region of interest, the γ-ray tracking mainly exploits the Compton formula with a probabilistic approach [2]. In principle, the scattering angles obtained with the Compton formula are compared to the geometrical determined scattering angles obtained with the reconstructed interaction positions. Additionally, absorption probabilities are taken into account.

[3] An additional broadening of the γ-line is caused by the accuracy Δv of the velocity v of the nucleus.

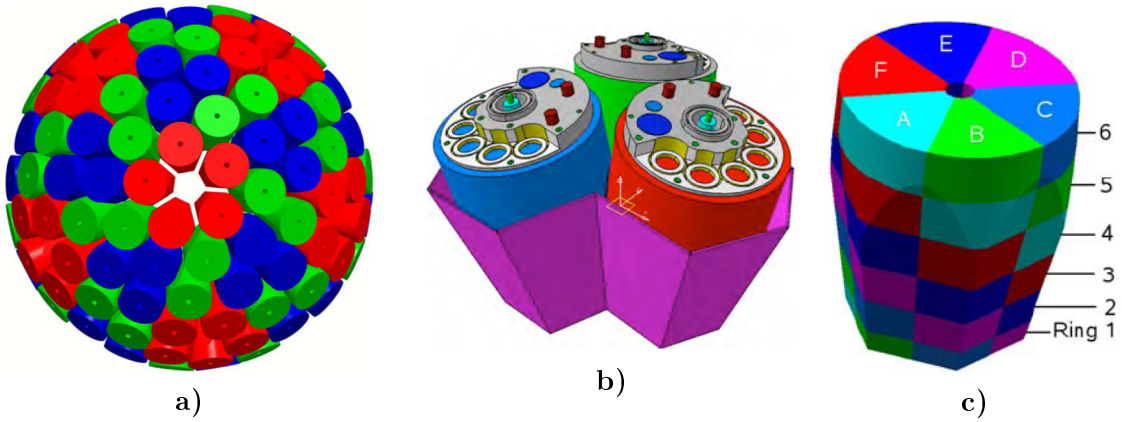

a) b) c)

Fig. 1.2: At its final state AGATA will consist of 180 coaxial HPGe detectors which are arranged on a 4π shell (**a**), [4]). The detectors are produced in three different shapes to receive a good angular coverage. The shapes are indicated with different colors: red, green and blue. Furthermore, always three different shaped crystals are stored in one cryostat forming a triple cluster (**b**), [3]). A single detector has a cylindrical shape with tapered sides leading to a hexagonal front. Additionally, every crystal is 36-fold electrically segmented (**c**), [5]).

1.2 The Advanced GAmma Tracking Array AGATA

AGATA is a 9 cm thick germanium shell which is divided into 180 hexagons and 12 pentagons. The hexagons correspond to 180 coaxial HPGe detectors. A schematic drawing of the AGATA array is shown in fig. 1.2 a). The 180 hexagonal shaped HPGe crystals are grouped in 60 triple clusters (ATCs[4]), each containing three slightly different tapered coaxial detectors (c.f. fig. 1.2 b)). Each crystal shape is labeled with a letter and a color: A-type crystals are red, B-type green and C-type blue. Three different shaped crystals are necessary to cover the maximum possible solid angle of up to 82 % of 4π with active germanium material [2].

AGATA crystals

All crystals have a length of (90 ± 1) mm, a diameter of $80^{+0.7}_{-0.1}$ mm and a tapering angle of about 8°. The core contact has a radius of 10 mm and a minimum distance of 13 mm to the crystal front. According to the specifications, the crystals are made of n-type HPGe with impurity concentrations ranging from 0.4 to $1.8{\cdot}10^{10}\,\mathrm{cm}^{-3}$. To protect the HPGe material, the crystals are encapsulated in a 0.8 mm thick aluminum can. Furthermore, they are electrically 36-fold segmented into six rows (1-6) and six sectors (A-F) (c.f. fig. 1.2 c)). The dimensions of the segments are adjusted to provide similar interaction probabilities in all segments. [6]

AGATA cryostats

One AGATA cryostat houses three different shaped crystals, thermometers for temperature control and the complete analog electronic. A transparent view is presented in fig. 1.3. The crystals at the front of the cryostat are cooled to 90 K to prevent thermal electron-hole excitations. Directly behind the crystals the cold part of the preamplifier is mounted in the same vacuum to minimize the noise contribution of the signals and to provide the best operational temperature for this FET of about 130 K. The warm part of the preamplifier is located outside the vacuum. Hence, it can be accessed easily. It is behind the transparent part in fig. 1.3, covered by the metal shield. Furthermore, an electronic shielding between the stages is included to keep the impact of crosstalk minimal. [2], [5]

[4] ATC: Asymmetric Triple Cluster

Fig. 1.3: Transparent view of an AGATA triple cryostat. At the front the three different shaped crystals in their aluminum encapsulation are situated. They are cooled to 90 K. Directly on the crystals the cold part of the preamplifier is mounted. The warm part of the preamplifier is located behind the metal shield. [5]

γ-ray multiplicity	1	10	20	30
Efficiency [%]	43.3	33.9	30.5	28.1
P/T [%]	58.2	52.9	50.9	49.1

Tab. 1.1: Predicted performance of the 4π AGATA array determined by Geant4 simulations for 1 MeV γ-rays [2].

Data processing

In the first stage, the signals of the 36 segments and the core signal of the preamplifiers are digitized with fast ADCs[5] at 100 MHz. Subsequently, the next units of digital electronics generate a trigger, extract the useful samples of the signals for the pulse shape analysis and determine the energy by a moving window deconvolution. Finally, a time stamp and an event number is assigned. Afterwards, the signals are sent to a PC server farm to reconstruct the interaction positions by PSA. These interaction points are then merged by the event builder to a single event. In this stage also the information of ancillary detectors can be included. Subsequently, the algorithms for γ-ray tracking are applied and the event is written to a mass storage device. All the software part of the data processing is managed by the Narval[6] tool [7]. [2], [6]

Predicted performance

The predicted performance of AGATA is summarized in tab. 1.1. It is expressed with the key parameters photopeak efficiency and peak-to-total ratio P/T. Note that the efficiency and the P/T values are obtained by Geant4 simulations and are strongly dependent on the performance of the reconstruction of the interaction positions and the capabilities of the γ-ray tracking algorithms [2]. Tab. 1.2 features a direct comparison of AGATA with important γ-ray spectrometers for a single 1 MeV γ-ray. Due to the large amount of germanium the photopeak efficiencies are significantly higher for AGATA and GRETA[7] than for any current existing arrays while the P/T ratios do not deteriorate by substituting the anti-Compton shields by the active germanium volume.

[5] Analog-to-Digital Converter

[6] Nouvelle Acquisition temps-Réel Version 1.6 Avec Linux

[7] The Gamma-Ray Energy Tracking Array GRETA is the corresponding project of AGATA in the USA which is currently under construction.

array	number of crystals	total granularity	photopeak efficiency	P/T
EUROBALL-III	239	239	9%	56%
GAMMASPHERE	110	∼170	9%	63%
AGATA Demonstrator	15	540	7%	7%
AGATA 4π	180	6480	43%	58%
GRETA 4π	120	4320	40%	53%

Tab. 1.2: Important quantities of γ-ray spectrometers for a 1 MeV γ-ray [6]. The Miniball array is not listed here as its performance differs due to the various possible arrangements.

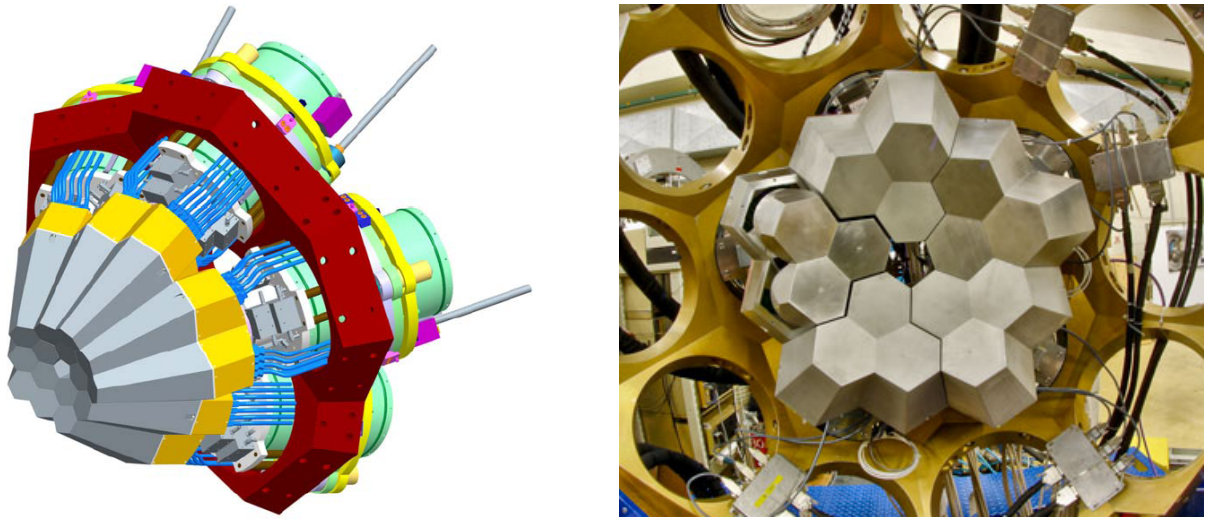

a) **b)**

Fig. 1.4: a) Schematic drawing of the AGATA Demonstrator. It consists of five triple clusters which are arranged around one pentagon. The support structure is shown in red and the LN_2 dewars in light green [5]. **b)** A photograph of the Demonstrator at its inauguration in April 2010 [8]. It displays four completed ATCs and one dummy ATC.

Status

Currently the AGATA Demonstrator, the first phase of the AGATA project, is completed. A technical drawing of the Demonstrator can be seen in fig. 1.4 a). It consists of five neighboring ATCs which are centered around a pentagon. Fig. 1.4 b) shows a photograph of the AGATA Demonstrator with four ATCs at its inauguration in April 2010 at Laboratori Nazionali di Legnaro (LNL) in Italy.

Up to now, 21 crystals have been delivered from Canberra, but six of them failed the acceptance tests due to too high leakage currents [9]. Furthermore, the line shapes of some detectors deteriorated after being exposed to a big neutron flux at the Laboratori Nazionali di Legnaro in July 2010. Therefore, they had to be annealed much earlier than planned to repair the crystal lattice. Currently, five triple clusters are operational and mounted in Legnaro, just being calibrated for the next experiments.

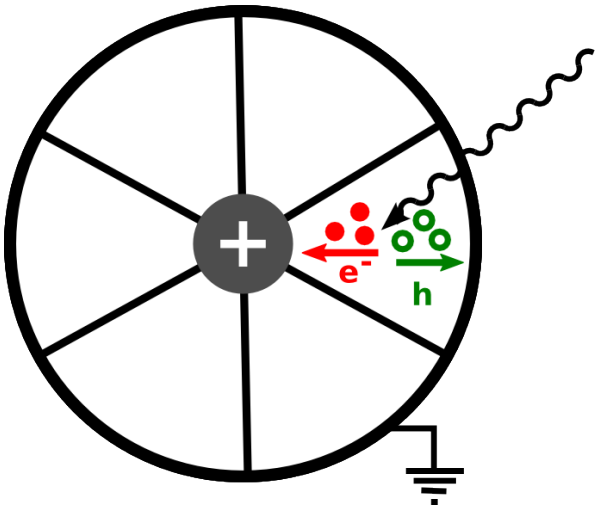

Fig. 1.5: Signal creation in a HPGe detector. If a γ-ray interacts with the germanium material a part or all of its energy is transferred to an electron, e.g. to the photo-electron or the Compton scattered electron. This electron decelerates in the crystal by producing electron-hole pairs. The electron-hole pairs are drifting due to the applied bias voltage to the detector electrodes. During the drift process the charge carriers induce mirror charges on the electrodes which form the signal.

1.3 Concept of Pulse Shape Analysis

The high photopeak efficiency and the good P/T ratio, stated in tab. 1.1, are based on the concepts of γ-ray tracking. As input for the γ-ray tracking algorithms the interaction points of the γ-rays are essential. They are obtained by a detailed analysis of the detected pulse shapes of the AGATA crystals. To understand the concept of pulse shape analysis, it is important to discuss the signal creation in HPGe detectors and their position dependence.

HPGe detectors

γ-rays interact via Compton scattering, photoelectric absorption or pair production with germanium. In all processes an electron is created which releases its energy by exciting electron-hole pairs in the semiconductor (c.f. fig. 1.5). The total number N_{eh} of the electron-hole pairs is proportional to the incident energy of the γ-ray if it is totally absorbed in the germanium crystal. Due to the small bandgap of about $E_{\text{gap}} = 0.7\,\text{eV}$ of germanium only about 3.0 eV are needed to create an electron-hole pair[8], resulting in a large N_{eh} [2]. Thus, statistical fluctuations are small leading to an excellent energy resolution of HPGe detectors. E.g. a fully absorbed 1.3 MeV γ-ray produces about $N_{eh} \approx 433\,000$ electron-hole pairs which, including the Fano factor of 0.3 [11], correspond to a line width of $\Delta E_\gamma = 1.2$ keV. Due to the applied bias voltage of about 4000 - 5000 V for AGATA detectors [12], the electron and the hole clouds separate. The electrons drift to the positive core while the holes drift to the outer segment contacts. While drifting both induce mirror charges on all electrodes which form the signal. On the charge collecting electrodes a net charge signal appears, whereas on the other electrodes the signal vanishes as soon as the drifting process is over. The latter signals are called transient signals.

[8] The mean excitation energy of an electron-hole pair is higher than the bandgap because phonons are excited, too [10].

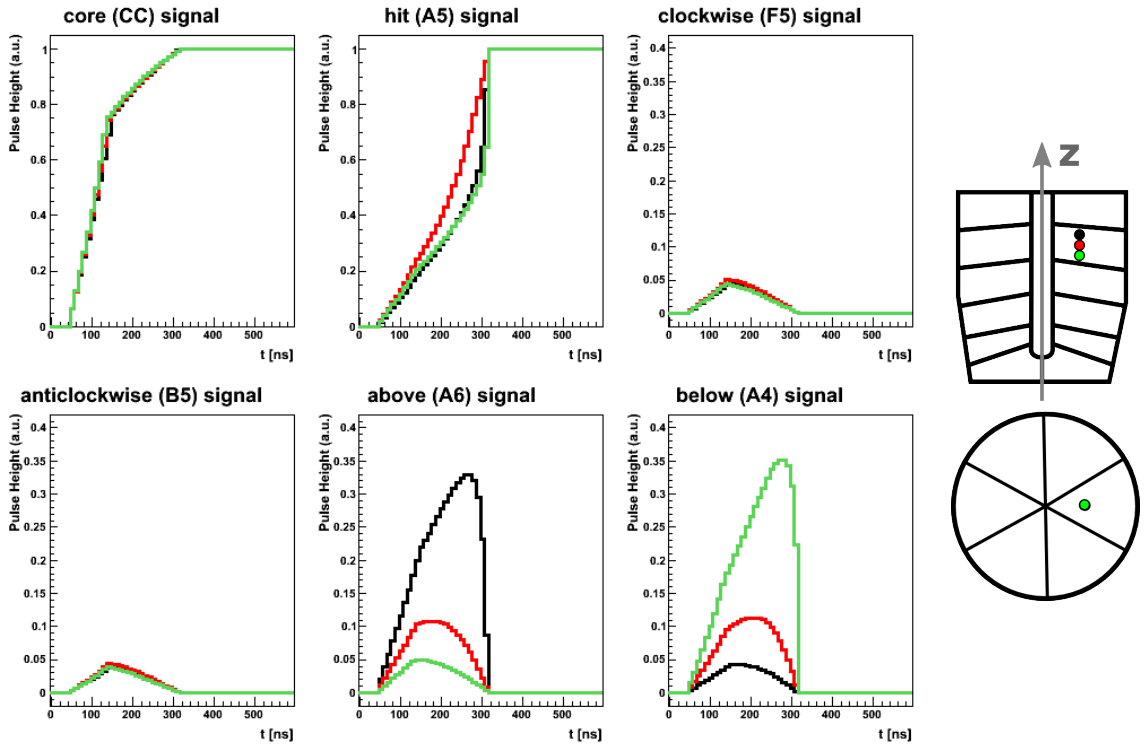

Fig. 1.6: Simulated pulse shapes from the JASS basis [6] for three different interaction points. They are marked with a black, a red and a green dot in the schematic AGATA crystal on the right. Comparing the pulse shapes for the different interaction points, a clear dependence of the their shape on the interaction position is visible.

Position dependence of pulse shapes

For a better understanding how these signals carry information about the γ-ray interaction position, fig. 1.6 shows the pulse shapes of three different interaction points. All interaction positions are located in the same segment. Thus, there are only two electrodes showing a net charge signal: the core and the segment A5 which contains the interaction points. The segments featuring a net charge signal are called hit segments. Additionally, the pulse shapes of the segments surrounding the hit segment are displayed. The signals in the clockwise and the anticlockwise segments all have the same shape as the three interaction points feature the same position in the x-y plane perpendicular to the z-axis. However, they differ in their z-coordinate leading to different signals in the segments above and below the hit segment. As an example, the black interaction point is located close to the upper segment boundary resulting in a huge pulse shape in the segment above and in a very weak signal in the far away below segment. The situation is the other way round for the green interaction point. In summary, the pulse shapes are characteristic for the γ-ray interaction position.

Pulse shape analysis: PSA

The most straight forward idea to extract the interaction positions from the measured pulses is to determine the interaction position from characteristic quantities. Typical candidates for these parameters are the rise-time and the amplitude of the signals. However, previous segmented HPGe detectors have shown that the achievable position resolutions are not sufficient for AGATA's physics goals. Hence, the AGATA collaboration has decided to use a more sophisticated method: The pulse shapes of all electrodes are calculated for a set of well defined

interaction positions in the AGATA crystal (c.f. sec. 1.4). As a result, a so called pulse shape basis is created[9]. Finally, these basis signals with known interaction positions are compared to the measured signals. This pulse shape analysis algorithms are based on a direct χ^2-like comparison. The minimal χ^2-value defines the interaction point. A more detailed discussion on the PSA algorithm is given in sec. 3.2.

1.4 Simulation of Pulse Shape Databases

The simulation of the pulse shapes consists of two steps: First, the trajectories $\vec{r}_{e,h}(t)$ of the electrons and the holes in the electric field of the AGATA detector are calculated. Second, the obtained trajectories are used to determine the induced mirror charges $Q_i(t)$ on the i^{th} electrode ($i = 1, \ldots, 36$ + core).

Calculation of the charge carrier trajectories $\vec{r}_{e,h}(t)$
In general, the trajectories $\vec{r}_{e,h}(t)$ of the drifting electrons and holes are given by their drift velocities $\vec{v}_{e,h}$ in the crystal lattice

$$\vec{r}_{e,h}(t) = \int_{t(\gamma\text{-ray int. point})}^{t(\text{charge coll. electrode})} dt \;\; \vec{v}_{e,h}(\vec{r}_{e,h}(t)) \; . \tag{1.3}$$

The trajectories start at the γ-ray interaction point and end at the charge collecting electrode, i.e. the core for the electrons and an outer contact for the holes. The drift velocity is challenging to calculate as it depends on the electric field $\vec{E}$ as well as on the electron and hole mobilities $\mu_{e,h}$ in the germanium crystal[10]

$$\vec{v}_{e,h}(\vec{r}) = \pm\mu_{e,h} \cdot \vec{E}(\vec{r}) \; . \tag{1.4}$$

The mobility tensors $\mu_{e,h}$ are anisotropic as they are defined by the band structure of the germanium crystal lattice. Hence, an exact knowledge of the crystal orientation is crucial in order to calculate the correct pulse shapes. The crystal axes of the AGATA detectors can be determined with the help of a ^{241}Am source by comparing the signal rise-times [13].
The electric field $\vec{E}$ in the AGATA detectors corresponds to the gradient of the potential ϕ

$$\vec{E}(\vec{r}) = -\nabla\phi(\vec{r}) \; . \tag{1.5}$$

The electric potential is determined by Poisson's equation

$$\phi(\vec{r}) = -\nabla^2 \frac{\rho(\vec{r})}{\epsilon_r \epsilon_0} \; , \tag{1.6}$$

where ϵ_0 and $\epsilon_r = 16$ are the permittivities of vacuum and germanium, respectively. $\rho(\vec{r})$ is the space charge distribution which results from the impurity concentration of the n-type HPGe material. It can be e.g. determined by measuring the capacity of the segments as a function of the bias voltage [14]. Due to the complex crystal geometry, leading to complex boundary conditions, the Poisson equation can only be solved numerically, e.g. with a Red-Black Gauß-Seidel solver [6]. An example of a resulting electric potential of an AGATA detector is visualized in fig. 1.7 a).

[9] At the beginning, the pulse shape bases were determined experimentally with scanning tables. However, this method is rejected as it is too time consuming and features a lot of systematic errors (c.f. chap. 2 and [6]).
[10] The sign in eq. (1.4) takes the different charge of the electrons and the holes into account.

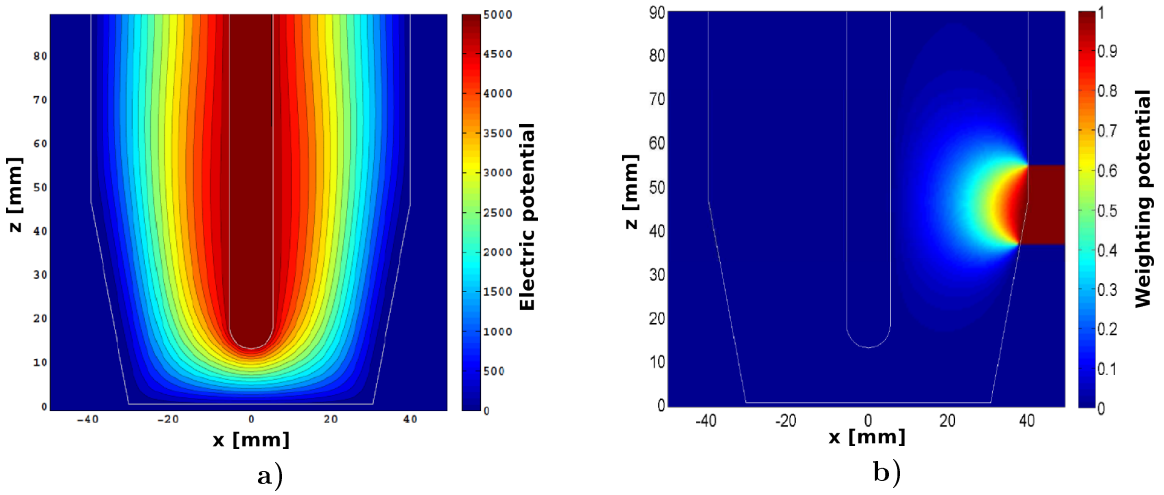

Fig. 1.7: Simulated electric potential (**a**)) and the weighting potential of segment E4 (**b**)) of a symmetric AGATA detector. The figures are similar to [6].

Calculation of the pulse shapes

Based on the trajectories of the electrons and the holes, the induced signals on all detector electrodes can be computed. The induced charge signal $Q_i(t)$ at the electrode i, caused by a point-like moving charge q, is given by Shockley-Ramo's theorem [6]

$$Q_i(t) = -q \cdot \psi_i(\vec{r}(t)) \ , \tag{1.7}$$

with $\vec{r}(t)$ being the position of the charge q at the time t. The weighting potential $\psi_i(\vec{r})$ in eq. (1.7) is an auxiliary quantity corresponding to a dimensionless potential. It is calculated by solving Poisson's equation with a zero space charge $\rho(\vec{r}) = 0$ and with the boundary conditions

$$\begin{aligned} \psi_i(\vec{r}) &= 1 \quad \forall \ \ \vec{r} \in \delta\Omega_i \\ \psi_i(\vec{r}) &= 0 \quad \forall \ \ \vec{r} \in \delta\Omega_{j \neq i} \ , \end{aligned} \tag{1.8}$$

where $\delta\Omega_i$ corresponds to the surface of the electrode i [6]. Hence, for the determination of the pulse shapes, the weighting potentials of all electrodes have to be computed. The weighting potential of segment E4 of a symmetric AGATA detector is shown in fig. 1.7 b).
As a result, the pulse shapes $Q_i(t)$ of the electrode i considering all drifting electrons and holes reads

$$Q_i(t) = q_{\text{cloud}} \cdot [\psi_i(\vec{r}_e(t)) - \psi_i(\vec{r}_h(t))] \ , \tag{1.9}$$

where $\vec{r}_e(t)$ and $\vec{r}_h(t)$ are the electron and the hole trajectory, respectively [6]. q_{cloud} is the absolute value of the total charge of the electron or the hole cloud.

The calculation of the pulse shapes is a challenging task as a lot of parameters have to be taken into account. These parameters are often not known precisely and strongly model dependent [6], resulting in systematic errors of the pulse shape basis. Furthermore, it has to be mentioned that due to the complex geometry of the AGATA crystals, most of the stated equations have to be solved numerically. Additionally, interpolation algorithms are necessary [6].
All simulated pulse shape bases are based on the described principles. They "only" vary in their implementation and their input parameters.

JASS	electron mobility parameters			
direction	$\mu_0 \left[\frac{\mathrm{cm}^2}{\mathrm{Vs}}\right]$	β	$E_0 \left[\frac{\mathrm{V}}{\mathrm{cm}}\right]$	$\mu_n \left[\frac{\mathrm{cm}^2}{\mathrm{Vs}}\right]$
$< 100 >$	40 180	0.72	493	589
$< 111 >$	42 420	0.87	251	62
JASS	hole mobility parameters			
direction	$\mu_0 \left[\frac{\mathrm{cm}^2}{\mathrm{Vs}}\right]$	β	$E_0 \left[\frac{\mathrm{V}}{\mathrm{cm}}\right]$	$\mu_n \left[\frac{\mathrm{cm}^2}{\mathrm{Vs}}\right]$
$< 100 >$	66 333	0.744	181	-
$< 111 >$	107 270	0.580	100	-

Tab. 1.3: Parameters of the mobility model used in the JASS basis. A detailed explanation of the model can be found in [6].

ADL	electron mobility parameters I			
direction	$\mu_0 \left[\frac{\mathrm{cm}^2}{\mathrm{Vs}}\right]$	β	$E_0 \left[\frac{\mathrm{V}}{\mathrm{cm}}\right]$	$\mu_n \left[\frac{\mathrm{cm}^2}{\mathrm{Vs}}\right]$
$< 100 >$	37 165.4	0.80422	507.7	$-1.447 \cdot 10^{-4}$
ADL	electron mobility parameters II			
	η_0	η_1	η_2	$E_0 \left[\frac{\mathrm{V}}{\mathrm{cm}}\right]$
	0.459	0.0294	$5.4 \cdot 10^{-5}$	1200
ADL	hole mobility parameters			
direction	$\mu_0 \left[\frac{\mathrm{cm}^2}{\mathrm{Vs}}\right]$	β	$E_0 \left[\frac{\mathrm{V}}{\mathrm{cm}}\right]$	$\mu_n \left[\frac{\mathrm{cm}^2}{\mathrm{Vs}}\right]$
$< 100 >$	62 934	0.73526	181.9	-
$< 111 >$	62 383	0.7488	143.9	-

Tab. 1.4: Parameters of the mobility model used in the ADL basis. A detailed explanation of the model can be found in [15] and [16].

The JASS and the ADL signal basis

In the following sections the performance of the signal bases JASS (Java Agata Signal Simulation, [6]) and ADL (AGATA Detector simulation Library, [15]) are discussed. Hence, their characteristic features are presented in more detail: Currently, both bases assume the same crystal orientation. The z-axis (symmetry axis) of the crystal coincide with the $< 001 >$-direction of the germanium crystal lattice, while the $< 100 >$-direction of germanium forms an angle of $\alpha = 45°$ with the x-axis of the coordinate system which passes the tip of the segment A[11]. Nevertheless, the main difference in the calculation of the two bases are the mobilities of the charge carriers. The used mobility parameters for JASS and ADL are summarized in tabs. 1.3 and 1.4, respectively. Comparing the corresponding electron parameters of the $< 100 >$-direction and the hole parameters of both directions, it is obvious that the bases do not feature the same drift velocities. Thus, the calculated signals of JASS and ADL differ. Additionally, the ADL basis uses a slightly different parametrization for the electron drift velocity. Details on the mobility models can be found in [6] for JASS and [15, 16] for ADL. Apart from that, JASS calculates the pulse shapes on a 1 mm cubic grid, whereas ADL uses a 2 mm cubic grid.

[11] Nevertheless, the ADL basis of the A003 crystal in symmetric test measurement (c.f. chap. 4) features $\alpha = 40°$.

1.5 Thesis Overview

This chapter discussed the need of a new generation of γ-ray spectrometers for future radioactive beam facilities such as FAIR. As an example for a modern γ-ray detector which is currently under construction, the Advanced GAmma Tracking Array AGATA is described in more detail (c.f. sec. 1.2). Its philosophy is the γ-ray tracking, i.e. to reconstruct the scattering path of incident γ-rays, to gain a significantly higher photopeak efficiency and good P/T ratio compared to existing γ-ray spectrometers. An important input of the tracking algorithms are the γ-ray interaction points which are reconstructed with the help of pulse shape analysis (PSA). Its concept is introduced in sec. 1.3 and sec. 1.4.
To validate the PSA chap. 2 presents possible PSA calibration experiments. The main focus of this thesis is set on a ^{22}Na calibration measurement which exploits the angular correlation of the annihilation γ-rays to extract the position resolution of the AGATA detectors. Furthermore, sec. 2.2 presents the setups of two executed test experiments.
In chap. 3 the analysis strategies of the ^{22}Na calibration experiment are detailed. For a better understanding a Geant4 based Monte Carlo simulation is included. The analysis deals with two different event selections (c.f. sec. 3.3): The position resolution of single γ-ray interaction points is studied as well as the position resolution of the energy weighted barycenter of all interaction points which are contained in a segment.
Chap. 4 presents the results of the first test experiment. It uses a symmetric source position leading initially to a mean position resolution of the involved crystals. However, with a multi-parameter fit the position resolution of individual crystals can be determined, too.
The second test measurement features asymmetric source locations in order to investigate the position resolution of a single crystal independently of the resolution of another crystal (c.f. chap. 5). Several source positions are chosen to determine the position resolution for each crystal row separately. Furthermore, this chapter includes a discussion of the energy dependence of the PSA performance (c.f. sec. 5.4) and the influence of the PSA algorithm on the position resolution (c.f. sec. 5.5).
Finally, chap. 6 discusses the obtained results and gives an outlook on possible modifications of the calibration experiment.

Chapter 2

A Calibration Experiment for the AGATA Pulse Shape Analysis

The new generation of γ-ray spectrometers for future radioactive beam facilities is based on the concepts of γ-ray tracking (c.f. sec. 1.1). An important input parameter for these tracking algorithms are the γ-ray interaction positions in the HPGe detector arrays. They are obtained by a detailed analysis of the pulse shapes. Hence, the capability of the γ-ray tracking is strongly dependent on the performance of the pulse shape analysis (PSA). Therefore, a reliable experimental method has to be developed to determine the achievable position resolution and its dependence on the quality of the simulated signal basis. For the AGATA detectors there are currently several experimental approaches for the calibration of the PSA parameters available.
A direct method is the so called scanning table which allows determining the pulse shapes of an experimentally defined interaction point. These pulse shapes are afterwards compared to the simulated pulse shapes. An example of such a scanning setup which is realized by the University of Liverpool is schematically shown in fig. 2.1. The interaction point is defined by a Compton scattering with a fixed geometry. This is realized using a strong ^{137}Cs source. It is located behind a long lead collimator to create a pencil beam which fixes two coordinates of the interaction point. The last coordinate is defined by further collimators with subsequent BGO detectors to detect the scattered γ-ray. [3], [17]
An indirect method for the PSA calibration was developed which exploits the Doppler broadening of a known γ-line. As shown in sec. 1.1, the Doppler correction capability of a γ-ray array is strongly related to the position resolution of the first interaction point. Thus, a careful analysis of the line width allows the determination of the PSA performance. This was successfully demonstrated with an in-beam experiment of the first AGATA prototype triple cluster using the reaction ^{48}Ti(d,p)^{49}Ti in inverse kinematics. The achieved resolution was about 5 mm (FWHM of a Gaussian distribution) for 1382 keV γ-rays. [3], [18]

These two calibration experiments are both working and are already used to characterize important PSA parameters. Nevertheless, both feature a few significant disadvantages.
The scanning method is only an offline method, i.e. the crystals have to be unmounted from the AGATA array for their characterization. Thus, they are not available for a long time in present beam experiments. Additionally, scanning the crystals is very time consuming as the necessary collimators lead to a low interaction rate of the γ-rays, especially in the last rows of the crystal. Thus, an analysis of all 180 crystals of the final AGATA array is not practicable. Another problem are the systematic errors. It is e.g. difficult to define the interaction position precisely with the collimators in the scanning setup [6]. Therefore, scanning setups often result in "supertraces". A "supertrace" is the mean signal of all measured pulse shapes of a scanning

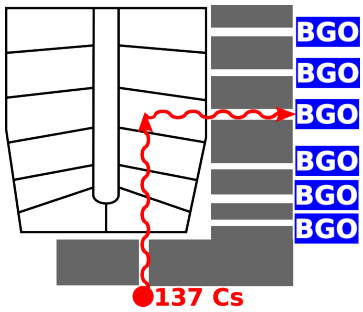

Fig. 2.1: Schematic setup of the Liverpool scanning table for the direct measurement of pulse shapes at known interaction points. The interaction point is defined by a Compton scattering of γ-rays emitted by a strong ^{137}Cs source. The collimator in front of the source defines the initial γ-ray direction. The scattered γ-ray is then detected in BGO detectors behind collimators which define the scattering angle and thus the last coordinate of the interaction point. The measured pulse shapes with known interaction positions are subsequently compared to the simulated pulse shapes.

point which correspond to an average position. These "supertraces" have the second advantage that the noise is canceled to a certain amount. However, due to the different electronics of the current scanning tables and the AGATA array the noise structure is still not identical.
Totally different is the characterization by Doppler broadening. This is an online method applicable to all crystals mounted at the same time. However, due to the low cross sections of the used reactions, the Doppler shifted γ-rays are only produced with a low rate. Thus, a lot of expensive beam time is needed for the calibration experiment. Furthermore, the determination of the PSA position resolution is only based on a single parameter, the linewidth of the Doppler shifted γ-rays. Thus, only a overall position resolution of the whole crystal can be determined instead of analyzing different regions in the crystal separately. As a result, it is e.g. difficult to locate regions where the basis is badly modeled. Apart from that, it is very important to know all contributions to the linewidth to get a good idea of the position resolution.
Therefore, a new calibration method for the AGATA PSA is essential. One possible calibration experiment was developed and validated in the scope of this thesis. The requirements and the concept of this calibration method are described in sec. 2.1. To proof its principle two test measurements were performed with several AGATA detectors. Their setups, the data analysis and the results are presented in the following sections.

2.1 Online Experiment with a ^{22}Na Source

Based on the experience with scanning tables and the in-beam experiment the new calibration method should fulfill the following requirements: First of all, it should be designed as an online experiment which can be easily conducted during or in between two beam times. Therefore, a short measurement time and a simple mechanical setup without moving the crystals are necessary. Furthermore, it is important that a modification of the electronics is not needed for the calibration experiment. This also has the advantage that the electronics have the same impact on the pulse shapes in the calibration measurement and in beam time experiments. Therefore, systematic errors such as a different noise structure are canceled.
To meet these requirements a new calibration experiment has been developed. Its concept is visualized in fig. 2.2. The general principle is to use a positron emitter e.g. a ^{22}Na source. If the positron annihilates with an electron, two 511 keV γ-rays are emitted nearly back to

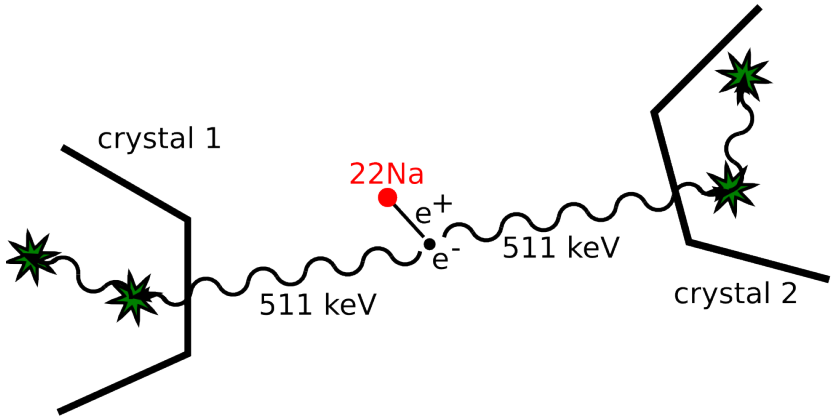

Fig. 2.2: Concept of an online calibration experiment for the AGATA pulse shape analysis. The two 511 keV γ-rays of the ^{22}Na source are emitted back to back. They are detected in coincidence in two opposite AGATA crystals. The angular correlation of the annihilation γ-rays can be used to determine the PSA performance.

back. These annihilation γ-rays are then detected in two opposing AGATA crystals. Their interaction positions are indicated in fig. 2.2 with green stars. The angular correlation of the γ-rays is exploited to determine the position resolution: The first interaction positions and the source should be located on one straight line. Using different stereo angles the deviations from this expected line can be used to determine the position resolution of the PSA in three dimensions. The analysis strategy to extract the position resolution from the angular correlation is detailed in chap. 3.

2.2 Setup of two Test Experiments

To verify the idea of the online calibration experiment two test measurements were performed at the Laboratori Nazionali di Legnaro (LNL) in Italy, which is currently the host laboratory of the AGATA Demonstrator. In both experiments the same ^{22}Na source with an activity of about 750 Bq was used. As the source geometry is not known, it is assumed that the radioactive ^{22}Na material is point-like and that it is housed in a thin plastic disk.
The setup of the first test measurement is shown in fig. 2.3. The ^{22}Na source is positioned in the center of three installed triple clusters of the AGATA Demonstrator. To exploit the angular correlation of the 511 keV γ-rays, they have to be detected in coincidence (c.f. chap. 3). Therefore, this setup allows studying the PSA performance of the red crystals A001 and A003. Based on the experience of the first test experiment, a second test measurement was performed at LNL. Fig. 2.4 a) visualizes the different setup. In contrast to the first experiment, an asymmetric source position was used: The ^{22}Na source was mounted directly at the cryostat wall of the red A006 detector. This allows studying the A006 crystal in more detail. Moreover, the measurement was conducted at several source positions on the A006 cryostat to be sensitive to the PSA performance in different regions of the crystal. The used source positions are shown in fig. 2.4 b) with respect to the segmentation of the A006 crystal. Furthermore, the experience of the first test measurement showed that it is likely that a non negligible amount of positrons can escape the source and annihilate e.g. in the cryostat of the crystals. These escaping positrons produce background events which mimic a bad PSA position resolution. As these events cannot be excluded in the analysis, the ^{22}Na source is covered with additional aluminum to ensure that the annihilation vertex is always located close to the source material.

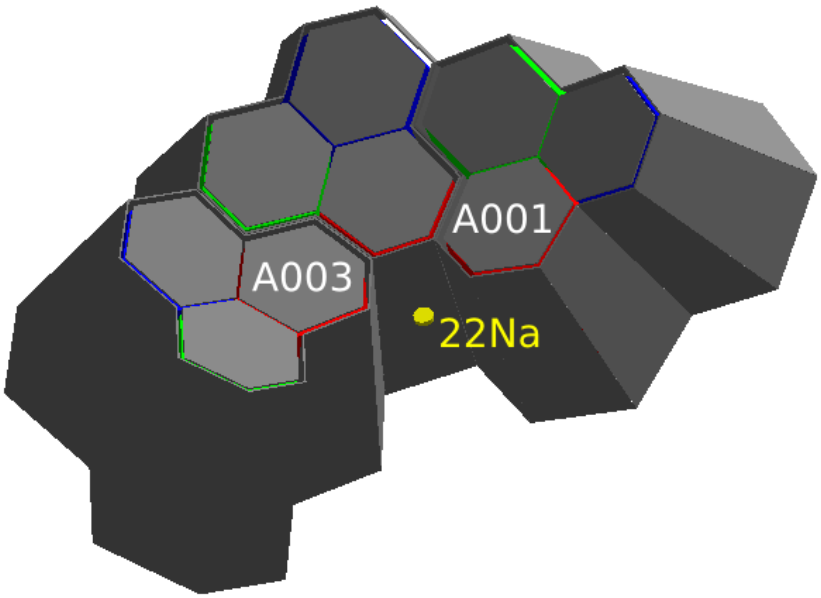

Fig. 2.3: Setup of the first test experiment to proof the principle of the online calibration method for the AGATA PSA. A point-like ^{22}Na source is positioned in the middle of the first triple clusters of the AGATA Demonstrator. As the two annihilation γ-rays of ^{22}Na are detected in coincidence, only the crystals A001 and A003 can be studied.

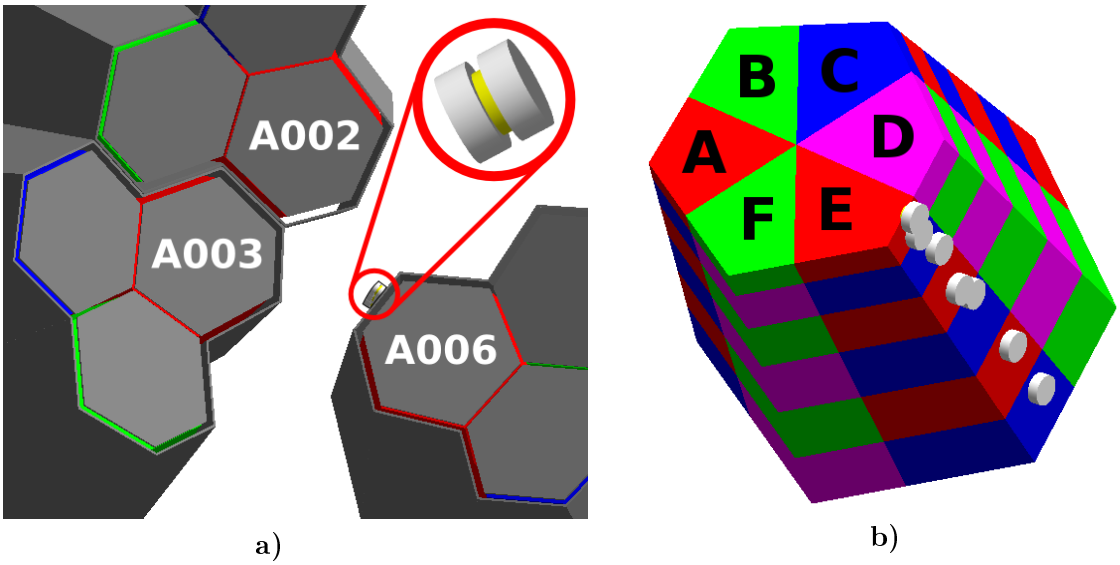

Fig. 2.4: **a)** Setup of the second test experiment of the online calibration method. A ^{22}Na source is located at the cryostat of the A006 crystal. It directly faces two other crystals of the AGATA Demonstrator. The zoomed view of the source shows that it is enclosed with aluminum to prevent the positrons from escaping the source. **b)** Measured source positions to receive a position dependent PSA performance. For a better orientation the segmentation of the crystal is visualized, too.

2.3 Energy Spectra

The determination of the PSA performance requires the coincident detection of the 511 keV annihilation γ-rays. Thus, a precise energy cut on the 511 keV peaks is necessary to gain a high background rejection. For its definition it is essential to study the recorded energy spectra of the crystals in more detail. In sec. 2.3.1 the energy resolution of the AGATA detectors and the shape of the 511 keV annihilation line are analyzed. Sec. 2.3.2 describes the impact of the crystal segmentation on the energy spectra.

2.3.1 Energy Resolution of the AGATA Detectors

A typical core energy spectrum from the crystal A001 measured in the symmetric setup is shown in fig. 2.5 a). It shows three clear lines. The first one at $E_\gamma = 511$ keV is due to the positron annihilation radiation. At $E_\gamma = 1.275$ MeV the $2^+ \rightarrow 0^+$ transition in ^{22}Ne, dominantly populated by the β^+-decay of ^{22}Na , is seen while the last peak corresponds to the sum peak of both lines. Furthermore, their Compton continua with the corresponding Compton edges are visible. A Gaussian fit to the 1.275 MeV γ-line in the core spectrum results in an energy resolution of FWHM = (2.67 ± 0.03) keV.
Contrary, the resolution at $E_\gamma = 511$ keV cannot be determined in the same way as the kinematics of the positron annihilation leads to an additional broadening of the line. This effect is clearly visible in the energy correlation of both emitted γ-rays which are detected in different detectors (c.f. figs. 2.5 b) and 2.5 c) for the first and the second test experiment, respectively). Both measurements feature an elliptical anticorrelation of the energies.

Explanation for the elliptical anticorrelation
The shape of the peak originates from the kinematics of the annihilation process. In the rest frame of the electron-positron pair the energy of both γ-rays corresponds exactly to the rest mass of an electron. Furthermore, the γ-rays are exactly emitted back to back due to momentum conservation. In the laboratory frame the situation is different. Before the annihilation the positron is slowed down until its energy is below one eV (thermal equilibrium) [19]. Thus, it can be considered to be at rest. Contrary, the electron has a finite momentum due to its binding which is characteristic for its host material [19]. Therefore, the energies and the relative directions of the 511 keV γ-rays depend on the electron momentum. A Lorentz transformation of the electron and positron quantities from the rest to the laboratory frame yields an energy difference ΔE and an angular deviation $\Delta\theta$ from 180° [19]:

$$\Delta E \approx c p_\parallel \quad \text{and} \quad \Delta\theta \approx \frac{p_\perp}{m_e c}. \tag{2.1}$$

This equation holds for small electron momenta p with $p_\parallel$ being the longitudinal and $p_\perp$ being transverse component with respect to the emission directions of the γ-rays. These deviations are estimated in first order. As the total energy of the γ-rays is conserved, one γ-ray is red-shifted by $-\Delta E/2$ while the second is blue-shifted by $\Delta E/2$. This results in the elliptical peak shape displayed in the figs. 2.5 b) and c). In condensed matter ΔE is typically about 2 keV and $\Delta\theta$ in the order of a few mrad[1] [19]. As these quantities are only dependent on the electron properties of the material, the electron-positron annihilation is a powerful tool to investigate material properties. Typical applications of positron-annihilation spectroscopy include studying defects in crystal lattices. This is possible as positrons preferably stay in the inter-atomic space due to the Coulomb repulsion of the positive ion cores. [19], [20]

[1] This small deviation from 180° can be neglected in the determination of the PSA position resolution in contrast to the energy shift.

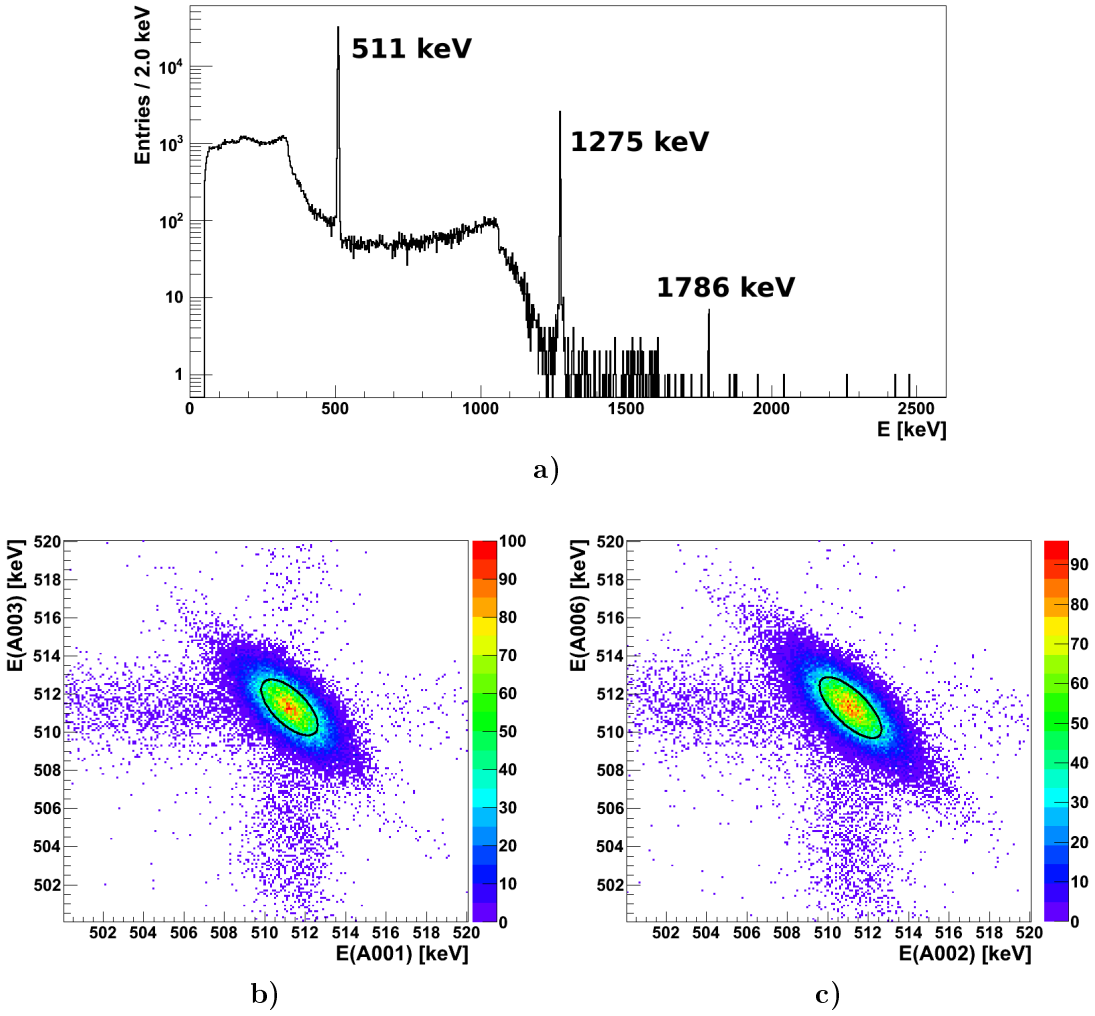

Fig. 2.5: a) Core energy spectrum of the crystal A001. The 1.275 MeV line of ^{22}Na has an energy resolution of FWHM = (2.67 ± 0.03) keV. **b)** and **c)** Energy correlations for the first and second test measurement. The elliptical shape of the annihilation peak is a consequence of the kinematics of the positron annihilation.

Due to the different mean electron momentum in aluminum and plastic, the energy shift ΔE of the annihilation γ-rays is different in the first and second test experiment because in the latter the source is additionally covered with aluminum. As the average electron velocity in aluminum is bigger than in plastic the semi-major axis of the ellipse is longer for the second test experiment. The semi-minor axis has the same length for both measurements as it is not affected by the nature of the positron annihilation. It is solely defined by the energy resolution of the detectors. The black ellipses in figs. 2.5 b) and c) show the contour line at the half peak height. The distributions of the energy correlation along the major and minor axis have a Gaussian shape. The FWHMs of the Gaussian distributions can be used to determine the energy resolution of the crystals:

- 1^{st} measurement: FWHM(minor axis) = (1.71 ± 0.03) keV,
  FWHM(major axis) = (3.67 ± 0.04) keV
- 2^{nd} measurement: FWHM(minor axis) = (1.67 ± 0.02) keV,
  FWHM(major axis) = (4.09 ± 0.05) keV.

The FWHM(minor axis) is composed of the energy resolutions of the individual crystals:

$$\text{FWHM(minor axis)} = \sqrt{\Delta E(\text{detector 1})^2 + \Delta E(\text{detector 2})^2}. \tag{2.2}$$

Assuming both detectors to be equal, the obtained mean energy resolutions are

$$\Delta E(\text{A001, A003}) = (1.21 \pm 0.02)\,\text{keV} \quad \text{and} \quad \Delta E(\text{A002, A006}) = (1.17 \pm 0.02)\,\text{keV} \tag{2.3}$$

for the first and second test experiment, respectively.
The energy cut used in the determination of the position resolution is defined by the elliptical contour line at half peak height (black line in figs. 2.5 b) and c)). All events inside this contour line are considered in the analysis.

2.3.2 Influence of the Segmentation

Besides the positron annihilation, there is a second effect which can change the shape of the 511 keV peak in the case multiple segments are hit: The annihilation line in the core spectrum can differ from the annihilation peak in the sum energy spectrum of two neighboring segments, even though no other segment shows any energy deposition. As indicated in fig. 2.6 a) the 511 keV line in the sum energy spectrum of the neighboring segments D1 and E1 has a more pronounced tail at the lower energetic side of the peak compared to the corresponding core spectrum. This effect can be seen more clearly in fig. 2.6 b) which shows the energy difference between the core and the sum energy of the hit segments, indicating that the segments loose part of the signal compared to the core. Fig. 2.6 c) visualizes the energy correlation of the segment energies. Here the missing energy appears in a bow below the anticorrelation line of the Compton scattered events. Fig. 2.6 d) displays the same plot but rotated by 45° showing that the missing energy can reach up to 60 keV. Thus, this bow effect cannot be neglected as it is one order of magnitude above the energy resolution of HPGe detectors.
To understand this phenomenon, it is useful to look at the electron-hole cloud created by the γ-ray interaction. Due to the bias voltage the cloud separates. The electrons drift towards the core and the holes to the outer segment contacts. If the γ-ray interaction occurs in the middle of a segments, all holes are collected by a single segment electrode. Thus, the core and the segment detect the same energy. However, if a γ-ray interaction is located near a segment boundary, the situation is different. Due to the space between the segment contacts the electric field is weak near the gap between the two contacts [21]. This results in a low drift velocity for the holes. Therefore, the diffusion of the hole cloud increases in this region. Thus, it can expand over two segments. As a result, two segments show a net charge signal making a single interaction position looking like two interaction points. Moreover, due to the low drift velocity it is possible that not all holes are collected fast enough leading to a ballistic deficit[2]. Thus, the segment energy seems to be lower than the core energy[3]. This effect dominates if the center of the hole cloud is at the segmentation line. Therefore, the energy loss is maximal if both segments detect the same energy. It can be concluded that due to energy conservation the energy loss in the segmentation boundary is fixed by the total energy deposited in the interaction (i.e. the energy which is detected by the core) and the position of the interaction on the segmentation boundary (i.e. the ratio of the energies detected in the adjacent segments).
As a result, the events in fig. 2.6 can be divided into three different event types. These three scenarios are schematically shown in figs. 2.7 a) - c). Fig. 2.7 a) illustrates the most common

[2] At first glance this explanation violates Ramo's theorem as the sum of all signals in not zero at all times [6]. However, it is still valid as the holes in the gap of the segmentation lines induce a charge on the aluminum can which has to be considered, too.

[3] Crosstalk which is explained in sec. 3.1.2 cannot be the reason for the different line shapes as it is already corrected. Furthermore, crosstalk would lead to a shift of the 511 keV peak which isn't present here.

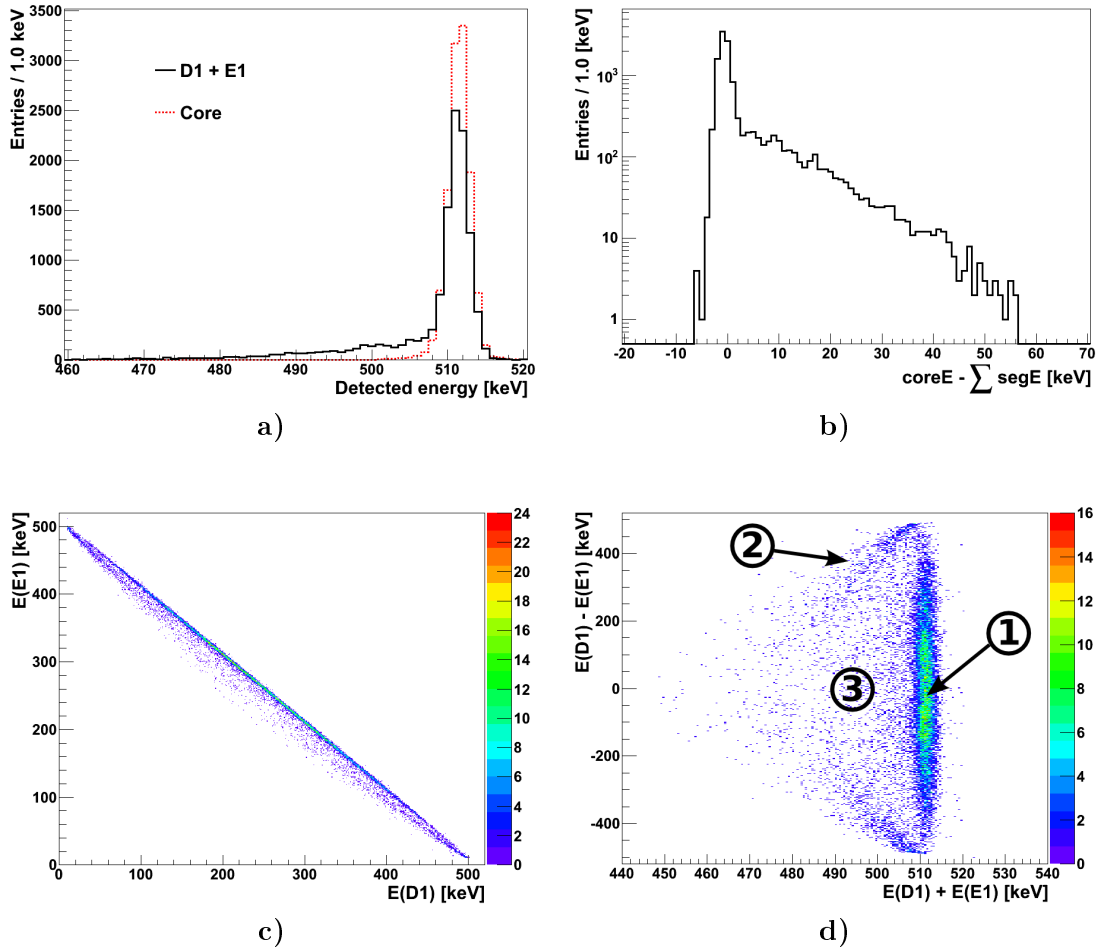

Fig. 2.6: Energy spectra of events featuring the absorption of a single γ-ray from the ^{22}Na source in two neighboring segments. **a)** Energy spectra of the core (red dotted line) and the sum spectrum of the neighboring segments D1 and E1 (black solid line). The tail of the segment spectrum at the lower energetic side of the peak is due to charge losses in the segmentation line between the segments. **b)** Difference between both spectra showing the magnitude of the charge loss. **c)** and **d)** Energy correlation between the hit segments. The bow structure is due to charge sharing between the segments and the insufficient collection of the hole cloud [21]. The numbers shown in **d)** correspond to the respective numbers in fig. 2.7.

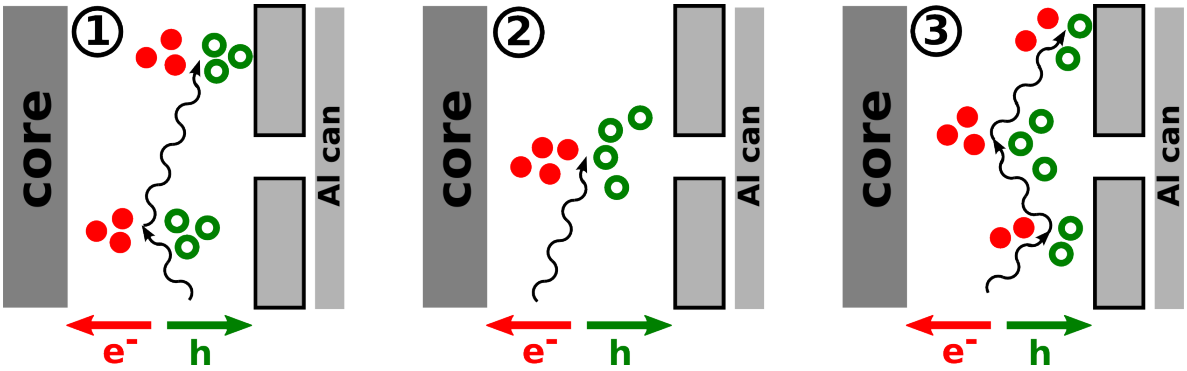

Fig. 2.7: Explanation of the bow effect. If the γ-ray interaction takes place near a segment boundary the hole cloud can expand over the two neighboring segments. Thus, both segments show a net charge signal and a single interaction point looks like two interaction positions.

case which is a Compton scattering from one segment into the neighboring segment. Here, both hole clouds are completely collected by their own segment electrode. This results in the dominating line in fig. 2.6 c) which crosses the axes at 511 keV (area 1 in fig. 2.6 d)). Due to the geometry of the experimental setup scattering angles close to 90° are preferred which corresponds to equal energy depositions in each segment. Moreover, it is possible that the 511 keV γ-ray deposits its energy in a single interaction near the segmentation line (c.f. fig. 2.7 b)) leading to charge sharing and charge loss as described above. As the photoelectric absorption is the highest possible energy deposit, the energy loss is maximal. Hence, these events are located at the outer side of the bow in figs. 2.6 c) and d) (area 2 in fig. 2.6d)). The last event type, displayed in fig. 2.7 c), features Compton scatterings from one segment into the neighboring segment with one interaction point near the segmentation line. Thus, the number of holes in the cloud near the segmentation boundary is not constant resulting in a variable energy loss. Therefore, there are also entries in the whole bow area in figs. 2.6 c) and d) (area 3 in fig. 2.6 d)). Furthermore, there are a lot of events featuring a signal loss, a small energy deposition in one segment and a very large energy deposition in the other segment. They are due to multiple Compton scatterings in one segment where one interaction point is close to the segmentation line. [21], [22]
Comparing the energy correlations of all neighboring segment combinations the bow effect is strongest in neighboring segments of the first row. This can be explained since their segmentation lines are much wider than for the other rows [21]. Additionally, the segmentation lines are much longer compared to other segments.
Although the bow effect has a big impact on the energy spectra, it does not influence the further analysis. Due to the large energy loss these events will be excluded with the elliptical cut on the 511 keV line.

2.4 Geant4 Simulation

To get a better understanding of the calibration experiment a Geant4 simulation for the two test measurements was performed [23], [24]. It is based on the official AGATA simulation package written by Enrico Farnea [25]. In this section the implementation of the ^{22}Na source, the crystals and the energy resolution is briefly described.

^{22}Na source
For the analysis of the PSA position resolution it is of great importance that the electron-positron annihilation vertex is modeled correctly. The distribution of the annihilation points is not trivial because the positrons have a finite range in the source material. Thus, it is not sufficient to implement a point-like source emitting two 511 keV γ-rays in the Geant4 simulation. Instead a more complex structure for the ^{22}Na source is needed. As the positron range is energy dependent the spectrum of the β^+-decay has to be considered. The shape of the β-spectrum is based on the level scheme of ^{22}Na (c.f. fig. 2.8 a)), on Fermi's Golden Rule and on the Fermi function which takes the Coulomb field of the nuclei and of the atomic electrons into account [26] , [27]. The calculation of the β-spectrum is described in more detail in app. B. The result is visualized in fig. 2.8 b). Thus, the positrons from the β^+-decay have a mean kinetic energy of 216 keV and an end point energy of 546 keV. In the simulation the positrons are emitted isotropically with an energy distribution following the calculated β-spectrum. For the sake of completeness the 1.275 MeV γ-ray is additionally emitted at the positron starting point in Geant4.
In the simulation of the test experiments the source is implemented as a thin plastic disk

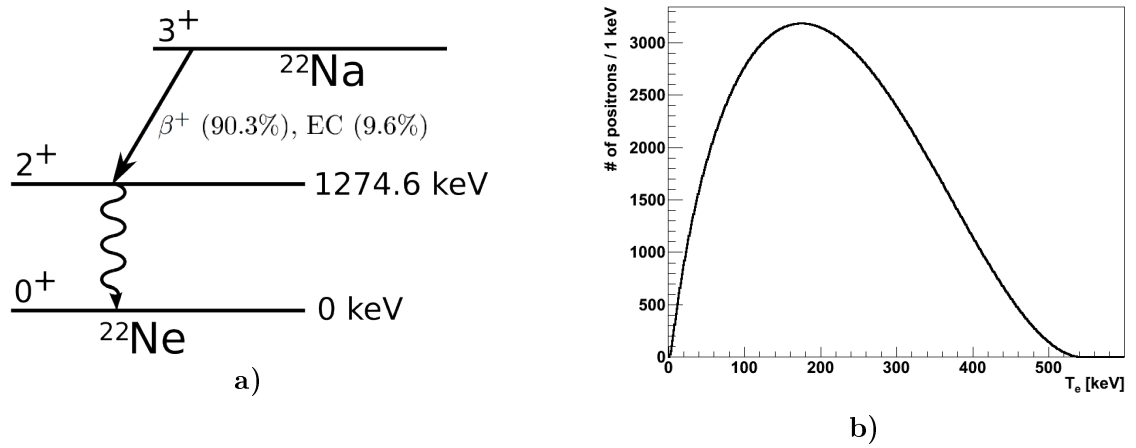

Fig. 2.8: a) Simplified level scheme of ^{22}Na (based on [28]) **b)** Distribution of the positrons for one million ^{22}Na decays as a function of the kinetic energy T_e of the positron.

(radius = 5 mm, height = 1 mm) with a point-like ^{22}Na material in its center[4]. Furthermore the simulation of the second measurement includes a cylindrical aluminum coverage (radius = 7 mm, height $\approx$ 2.5 mm) on both sides of the source as shown in the fig. 2.4 a).

Range of positrons in matter

After calculating the energy spectrum of the positrons their range in matter has to be determined. The dominant energy loss process of positrons is ionization but also a small amount of bremsstrahlung occurs. During the deceleration process, the positrons often change their direction. As a result, the traveled path length is much longer than the range of the positrons. The latter is defined as the shortest distance between the starting point and the annihilation vertex. To receive the positron range, a separate Geant4 simulation was performed for the relevant materials plastic (C_3H_6, density $\rho = 0.9\,g/cm^3$), air ($\rho = 0.001\,g/cm^3$) and aluminum ($\rho = 2.7\,g/cm^3$). Fig. 2.9 a) shows the ranges of positrons resulting from the β^+-decay of ^{22}Na for the source materials plastic and aluminum. Positrons in plastic have a maximal range about 1.5 mm whereas aluminum has the shortest range with about 0.5 mm. The distribution of the positron annihilation vertices in plastic, air and aluminum are shown in figs. 2.9 b) - d). Thus, it is possible that the positrons escape the 1 mm plastic disk of the ^{22}Na source. Therefore, it is likely to happen in the symmetric test measurement[5]. These escaping positrons can travel a long distance in air as their range in air can extend up to 1.5 m. They typically annihilate in the cryostat of one of the AGATA detectors resulting in a background component in the analysis of the PSA position resolution. As the source dimensions are not known the amount of background events cannot be determined easily. Contrary, in the second test measurement that includes an aluminum coverage of the ^{22}Na source all positrons annihilate near the source material due to their short range in aluminum. Therefore, this background component is absent.

Geometry of the AGATA crystals

In the Geant4 simulation the detector geometry is included as precise as possible. The bare asymmetric germanium crystals have a length of 90 mm and are tapered according to the

[4]The radioactive material is implemented as a sphere with a radius of 0.1 mm.

[5]The actual size of the ^{22}Na source which was used in the measurements was not known. Therefore, the size of the plastic disk in Geant4 was roughly adapted in a way that the distribution of the interaction points in the crystals matches to the experimental data.

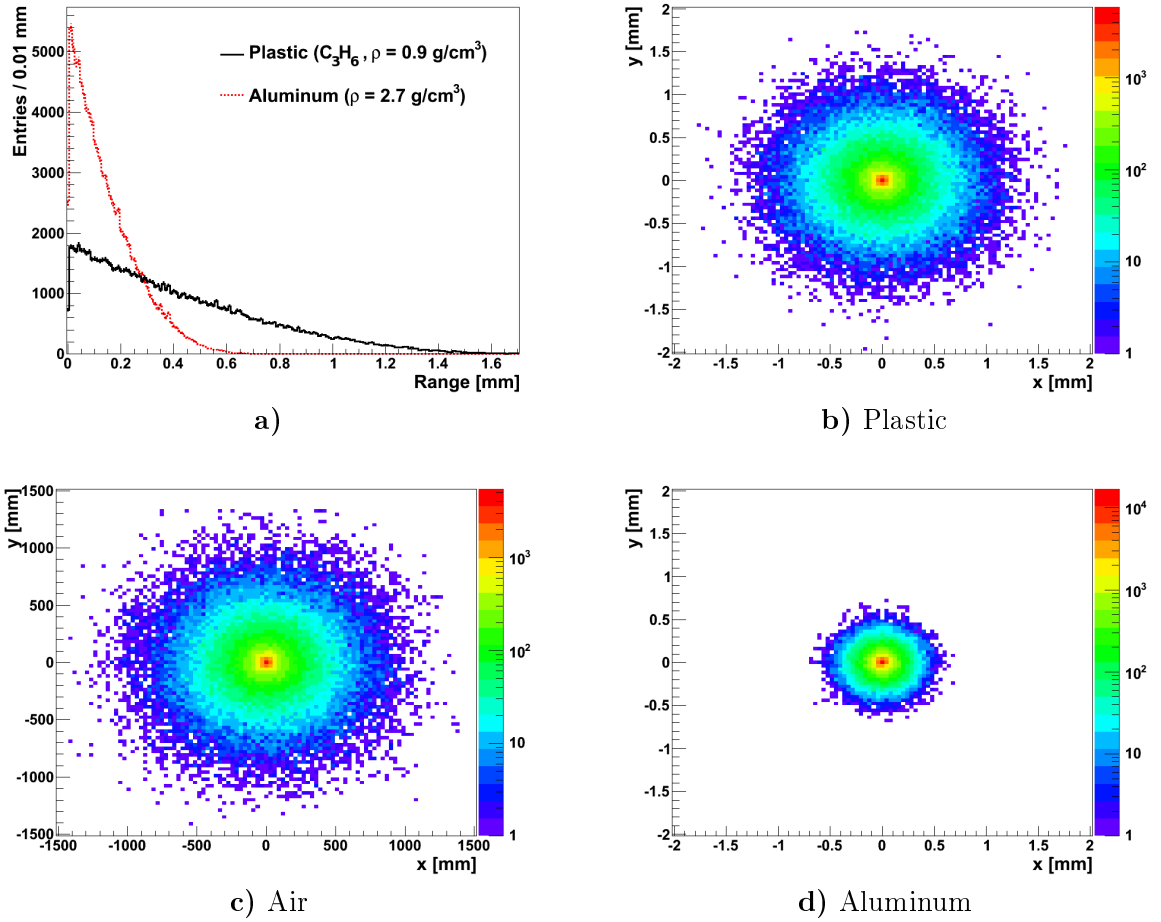

Fig. 2.9: **a)** Ranges of positrons emitted by ^{22}Na in the source materials plastic and aluminum. **b)**, **c)** and **d)** Distribution of the annihilation vertices of 100 000 positrons in plastic, air and aluminum. The positrons are produced at the origin of the coordinate system.

specifications of the three different crystal shapes. Furthermore, the aluminum encapsulation and the cryostat walls of the asymmetric triple clusters are taken into account. The resulting geometries of the test experiments have already been shown in figs. 2.3 and 2.4. Apart from that, the effective segmentation of the crystals is included. Fig. 2.10 a) visualizes a front view of a red crystal showing the segments in different colors. To adapt the crystal segmentation in Geant4 to the current knowledge [29] it was changed from the equal edge segmentation to the equal angle segmentation[6]. Fig. 2.10 b) displays the segmentation in the x-z plane of the crystal. For comparison fig. 2.10 c) shows the calculated segmentation of the JASS basis which matches the Geant4 segmentation quite well.

Barycenter

The PSA algorithm which is currently implemented in the Narval emulator [7] is only able to reconstruct one interaction position per segment. As a result, the PSA reconstructs the energy weighted barycenter of all interaction points. This is visualized in fig. 2.11. Therefore, the Geant4 simulation combines all single γ-ray interaction positions $\vec{r}_i$ of the segment to the

[6] In the equal edge segmentation the segment lines divide each of the six outer edges of the crystal in half, whereas in the equal angle segmentation the angle between the segmentation lines at the core contacts are all 60°.

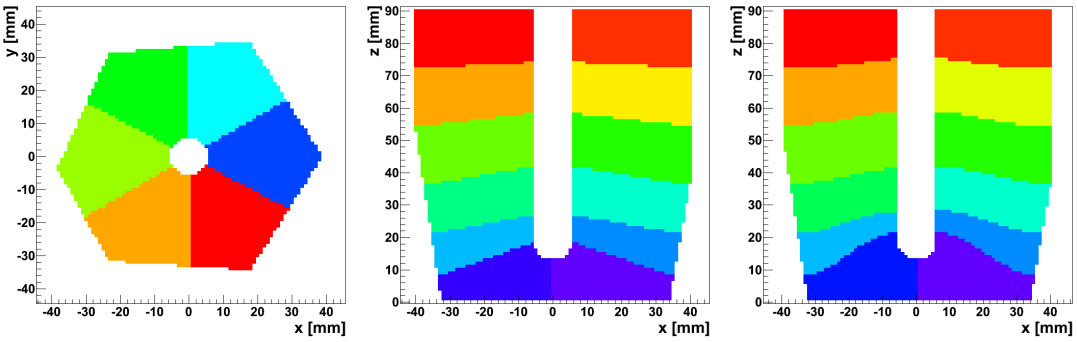

a) b) c)

Fig. 2.10: **a)** and **b)** Segmentation of the crystals in the Geant4 simulation. **c)** Segmentation of the JASS signal basis [6].

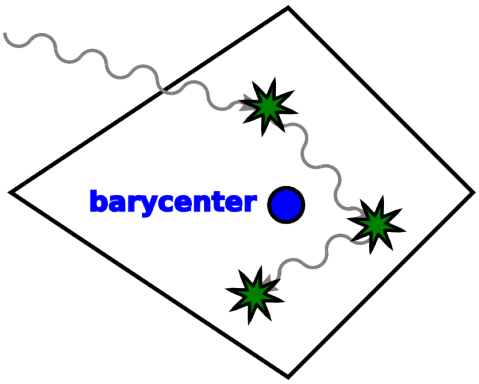

Fig. 2.11: Explanation of the barycenter. The incoming γ-ray deposits its energy in three interaction points (green stars) which are all located in one segment. According to the PSA algorithm these interaction points are packed together to their energy weighted mean value. This barycenter is marked with a blue circle.

energy weighted barycenter:

$$\vec{r}_{\text{barycenter}} = \frac{1}{E_{\text{barycenter}}} \sum_{i=1}^{N} \vec{r}_i \cdot E_i \quad \text{with} \quad E_{\text{barycenter}} = \sum_{i=1}^{N} E_i, \tag{2.4}$$

with E_i being the energy of a single interaction i.

Energy resolution

In the Geant4 simulation the energy resolution ΔE of the AGATA detectors is considered by smearing the deposited energy of the segments and the core with a Gaussian distribution. ΔE is assumed to be the full width at half maximum (FWHM) of the Gaussian distribution

$$\Delta E = \sqrt{A + B \cdot E}, \text{ with } A = 1.19\,\text{keV}^2,\ B = 1.82 \cdot 10^{-4}\,\text{keV}. \tag{2.5}$$

The constants A and B are defined by the energy calibration. Nevertheless, the elliptical shape of the 511 keV peak is not implemented in the simulation as it depends on crystal lattice defects of the material which cannot be defined in Geant4. Therefore, the broadening of the annihilation peak is taken into account by defining a worse energy resolution for the 511 keV γ-rays. Its FWHM is defined as the FWHM of a Gaussian distribution which results if the ellipses of the correlation plots in fig. 2.5 are projected on the energy axes. This leads to an energy resolution of about $\Delta E = 1.5$ keV (FWHM).

Chapter 3

Analysis Strategies

For the analysis and the interpretation of the data gathered in the calibration experiment several independent steps are required. First the full experiment has to be simulated in Geant4 to generate interaction points inside the active material (c.f. sec. 2.4). In a second step the experimental data has to be treated with all the analysis tools developed for AGATA. Before the AGATA PSA starts the so called preprocessing is performed (c.f. sec. 3.1). The resulting traces are subsequently used as input for the PSA. Its implementation is described in sec. 3.2. After the reconstruction of the interaction points with the PSA, their position resolution is determined. This requires a selection of suitable events from the overall dataset. The two event selections used for the analysis are detailed in sec. 3.3. Sec. 3.4 introduces the analysis strategy to extract a position resolution from the selected events.

3.1 Preprocessing of Pulse Shapes

Before the PSA compares the experimental traces with the traces of the simulated database all experimental signals have to be preprocessed. Figs. 3.1 a) and b) display a superposition of 1000 digitized raw signals of the core and the hit segments[1]. They were recorded by the A001 crystal during the symmetric test measurement. As its analysis is based on the annihilation peak of ^{22}Na, only events with $E_{\text{core}} \in [500, 520]$ keV are included in fig. 3.1. Hence, the superimposed signals have the same amplitude which corresponds to the deposited energy. However, rate dependent baseline fluctuations[2] are visible. As the gains of the segments are slightly different, the heights of the hit segment traces show a band structure. The signals in one band belong to the same segment. In contrast to the core, the rate of the segments is much lower resulting in a lower fluctuation of the baseline.
The preprocessing starts with a baseline correction and an amplitude calibration of the experimental traces. Due to the low rate of the calibration experiment, simplified algorithms can be used. The baseline is calculated from the average of the first 15 samples (150 ns) of each trace[3]. Afterwards, the amplitude of the signal is calibrated to ensure that it directly corresponds to the deposited energy. This is done with the signal average of the last 30 samples (last 300 ns) which are behind the rising slope.

[1] One sample corresponds to 10 ns.

[2] Baseline fluctuations occur if the previous signal has not completely decayed to the baseline before the next signal is present.

[3] According to fig. 3.1 the first 15 samples are significantly before the rising slope of the signal.

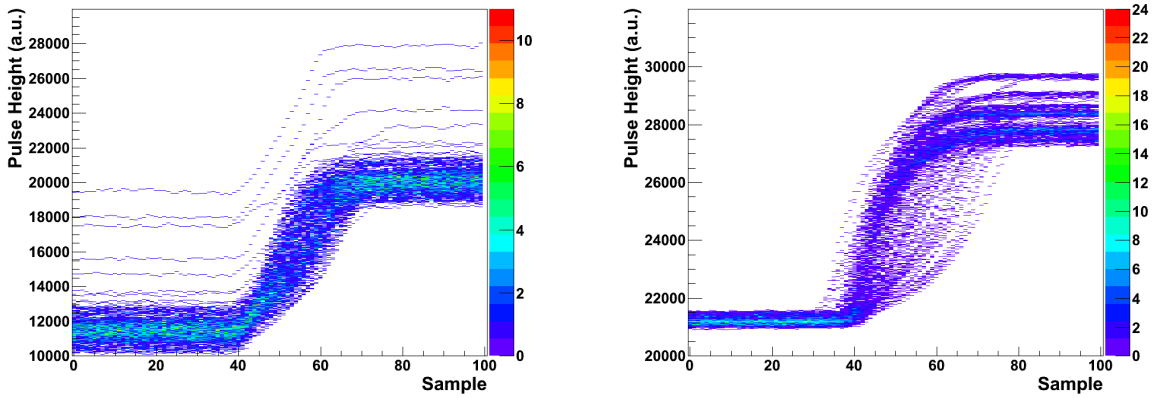

Fig. 3.1: 1000 raw pulse shapes of the A001 crystals as a function of ADC samples. **a)** The superposition of the core traces. **b)** The superposition of the hit segment traces. All included events feature a core energy E_{core} between E_{core} = 500 keV and E_{core} = 520 keV. The total energy is deposited in a single segment. One sample corresponds to 10 ns.

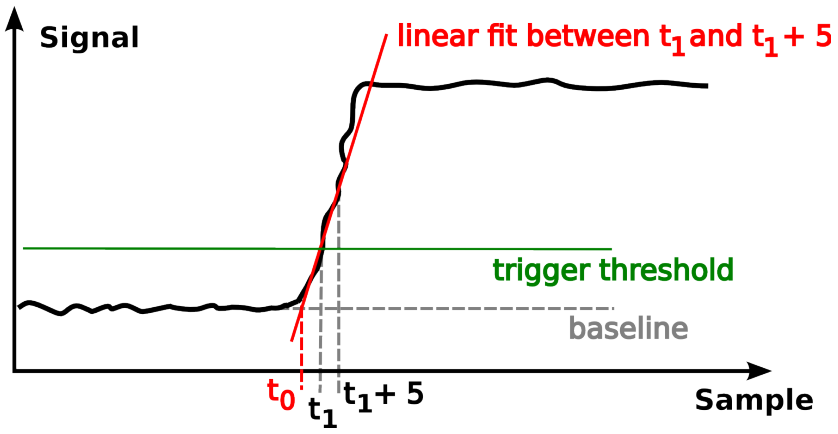

Fig. 3.2: Schematic drawing of the algorithm for the determination of the starting time t_0.

3.1.1 Time Alignment

To be able to compare the experimental pulses to the basis signals, a good time alignment of them is essential. This is accomplished by matching the start time t_0 of the experimental trace to the start time of the basis trace. t_0 can be received e.g. by a neural network (for details see [6]) or by a linear fit of the rising slope of the signal. As the latter algorithm is currently implemented in the Narval data acquisition software, it is described in the following: The method is sketched in fig. 3.2. First, a trigger threshold at about 4σ of noise over the baseline is defined. The sample where the experimental signal passes the trigger threshold is called t_1. Subsequently, a line is fitted to the signal in the range $[t_1, t_1 + 5]$. Its intersection with the baseline defines t_0. Finally, all experimental traces are shifted in a way that their t_0 is at sample 10.
The superposition of the 1000 preprocessed traces is shown in fig. 3.3. For a better comparison all traces are normalized to 1. The slope of the sum signal can be best approximated by a straight line. Hence, it is used for the determination of the start time. Furthermore, it has been shown that the results can be improved by introducing an additional shift of one sample i.e. using t_0 - 1 as start time of the experimental signal. After calculating the start time t_0 the baseline is corrected again by averaging over the last 10 samples before the t_0 sample.

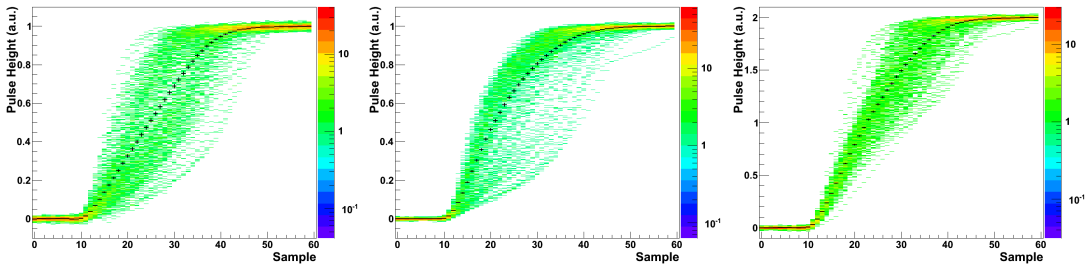

Fig. 3.3: Preprocessed traces of the A001 crystal. **a)** The core traces. **b)** The traces of the hit segment. **c)** The sum of the core and the hit segment traces. Furthermore the mean trace of all 1000 signals is visualized in black.

3.1.2 Crosstalk

The determination of the γ-ray interaction points by pulse shape analysis relies solely on a precise knowledge of the shapes of the traces. Therefore, all effects which influence the pulse shapes have to be considered. It has been shown that in segmented HPGe detectors the recorded signals at different electrodes are not independent due to capacitive coupling between the detector electrodes, the so called crosstalk. Generally, two types of crosstalk exist [6]:

- proportional crosstalk which is proportional to the signal amplitude
- derivative crosstalk which is proportional to the derivative of the signal

The proportional crosstalk which dominates between the core and the segment contacts causes an energy shift of the segments' amplitudes [6]. Therefore, the impact on the energy spectra is not negligible. This can be seen in the sum energy spectrum of all hit segments which was recorded e.g. with a ^{60}Co source. With increasing segment-fold[4] the sum energy peak is more and more shifted to lower energies [6].
The derivative crosstalk only occurs if the signal shape changes i.e. during its rise-time. Furthermore, it is only present in direct neighboring segments which coincide with the segments used for PSA. Thus, the derivative crosstalk component plays an important role in the PSA. Without a crosstalk correction the PSA can have a poor position resolution even though the simulation of the detector is perfect. [6], [30]
Narval includes the proportional crosstalk by directly correcting the energies and the signal amplitudes. The crosstalk correction of the traces is done by including the crosstalk in the basis. This approach has the advantage that the correction can be done before the actual PSA, saving computing time.

3.2 Pulse Shape Analysis

After preprocessing the experimental and basis traces are both used as input for the pulse shape analysis algorithm. The implementation used in this thesis is described in this section. Sec. 3.2.1 considers the case of events with one hit segment per crystal whereas sec. 3.2.2 addresses the more complex case of multiple hit segments. Finally, sec. 3.2.3 provides an outlook on the reconstruction of more than one interaction point in a single segment. Currently, the algorithm reconstructs only the energy weighted barycenter.

[4] segment-fold = number of hit segments

3.2.1 Single Hit Segments

The goal of the single hit-segment scenario is to reconstruct one interaction point in events where all energy deposited in the crystal is absorbed in a single hit segment, so called single hit events. This reconstructed interaction position corresponds to the energy weighted barycenter (c.f. fig. 2.11).
To determine the barycenter, the PSA searches for the basis signal S^{basis} which best matches to the experimental signal S^{exp}. The optimal basis trace defines the interaction position. In principle the PSA algorithm uses a χ^2-like test to compare the experimental traces to the basis traces. The figure of merit FOM which is used for the comparison is defined by [18]

$$FOM = \sum_{i \in NS} \sum_{k \in \text{samp.}} |S_{ik}^{\text{exp}} - S_{ik}^{\text{basis}}|^p. \tag{3.1}$$

The first sum in eq. (3.1) expresses that the PSA does not only consider the signal of a single segment to reconstruct the interaction point. Generally, the neighboring segments (NS) surrounding the hit segments are used as they contain the largest amount of information on the γ-ray interaction point (c.f. sec. 1.3). The segments which are considered in the FOM form the so called neighbor pattern. After the definition of the neighbor pattern, the part of the trace which is used for the comparison is defined by the second sum running over a predefined selection of ADC-samples k. Furthermore, the metric p in eq. (3.1) has to be fixed. It is used for the calculation of deviation of the experimental trace S^{exp} from the basis trace S^{basis}.
Using an extensive grid search, the FOM is evaluated for all basis points in the hit segment[5]. Thus, 5000 to 12 000 basis points[6] are considered for the reconstruction of a single interaction position which leads to a long computation time [6]. More sophisticated search algorithms such as the Particle Swarm Optimization (c.f. [6]) are much faster. Nevertheless, the extensive grid search ensures that no additional errors due to the search loop occur as always the basis signal with the smallest FOM-value is found. Thus, the influence of the PSA algorithm on the position resolution is minimized. This is important as the PSA calibration experiment should be solely sensitive to the signal basis.

Current implementation of the PSA algorithm
According to eq. (3.1) the following parameters have to be set in the grid search algorithm: the segment neighbor pattern NS, the metric p and the samples which are included in the FOM. In the current implementation the FOM calculation spans over 50 samples (500 ns) starting at the beginning of the pulse at t_0.
For the metric p two different values have been used in the analysis: A least square comparison with $p = 2$ and a comparison with the square root, i.e. $p = 0.5$. Nevertheless, the results of the test experiments indicate that the influence of the metric on the performance of the PSA algorithm is weak. Thus, in the further analysis the square root metric is used.
A more critical parameter of the PSA algorithm is the choice of the neighboring segments which are included in the grid search. The experience of the test measurements show that the PSA performance deteriorates dramatically if net charge signals are included in the search loop. Therefore, they are not considered in the following. Two possible neighbor patterns, the cubic and the spherical configuration, are visualized in figs. 3.4 a) and b), respectively. The left patterns in fig. 3.4 illustrate that for net charge signals in the first crystal row all segments of the front row are included in the PSA. This approach is reasonable as these segments are not separated by the core contact. Furthermore, independent of the pattern shape, big patterns are preferred as a large number of segments contain more information about the interaction

[5] Due to the net charge signal, the segment containing the interaction point is never misidentified.
[6] Here a 1 mm cubic grid is assumed.

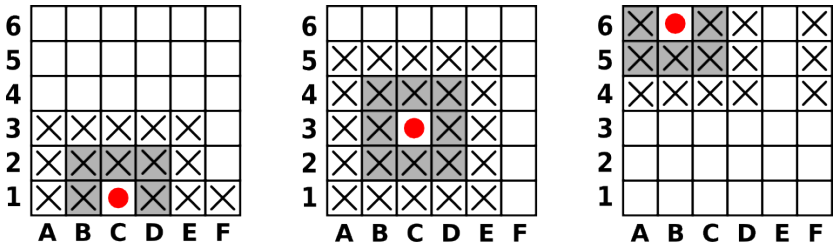

a) Cubic segment neighbor pattern.

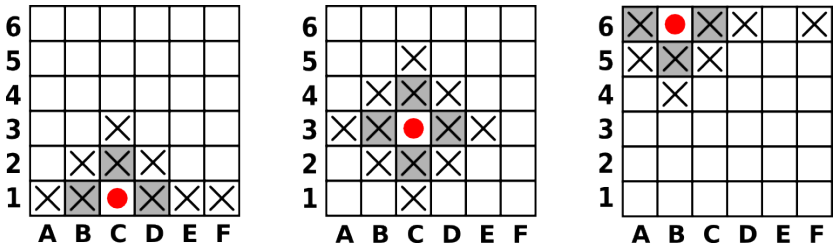

b) Spherical segment neighbor pattern.

Fig. 3.4: Segment neighbor pattern. The grid corresponds to the 36 segments of the AGATA crystal. On the horizontal axis the segment sectors are shown whereas the vertical axis corresponds to the crystal row (c.f. also fig. 1.2 c)). The red dots visualize the hit segment. All neighbors which are included in the PSA grid search are marked with black crosses. The first neighbors are additionally shaded. The figure is similar to [18].

position. Thus, considering only direct neighbors of the hit segment result by far in the poorest PSA position resolution. The pattern size is, however, limited due to the available computation time. Moreover, results show that the cubic pattern outperforms the spherical pattern. Hence, the cubic pattern which is shown in fig. 3.4 a) is used for the PSA of the test experiments.

3.2.2 Multi Hit Segments

As long there is only one hit segment in the crystal, the experimental traces can be easily compared to the basis traces as they are not influenced by further energy depositions in other segments. However, the situation changes if more than one segment features a net charge signal as HPGe detectors are not able to resolve two subsequent γ-ray interactions in time. Thus, the recorded signal is always the sum signal of both interactions. A schematic example is visualized in fig. 3.5. The interaction positions in two neighboring segments are marked with a red (number 1) and a green (number 2) circle, respectively. Their corresponding pulse shapes are displayed with the same colors and numbers. The sum signal is drawn in gray. The best reconstruction of the interaction positions could be achieved if the PSA algorithm would fit both interaction points at the same time with a multi-parameter fit. Nevertheless, the computation time of such an implementation is extremely high because every basis pulse shape of the first hit segment has to be combined with every pulse shape of the second hit segment. As the PSA is performed in real time, fitting both interaction points simultaneously with an extensive grid search is not possible. Fitting both interaction points separately and completely neglecting the other hit leads to a significant systematic error. Each reconstructed interaction point is always shifted towards the second hit segment. If e.g. two directly neighboring segments are hit, like in fig. 3.5, this PSA implementation leads to a clustering of the interaction points near the common segment boundary. Therefore, a different strategy is needed. Computation time requirements still force the new algorithm to reconstruct one

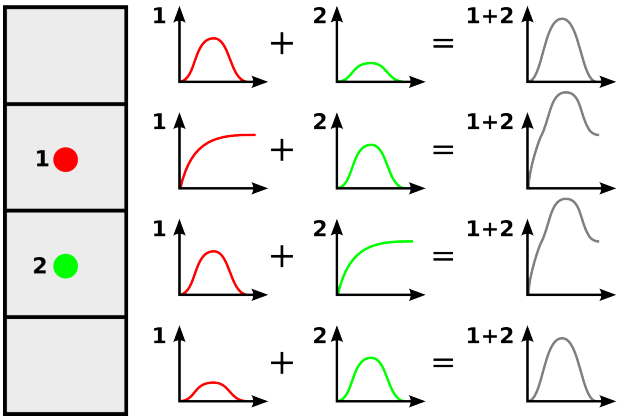

Fig. 3.5: On the left two interaction points e.g. resulting from a Compton scattering in a segmented HPGe detectors are shown in red and in green. It is assumed that their energy depositions are equal. Their pulse shapes are schematically drawn in the middle. The sum signals are plotted on the right.

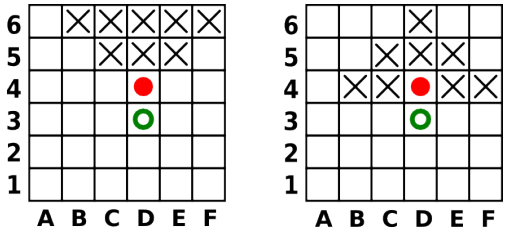

Fig. 3.6: Adapted segment neighbor pattern for multi hit-segments. The hit segments are marked with a red filled and a green open circle. The pattern for the analysis of the red filled interaction point are shown. On the left a cubic pattern is assumed while on the right the pattern has a spherical configuration.

interaction point after the other.
Two approaches have been implemented for the analysis of the test measurements:
The first uses an adapted neighbor pattern. It is created by assigning a weight to each neighbor, dependent on its distance to the hit segment. All neighbors which are situated directly at the hit segment are of order one (shaded neighbors in fig. 3.4), the neighbors which are a little bit further away have second order (unshaded segments in fig. 3.4) and so on. Finally, the extensive grid search is performed for all hit segments separately, taking into account only segments which have a lower order for the current hit segment than for any other hit segment. Fig. 3.6 shows the resulting adapted neighbor pattern for the cubic and spherical configuration, respectively. In this example two adjacent hit segments are considered.
The second algorithm uses a completely different approach as it does not change the neighbor pattern [31]: It first searches for the interaction position with the largest energy deposition and reconstruct its interaction point using the strategy for single hit segments (c.f. sec. 3.2.1), neglecting the other hit segments completely. Finally, the best fitting basis traces are subtracted from the experimental signals. These modified experimental signals are then used as input for the fit of the interaction point with the second highest energy. The procedure is recursively repeated for each energy sorted interaction position.
Comparing both methods, the recursive subtraction of the experimental trace leads to a better position resolution in the test measurements than the adapted neighbor pattern. Therefore, multi-hit segments are treated with the second approach in the analysis of the test experiments.

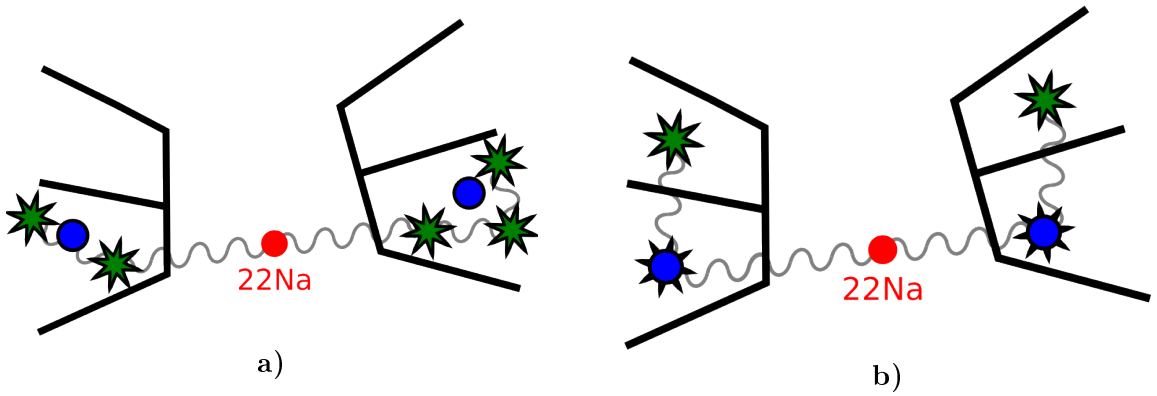

Fig. 3.7: Typical event signatures of the one hit-segment analysis, described in sec. 3.3.1 (**a**)) and the two hit-segment analysis, described in sec. 3.3.2 (**b**))

3.2.3 Higher Multiplicity Scenarios

Currently the PSA reconstructs only one interaction point per segment. It corresponds to the energy weighted barycenter. The reconstruction of multiple interaction points per segment is a much more challenging task: A reliable criterion is needed to determine the number of interaction points in the hit segment. It can be e.g. based on the segment energy [6]. Furthermore, the extensive grid search cannot be used as it is too time consuming. Thus, the FIPS[7] algorithm was developed which is capable to resolve more than one interaction point in one segment [6].
Nevertheless, the question arises whether it is necessary to reconstruct single interaction points. Currently the tracking algorithms for the γ-ray-path are still grouping interaction points which are closer than a certain distance together. Thus, the segment barycenter is in most cases sufficient. However, the Doppler correction capability can be increased significantly if instead of the barycenter the first interaction point can be reconstructed (c.f. 4.1.3). Therefore, the need for the treatment of multi hits in a segment is currently still under discussion [32]. In this thesis higher multiplicity scenarios are neglected.

3.3 Event Selections

The calibration experiment of the AGATA pulse shape analysis should consider as many different event types as possible since the occurring event signatures in AGATA are manifold. As the analysis is based on the angular correlation of the annihilation γ-rays of ^{22}Na, energies above 511 keV are not accessible. Energies below 511 keV are analyzable as the energy of one 511 keV γ-ray can be distributed over multiple segments resulting in different energies of the reconstructed barycenters. Sec. 3.3.1 presents events with exactly one hit segment per crystal corresponding to the highest possible energy whereas sec. 3.3.2 details the case of two hit segments.

3.3.1 One Hit Segment

The one hit-segment analysis requires events with both crystals featuring a total absorption of the annihilation γ-rays in a single segment (c.f. fig. 3.7a)). Therefore, exactly one net charge signal per crystal is allowed with a total energy deposition of about $E = 511$ keV. The energy cut is defined by the ellipse centered around the anti-correlation peak in fig. 2.5. This tight

[7] FIPS: Fully Informed Particle Swarm

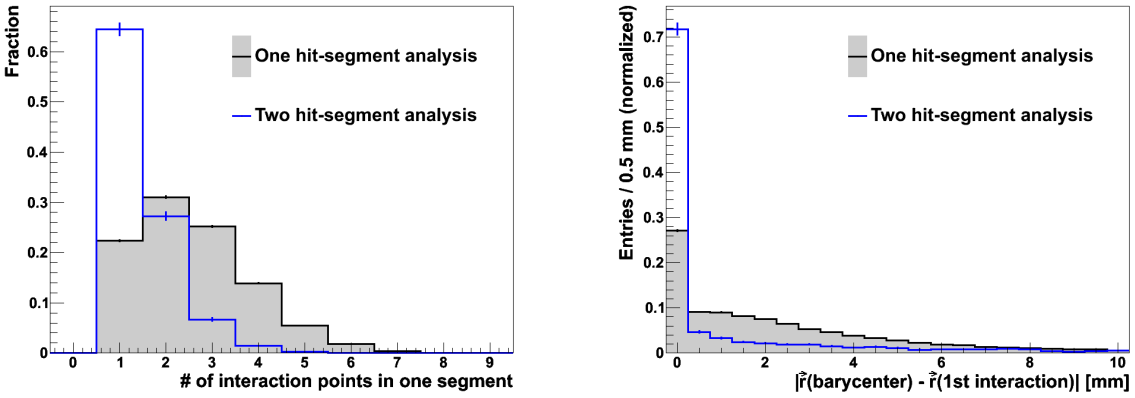

Fig. 3.8: a) The number of interaction points in one segment which are packed together to the energy weighted barycenter. In the case of the two hit-segment analysis the number of hits in the Compton segment is shown. **b)** The distance between the barycenter and the first interaction point for the same segments.

energy window and the coincidence condition of the annihilation γ-rays lead to a very efficient background discrimination which is a big advantage of the calibration experiment.
As the Compton cross section dominates at $E_\gamma = 511\,\text{keV}$ in germanium [33], most of the annihilation γ-rays of ^{22}Na deposits their energy in more than one interaction. Thus, it is likely that multiple interaction points in the hit segment occur. To gain a deeper insight a Geant4 simulation was performed. The results are visualized in fig. 3.8. Fig. 3.8 a) shows the number of interaction points in the hit segment. As expected from the interaction cross sections of γ-rays in germanium the maximum of the distribution is at two to three interactions in the one hit-segment analysis. Thus, the energy weighted barycenter of all interactions and the first interaction point do not coincide. This leads in most cases to a non negligible distance between the barycenter and the first interaction position (c.f. fig. 3.8 b)). As a result, the one hit-segment analysis studies the performance of the reconstruction of the barycenter and not of single interaction points.
Apart from that, the one hit-segment analysis has the advantage that the single hit segment can be treated with the simplest PSA algorithm (c.f. sec. 3.2.1). Thus, the position error resulting from the implementation of the PSA algorithm is kept small. Nevertheless, the basis pulse shapes are calculated for single γ-ray interactions and not for the energy weighted mean value of multiple interactions. Therefore, it is implicitly assumed that the pulse shapes of a single interaction and the barycenter coincide.

3.3.2 Two Hit Segments

To get rid of the effects caused by the barycenter formation, a second event selection is introduced. The basic idea is to analyze events which feature a Compton scattering in one segment and a subsequent photoelectric absorption in another segment (c.f. fig. 3.7 b)). Consequently, the second event selection of the PSA calibration experiments deals with events having exactly two hit segments per crystal with a total energy deposition of about $E_\text{tot} \approx 511\,\text{keV}$. As indicated in fig. 3.8 a) this event selection considers predominantly events with only one hit in the segment containing the Compton scattering. As a result, the barycenter coincides with the first interaction point in most cases. This can also be seen in fig. 3.8 b) showing that the distance between the barycenter and the first interaction is zero for over 70% of the selected events. Consequently, with the two hit-segment analysis the position resolution of

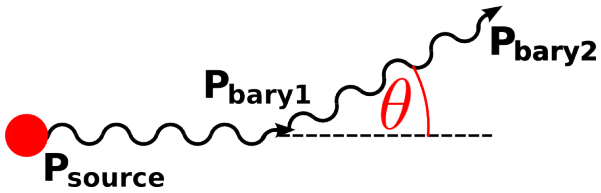

Fig. 3.9: Compton scattering of a γ-ray emitted by a source at P_{source}. The γ-ray undergoes a single Compton scattering at $P_{\text{bary 1}}$ and finally a photoelectric absorption at $P_{\text{bary 2}}$.

single interaction points can be studied.
To select Compton events the following cuts are imposed:

- For each crystal, exactly two hit segments with a total energy deposition of $\sum E_{\text{segments}} \approx 511\,\text{keV}$ are required. The energy cut is defined according to the ellipse in fig. 2.5. Due to this tight cut, fake events e.g. resulting from the bow effect (c.f. sec. 2.3.2) are sufficiently rejected.

- To determine the segment with the Compton scattering the time order of the segments, i.e. the scattering path has to be known. In the following the segment which is hit first is called Compton segment whereas the second segment containing the photoelectric absorption is called photo segment. The straight forward approach to reconstruct the scattering path is based on the scattering angle θ (c.f. fig. 3.9). θ can be determined with two different methods. On the one hand, it can be calculated with the Compton formula [34]

$$\cos(\theta_{\text{energy}}) = 1 - \frac{m_e c^2 \cdot E_{\text{Compton}}}{E_\gamma \cdot (E_\gamma - E_{\text{Compton}})}, \tag{3.2}$$

  with the incident γ-ray energy $E_\gamma = 511\,\text{keV}$, the rest mass of the electron $m_e c^2$ and the energy deposition E_{Compton} in the Compton segment. On the other hand, it can be estimated geometrically with the source position P_{source} and the two reconstructed barycenters $P_{\text{bary 1,2}}$

$$\cos(\theta_{\text{geo}}) = \frac{\overrightarrow{P_{\text{source}}P_{\text{bary 1}}} \cdot \overrightarrow{P_{\text{bary 1}}P_{\text{bary 2}}}}{|\overrightarrow{P_{\text{source}}P_{\text{bary 1}}}| \cdot |\overrightarrow{P_{\text{bary 1}}P_{\text{bary 2}}}|}. \tag{3.3}$$

  θ_{energy} and θ_{geo} can be calculated according to eqs. (3.2) and (3.3) for the two possible scattering paths $P_{\text{source}} - P_{\text{bary 1}} - P_{\text{bary 2}}$ and $P_{\text{source}} - P_{\text{bary 2}} - P_{\text{bary 1}}$. Thus, it could be assumed that the path with the smaller difference $|\theta_{\text{energy}} - \theta_{\text{geo}}|$ corresponds to the correct combination. However, the failure rate of this method is quite high as the Compton formula features an ambiguity for γ-rays with energies ranging from 255 keV to 700 keV [35]. This is further illustrated in fig. 3.10. It shows a 600 keV γ-ray which undergoes a single Compton scattering, followed by a photoelectric absorption. According to the Compton formula, both displayed scattering paths are possible. Therefore, a different method to determine the time order of the interaction positions is needed.
  To improve the situation, the mean free path of γ-rays in germanium is included in the decision [35]. It can be compared to the distance between the Compton interaction and the photoelectric absorption because γ-rays with a higher energy have a longer mean free path. Nevertheless, due to the finite position resolution of the PSA and the packing of the interaction points to the energy weighted barycenter the misidentification rate of the scattering path is still too high.
  Furthermore, both methods feature an additional, significant drawback: Their performance is strongly dependent on the position resolution of the PSA. Therefore, a com-

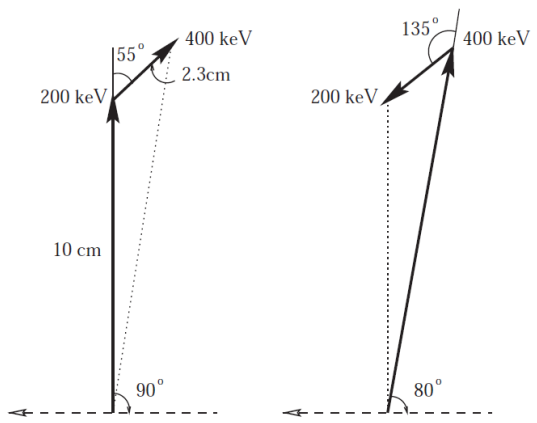

Fig. 3.10: An example for the ambiguity of the Compton formula. For the incident γ-ray with an energy of 600 keV both displayed scattering paths are allowed according to the Compton formula. The figure is taken from [35].

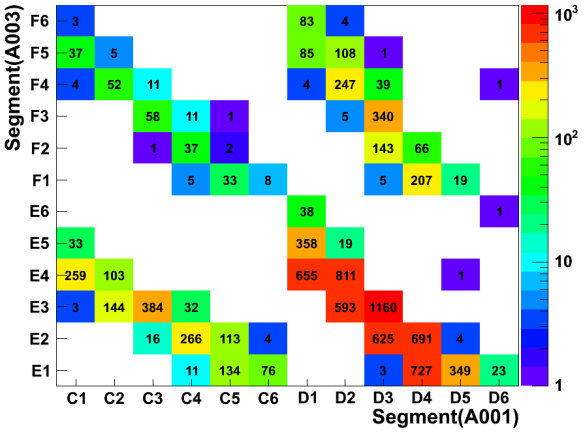

Fig. 3.11: The look-up table simulated with Geant4 for the symmetric test measurement. On the x- and y-axis the segments of the A001 and the A003 crystal are plotted. If the number of hits for a segment combination exceeds 100 the combination is accepted in the analysis.

pletely different method is chosen to determine the time order of the interaction points which just relies on the geometry of the setup. Due to the angular correlation of the two 511 keV annihilation γ-rays not every Compton segment combination of the two crystals is geometrically possible. This method utilizes that the two Compton segments and the source should be positioned on a straight line. Due to the complex geometry a Geant4 simulation is performed to determine all possible segment pairs. Fig. 3.11 shows the number of hits for each segment combination resulting from a Geant4 simulation of the symmetric test experiment with 30 million simulated ^{22}Na decays. A segment combination is accepted in the analysis if the segment pair is hit more than 100 times in coincidence[8]. With the help of this look-up table the Compton ambiguity can be solved. As a result, about 94% of the scattering paths are identified correctly. However, one drawback of the look-up table is that lots of good Compton events are rejected as only unambiguous scatterings paths are allowed to keep the misidentification rate minimal.

- The energy E_{Compton} deposited in the Compton segment must not be larger than the Compton edge $E_{\text{Compton edge}} = 340$ keV. This cut reduces background events featuring two hits in the Compton segments as multiple hits are the only possibility of exceeding the Compton edge.

- The criteria stated so far are suitable to select Compton scattered events. Taking additionally the geometry of the crystals into account, the fraction of single interactions is increased. As the initial and the Compton scattered γ-ray are reconstructed in the same crystal the scattering angle of the γ-ray is limited due to the active detector volume. Thus, an additional cut on the energy E_{Compton} is introduced which is equivalent to a cut on the scattering angle. The maximal allowed energy E_{Compton} is set to 40 keV below the Compton edge of the annihilation γ-rays because energies near the Compton edge have high scattering angles and backscattering out of the detector is likely in this case. Thus, if a γ-ray deposits more than 300 keV in the Compton segment and is scattered into a

[8] The threshold 100 was tuned to get the best performance of the selection.

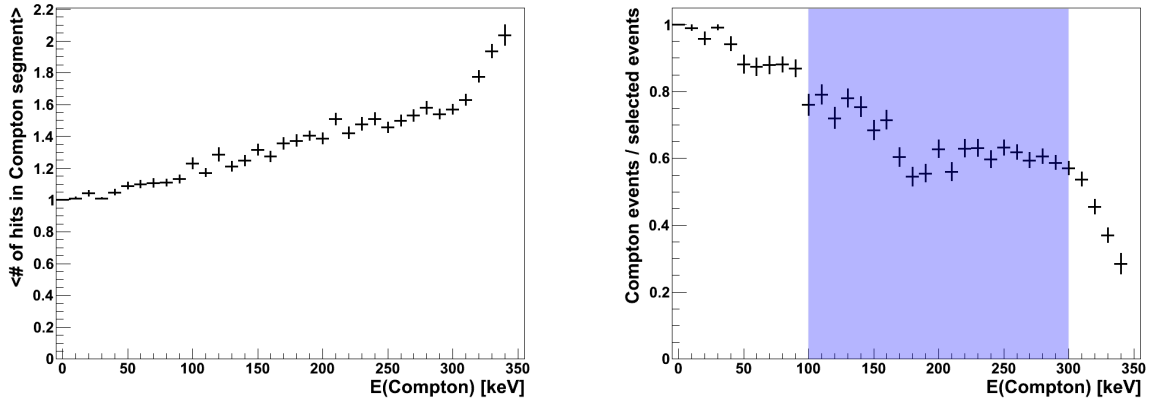

a) b)

Fig. 3.12: a) The mean number of hits in the Compton segment as a function of the energy in the Compton segment. **b)** The performance of the Compton selection versus the Compton segment energy.

neighboring segment of the same crystal, it usually features multiple hits in the Compton segment. This behavior is confirmed by fig. 3.12 a) which shows the mean number of interaction points in the Compton segment as a function of the energy deposited in the Compton segment. The number of hits increases rapidly near the Compton edge.

- A minimal energy threshold of 100 keV is set because the PSA resolution is energy dependent. As lower energy depositions have a small signal amplitude, the reconstruction of the interaction points with the PSA becomes more and more difficult. Hence, a lower bound for the energy was introduced to ensure that the energy dependence of the PSA does not dominate over the influence of the signal basis in the position resolution.
  In summary, the energy E_{Compton} of the Compton segment is restricted to the interval $E_{\mathrm{Compton}} \in [100\,\mathrm{keV}, 300\,\mathrm{keV}]$.

Fig. 3.12 b) shows the performance of the event selection determined by a Geant4 simulation. It displays the ratio between the number of selected good Compton scatterings (single interaction in the Compton segment, correctly identified scattering path) and the total number of selected events. The shaded band in fig. 3.12 b) indicates the energy region selected by the cuts. The overall ratio between $E_{\mathrm{Compton}} = 100\,\mathrm{keV}$ and $E_{\mathrm{Compton}} = 300\,\mathrm{keV}$ is about 63%. Generally the shape of the curve is anti-correlated to the shape of the mean number of interaction points in the Compton segment, displayed in fig. 3.12 a). Hence, the main background is composed of events with more than one interaction point in the Compton segment. The gradients in figs. 3.12 a) and b) can be explained as increasing energy depositions in the Compton segment lead to an increasing probability for multiple hits in the segment.
A positive aspect of the described event selection is that it does not depend on the reconstructed interaction positions. Thus, the position resolution does not hamper the performance of the event selection and the obtained position resolution is not biased by the Compton selection at the same time. Hence, to keep the analysis unbiased, an additional upper limit on $|\theta_{\mathrm{energy}} - \theta_{\mathrm{geo}}|$ was not introduced as it depends on the PSA position resolution, although the cut would increase the fraction of true single interactions dramatically. An even more sophisticated selection will be discussed in sec. 5.5.

3.4 Determination of the Position Resolution

After discussing the event selection of the calibration experiment, the analysis strategies to determine the position resolution of the selected events are detailed. The following description is based on a Geant4 simulation of the symmetric test measurement[9]. As a reminder, the symmetric test experiment features two AGATA crystals (A001 and A003) with the source being positioned in their center (c.f. fig. 2.3). Due to the symmetric setup both crystals are treated in the same way. Thus, unless otherwise stated, the position resolution of both crystals is assumed to be the same.

3.4.1 Concept

First of all, the concept of the calibration experiment is illustrated with a Geant4 simulation. Figs. 3.13 a) and b) show the distribution of the first interaction points of the two annihilation γ-rays which are selected according to the one hit-segment analysis (c.f. sec. 3.3.1). In fig. 3.13 a) a front view of the crystals is shown whereas fig. 3.13 b) visualizes a side view. Additionally some of the interaction points of the same event are connected with a straight line. As expected from the angular correlation of the 511 keV γ-rays, these lines are all crossing at the source position.
In figs. 3.13 c) and d) the same distributions are shown, but instead of the first interaction points the barycenters of the one hit-segment analysis are displayed. As it is likely that the barycenter does not coincide with the first interaction point (c.f. figs. 3.8 a) and b)), the barycenters and the source position need not be positioned on a straight line. Thus, the lines are not crossing at one point, although they are quite close to it. The influence of the packing of the segment's interaction points to their energy weighted barycenter is also visible in the distribution. As the barycenter tends to cluster in the segment center, the density of the interaction points drops near the segmentation lines.
The corresponding distributions of the two hit-segment analysis are displayed in figs. 3.13 e) and f). They show the barycenters of the Compton segment. Analogous to the one hit-segment analysis the lines are nearly crossing at the source position. However, a few outliers are visible. They are caused by misidentified scattering paths of the γ-ray. Furthermore, the clustering of the barycenters is not present for Compton events since the two hit-segment analysis selects predominantly single interactions.
So far, the position resolution of the simulated interaction points is perfect. If it is set to a finite value the smearing of the lines around the source position increases. As an example the influence of the position resolution is illustrated in figs. 3.14 a) and b) showing the results of the one hit-segment analysis with a 3 mm position smearing[10]. Comparing the distribution of the lines around the source position with and without the position uncertainty, it is obvious that the smearing of the lines can be used to determine the PSA position resolution.

3.4.2 Fitting the Source Position and Definition of the Distance Spectrum

As the smearing of the lines near the source is directly connected to the position uncertainty of the reconstructed interaction points, a quantitative method to characterize the smearing is needed.

Fitting the source position
First of all, the exact source position has to be determined has it is essential for the analysis. As the source location is not known for the test measurements, it has to be extracted from the

[9] The asymmetric test experiment is handled analogously (c.f. chap. 5).
[10] Details on the position smearing can be found in sec. 3.4.3.

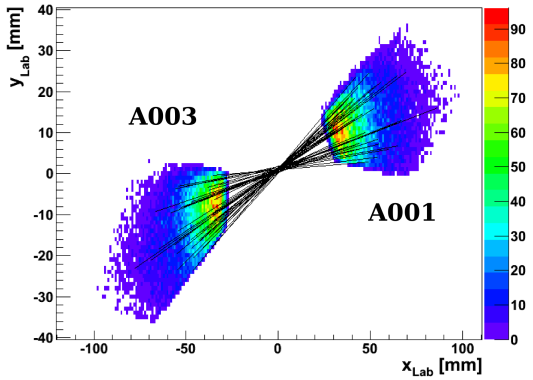

a) First interaction points of the one hit-segment analysis

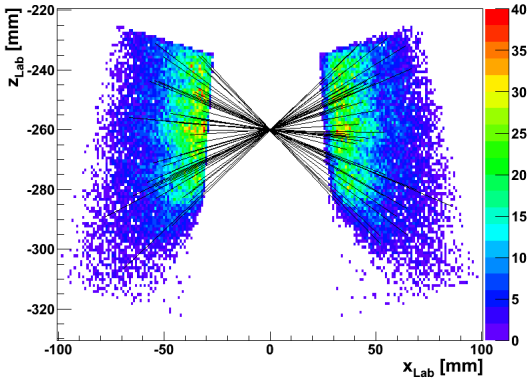

b) First interaction points of the one hit-segment analysis

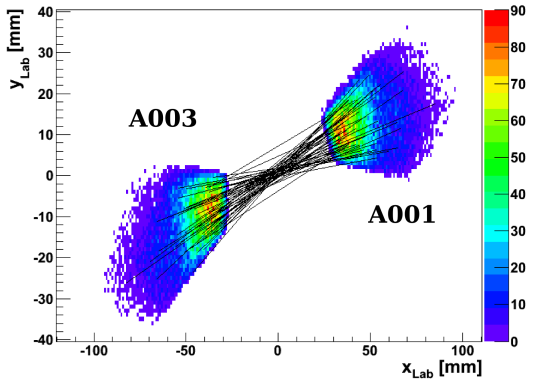

c) Barycenters of the one hit-segment analysis

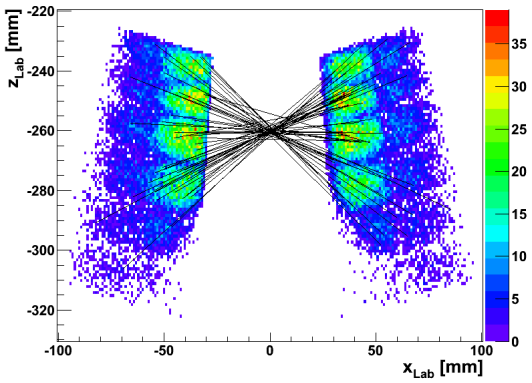

d) Barycenters of the one hit-segment analysis

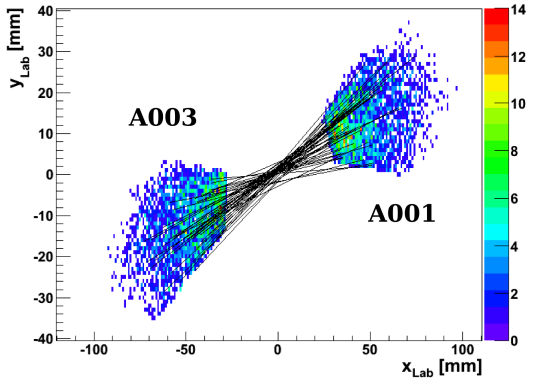

e) Barycenters of the Compton segment of the two hit-segment analysis

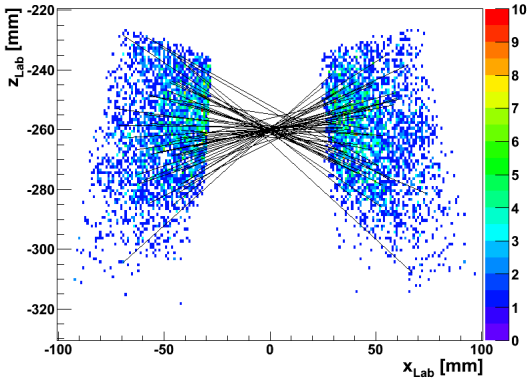

f) Barycenters of the Compton segment of the two hit-segment analysis

Fig. 3.13: Simulated spatial distributions of the interaction points for the symmetric test experiment with perfect position resolution. The left column shows a front view of the crystals whereas the right column present a side view of the same events.

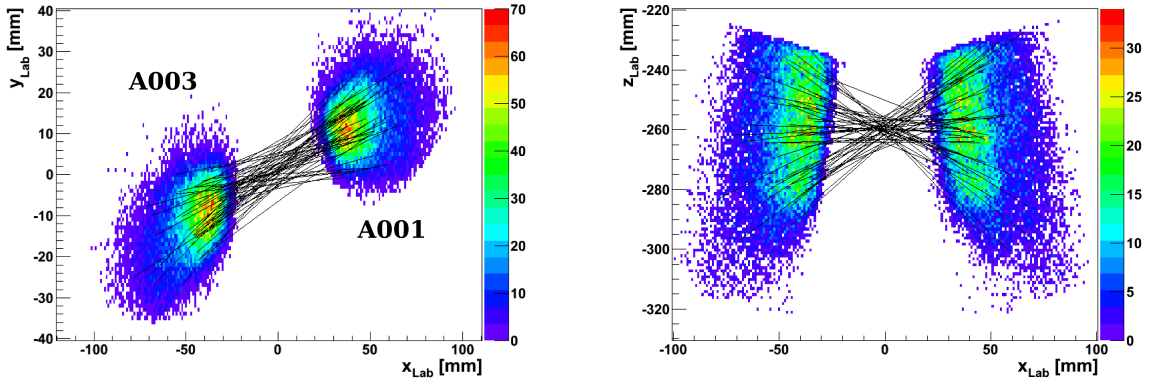

a) b)

Fig. 3.14: Simulated distribution of the barycenters for the symmetric test experiment with a position smearing of 3 mm. The left column shows a front view of the crystals whereas the right column present a side view.

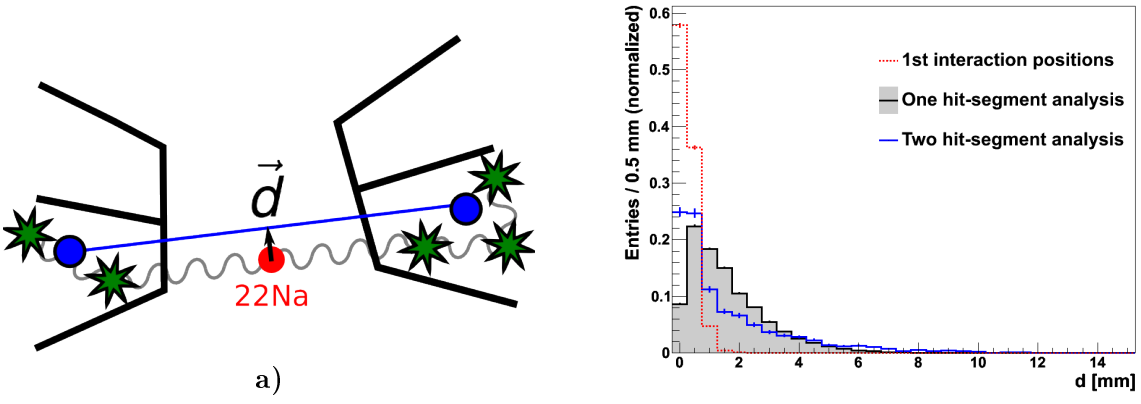

a) b)

Fig. 3.15: **a)** The definition of the vector $\vec{d}$. **b)** The distribution of the quantity $d = |\vec{d}|$ for different event types. All distance spectra are obtained by a Geant4 simulation.

data, i.e. from the reconstructed interaction points. The most exact method to determine the source position is a global fit. For this purpose the vector $\vec{d}$ is introduced. It represents the shortest distance between the source position and the straight line connecting corresponding barycenters which pass the event selection. This is illustrated in fig. 3.15 a). The length of the vector $\vec{d}$ is given by the source position $\vec{s} = (s_1, s_2, s_3)$ and the line $l : \vec{x} = \vec{a} + \lambda \cdot \vec{u}$ $(\lambda \in \mathbb{R})$

$$|\vec{d}|^2 = \sum_{i=1}^{3}(s_i - a_i)^2 - \frac{1}{u_1^2 + u_2^2 + u_3^2} \cdot \left[\sum_{i=1}^{3} u_i(s_i - a_i)\right]^2 . \tag{3.4}$$

The source position is determined by minimizing the mean distance

$$\langle|\vec{d}|\rangle = \frac{1}{N_{\text{events}}} \sum_{\text{events}} |\vec{d}_i|, \tag{3.5}$$

with respect to the source $\vec{s} = (s_1, s_2, s_3)$. The sum in eq. (3.5) includes all selected events. The fit of the source position was executed with the Minuit package [36] which is included in the ROOT framework [37].
To test the precision of the fit a Geant4 simulation with a position uncertainty of 2 mm was

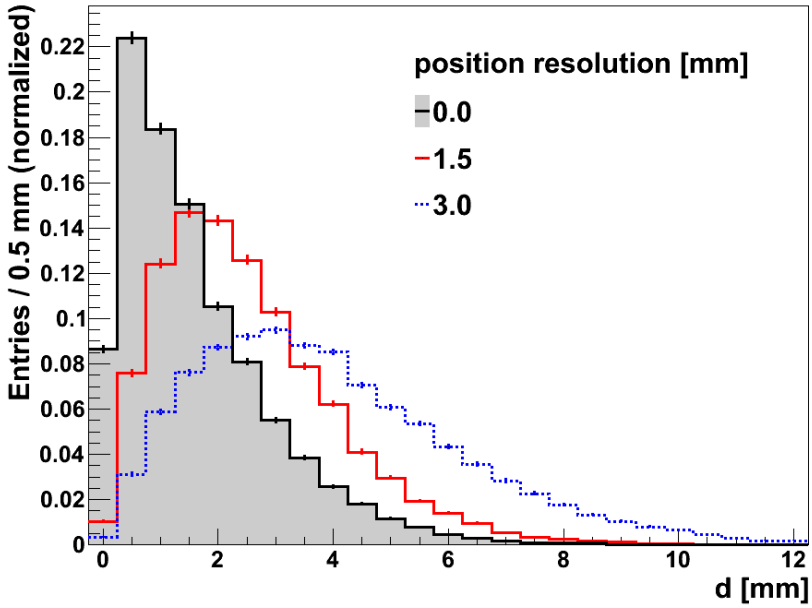

Fig. 3.16: Influence of the position smearing on the distance spectrum. All spectra are simulated with Geant4.

performed. The fitted and the simulated source position coincide within 0.3 mm which is sufficient for the further analysis. Nevertheless, in reality additional systematic errors can deteriorate the source position resolution. E.g. the reconstructed barycenters can feature a systematic shift in one direction instead of being isotropically distributed around the actual barycenter.

Definition of the distance spectrum

To quantify the smearing of the connection lines around the source, the distance $d = |\vec{d}|$ of the lines to the fitted source position is used. Fig. 3.15 b) shows a histogram of the obtained distances d for the various event types. All events are simulated with Geant4 assuming a perfect position resolution. The red dotted line visualizes the distribution for the first interaction points. As expected it is quite close to zero. The shaded area displays the resulting distance spectrum of the one hit-segment analysis. It is broader compared to the first interaction points due to the influence of the barycenter (c.f. sec. 3.3). In contrast to the one hit-segment analysis, the distance spectra of the two hit-segment analysis (blue solid curve) has its peak at zero because the latter analysis selects mostly single hit events. However, the tail of the two hit-segment analysis is more pronounced as the scattering path of the γ-ray can be misidentified, resulting in large d-values.

In general, the shape of the distance spectra is directly connected to the smearing of the lines near the source position and therefore to the position resolution. This is illustrated in fig. 3.16 showing the simulated distance spectra for various resolutions. Obviously the distance spectrum is sensitive to the position resolution of the interaction points. Thus, it can be used to determine the position resolution in a quantitative way.

3.4.3 Including the Position Resolution in the Simulation

The determination of the position resolution is based on the comparison of the experimental distance spectrum and simulated distance spectra with different position smearings. Therefore, a quantitative analysis requires an accurate model for the position uncertainty.

Distributions for position smearing

The simplest approach to include a finite position resolution in the simulation is to smear the Geant4 barycenters with a Gaussian distribution around their true coordinates $\vec{x}_{\text{true}}$. Furthermore, it is assumed that the position resolution in all three directions x, y, and z is the same as no better model exists. Thus, the smeared barycenters $\vec{x}$ are distributed according to the probability density function

$$\begin{aligned} P_G(\vec{x}|\sigma) &= \frac{1}{(2\pi)^{3/2}\sigma^3} \cdot \exp\left(-\frac{(x-x_{\text{true}})^2}{2\sigma^2}\right) \cdot \exp\left(-\frac{(y-y_{\text{true}})^2}{2\sigma^2}\right) \cdot \exp\left(-\frac{(z-z_{\text{true}})^2}{2\sigma^2}\right) \\ &= \frac{1}{(2\pi)^{3/2}\sigma^3} \cdot \exp\left(-\frac{(\vec{x}-\vec{x}_{\text{true}})^2}{2\sigma^2}\right), \end{aligned} \tag{3.6}$$

with σ being the standard deviation of the Gaussian distribution.
In spherical coordinates r, θ, and ϕ eq. (3.6) reads

$$P_G(r,\theta,\phi|\sigma) = r^2 \sin\theta \cdot \frac{1}{(2\pi)^{3/2}\sigma^3} \cdot \exp\left(-\frac{r^2}{2\sigma^2}\right) \tag{3.7}$$

with $r^2 \sin\theta$ being the volume element for spherical coordinates. Thus, the distribution of the distance $r = |\vec{x} - \vec{x}_{\text{true}}|$ between the smeared point $\vec{x}$ and the true point $\vec{x}_{\text{true}}$ is obtained by integration over the angles θ and ϕ

$$\begin{aligned} P_G^{rad}(r|\sigma) &= \int_0^{2\pi} d\phi \int_0^{\pi} d\theta \; r^2 \sin\theta \cdot \frac{1}{(2\pi)^{3/2}\sigma^3} \cdot \exp\left(-\frac{r^2}{2\sigma^2}\right) \\ &= \frac{4\pi}{(2\pi)^{3/2}\sigma^3} \cdot r^2 \cdot \exp\left(-\frac{r^2}{2\sigma^2}\right). \end{aligned} \tag{3.8}$$

The second smearing distribution which is used in the analysis is a Laplace distribution as previous experiments have shown that the reconstructed barycenters tend to be leptokurtic distributed [6]. Its one dimensional probability density function can be written as

$$P_L^{1D}(x|\sigma) = \frac{1}{\sqrt{2}\sigma} \cdot \exp\left(-\sqrt{2} \cdot \frac{|x - x_{\text{true}}|}{\sigma}\right). \tag{3.9}$$

The quantity σ is again the standard deviation. Comparing the Laplace distribution to a Gaussian distribution with the same standard deviation, the Laplace distribution features a sharper peak and a more pronounced tail (c.f. fig. 3.17). In three dimensions the probability function of the Laplace distribution can be expressed as

$$P_L^{3D}(\vec{x}|\sigma) = \frac{1}{2^{3/2}\sigma^3} \cdot \exp\left(-\sqrt{2} \cdot \frac{|x - x_{\text{true}}|}{\sigma}\right) \cdot \exp\left(-\sqrt{2} \cdot \frac{|y - y_{\text{true}}|}{\sigma}\right) \cdot \exp\left(-\sqrt{2} \cdot \frac{|z - z_{\text{true}}|}{\sigma}\right). \tag{3.10}$$

For two dimensions and $\vec{x}_{\text{true}} = 0$ the result is visualized in fig. 3.18 b). In contrast to the Gaussian distribution displayed in fig. 3.18 a), the Laplace distribution is not radial symmetric. This is a direct result of eq. (3.10) as the probability function cannot be written in terms of $|\vec{x} - \vec{x}_{\text{true}}|$. Consequently, a different distribution is chosen for the Laplace position smearing: Analogously to eq. (3.8) a radial symmetric Laplace distribution can be written as[11]

$$P_L^{rad}(r|\sigma) = \frac{\sqrt{2}}{\sigma^3} \cdot r^2 \cdot \exp\left(-\sqrt{2} \cdot \frac{r}{\sigma}\right). \tag{3.11}$$

[11] The normalization factor $\mathcal{N} = \frac{\sqrt{2}}{\sigma^3}$ is given by $\int_0^{\infty} dr P_L^{rad}(r|\sigma) = 1$.

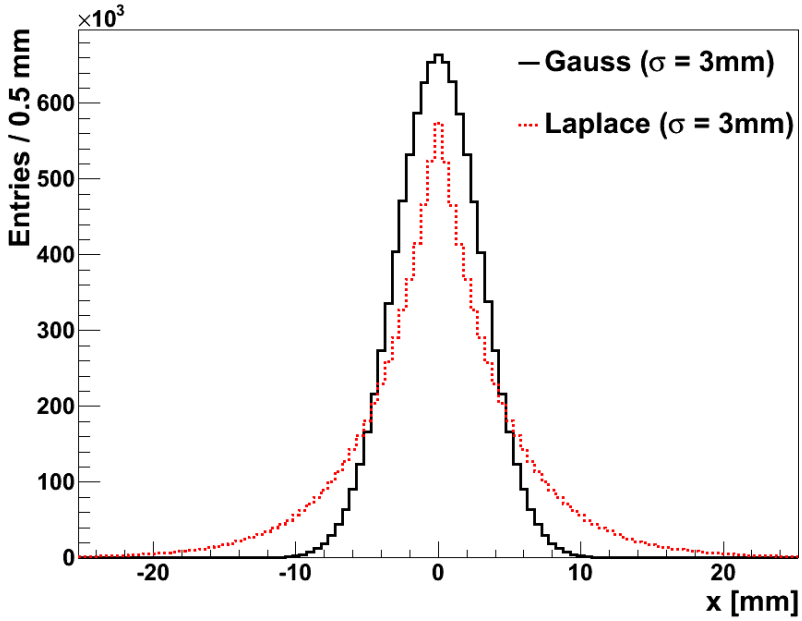

Fig. 3.17: One dimensional Gaussian and Laplace distribution with the same standard deviation σ. The Laplace distribution is leptokurtic compared to the Gaussian. Note that both distributions have the same number of entries.

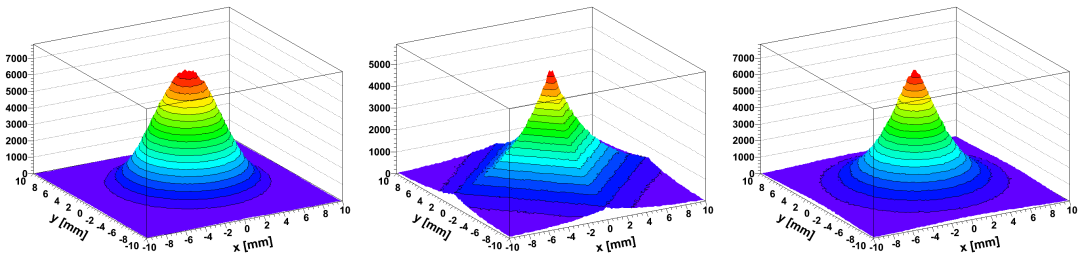

a) **b)** **c)**

Fig. 3.18: Two dimensional projections of possible distributions used for the position smearing. **a)** Two dimensional Gaussian distribution. **b)** Resulting distribution if the x- and y-coordinate follow an independent Laplace distribution. **c)** Distribution following eq. (3.11) and featuring an isotropic direction.

Therefore, to simulate a Laplace-shaped resolution the radius is smeared according to eq. (3.11) whereas the direction is chosen isotropically. The resulting two dimensional distribution is shown in fig. 3.18 c). In contrast to fig. 3.18 b), it features a radial symmetry. In the following this symmetric distribution is used to smear the interaction points according to a Laplace probability density function.

Definition of the position resolution
The position resolution is defined as the standard deviation of the distribution which is used to smear the simulated interaction points. This definition is preferred to the more common convention which uses the FWHM as a measure of resolution because it provides a better comparability between the Gaussian and the Laplace distribution (c.f. fig. 3.17). This is due to the standard deviation being a fundamental property of a distribution while the FWHM is strongly shape dependent. As an example the FWHM of a one dimensional Gaussian and Laplace distribution is given by the following formulas

$$\mathrm{FWHM(Gauss)} = 2\sqrt{2\ln 2}\cdot\sigma \approx 2.35\cdot\sigma \quad \leftrightarrow \quad \mathrm{FWHM(Laplace)} = \sqrt{2}\ln 2\cdot\sigma \approx 0.98\cdot\sigma. \tag{3.12}$$

Additional constrains
To receive a more realistic position smearing additional constrains are introduced. The PSA algorithm reconstructs all interaction points inside the germanium crystal. Thus, the smearing implemented in the simulation, is designed to allow only interaction positions inside the active detector volume. In contrast, smearing out of the hit segment is accepted because the segmentation lines are not known precisely and therefore not perfectly implemented in the Geant4 simulation (c.f. sec. 2.4). Thus, allowing the interaction points be positioned outside the segment this uncertainty is taken into account. Apart from that, the grid of the pulse shape basis can be considered by positioning the smeared barycenters on the nearest grid point. The ADL basis is calculated on a cubic grid with 2 mm spacing whereas the JASS basis is simulated on a 1 mm cubic grid. Thus, the spacing has the same order of magnitude as the PSA position resolution. Nevertheless, by default the grid is ignored to speed up the analysis.

3.4.4 First Estimation using the Symmetric Setup

The straight forward way to estimate the PSA position resolution is to determine characteristic parameters from simulated distance spectra with different position smearing and compare them to the values of the experimental spectrum. Figs. 3.19 a) and b) display simulated distance spectra for various position resolutions σ according to a Gaussian and a Laplace distribution, respectively. Note that both crystals are treated equally, i.e. both feature the same position resolution. To get an idea which parameters are suitable for the analysis, characteristic quantities of these spectra are plotted in figs. 3.19 b) and c) as a function of the position resolution σ. The standard deviation of the distance spectrum does not seem to be strongly correlated to the position resolution. Furthermore, the position of the maximum is also not very suitable as its determination is challenging. Choosing just the bin with the largest number of entries for the maximum position leads to a large error which corresponds to the bin width. Thus, its distribution as a function of σ is not uniform. Fitting the maximum position is too complicated as the peak structure of the distance spectrum cannot be described with a simple fit function. Furthermore, this quantity does not consider all entries of the distance spectrum, i.e. all reconstructed interaction points passing the event selection. Contrary, the mean and the median of the distance spectrum take all entries into account and are independent of the binning of the histogram. Furthermore, both show a strong correlation to σ. Hence, the mean and the median are suitable parameters for the determination of the PSA position

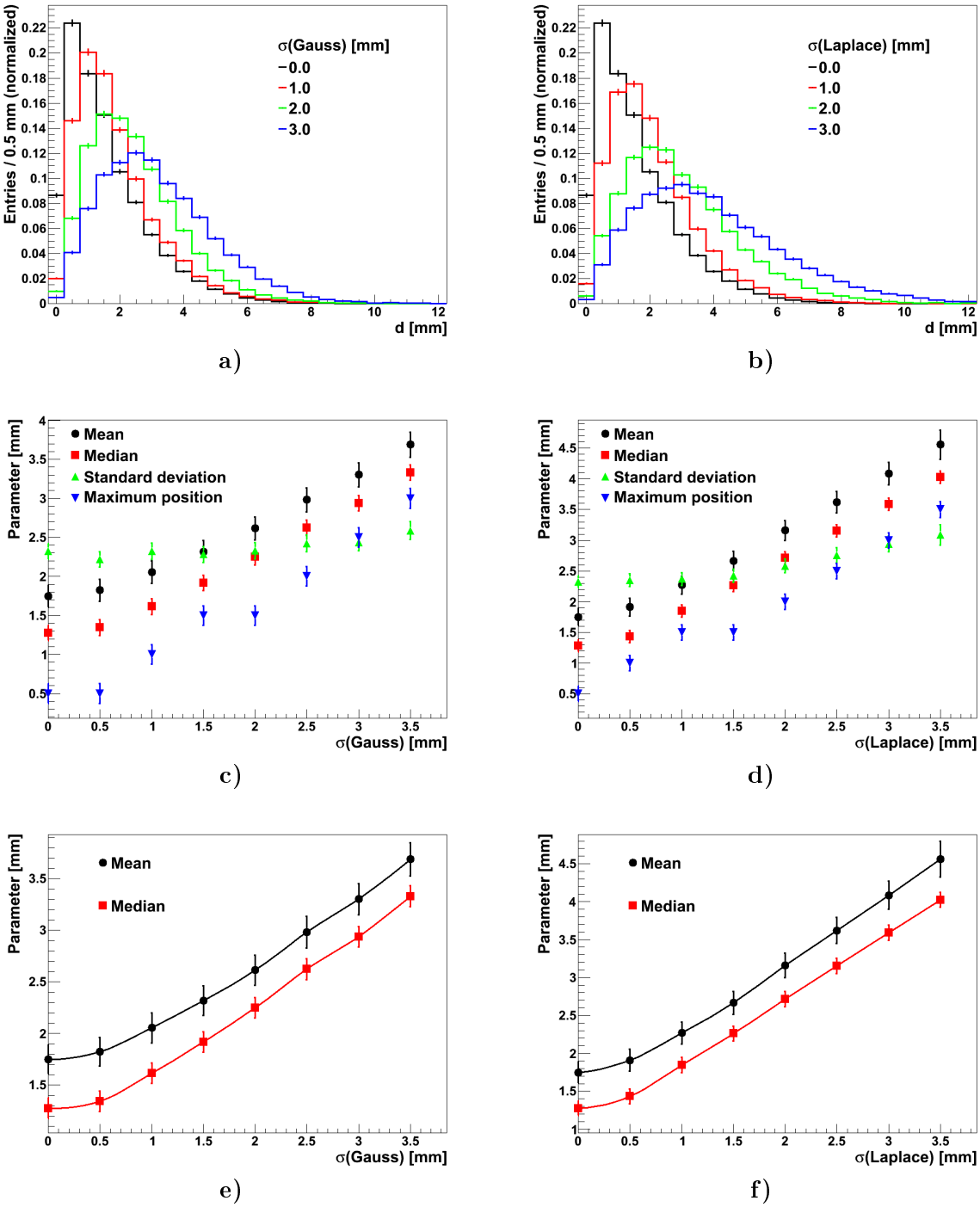

Fig. 3.19: **a)** and **b)** Simulated distance spectra for various values of the position resolution. **c)** and **d)** Characteristic parameters of these distance spectra. **e)** and **f)** Suitable parameters for the determination of the PSA position resolution. The errors of the mean and the median are visualized 10 times larger. In the left column a Gaussian position smearing is used while the right column is obtained using a Laplace-smearing.

resolution. For a better overview their dependency on the standard deviation of a Gaussian and a Laplace position smearing distribution is again illustrated in figs. 3.19 e) and f). The smaller slope at small σ is explained as the influence of the barycenter dominates over the influence of the smearing distribution there. Note that the statistical error bars have been increased by a factor of 10 to make them properly visible. Furthermore, the obtained parameters are connected with cubic splines. Hence, the position resolution of a calibration experiment can be determined by calculating the mean or the median of its distance spectrum. Subsequently figs. 3.19 e) and f) can be used to translate the obtained value into a resolution. However, the evaluation of the experimental spectra is safer using the median as it is more robust against outliers compared to the mean value[12] [38].
Nevertheless, this method to determine the PSA position resolution features one significant drawback. There is no possibility to decide whether the smearing assumed in the simulation is compatible with the real distribution of the reconstructed barycenters around their true coordinates. Thus, there is no information whether a Gaussian or a Laplace distribution is more likely. While a position resolution can be obtained for both, it is not possible to decide which is correct. Therefore, a better algorithm to determine the position resolution which takes the full spectral shape of the distance spectrum into account is presented in sec. 3.4.5.

3.4.5 Fitting the Distance Spectrum

In contrast to the method described in sec. 3.4.4, the second possibility to determine the position resolution analyzes the shape of the distance spectrum. Thus, in principle, the assumed smearing distribution of the simulated interaction points can be checked.

Fit strategy
The second method is based on a fit of the simulated distance spectrum to the experimental distance spectrum. The smearing σ, applied to the simulated barycenters, is varied until the simulated distance spectrum coincides with the experimental distance spectrum. Analogous to the first estimation of the position resolution, described in sec. 3.4.4, it is assumed that the position uncertainty of both crystals is the same. To quantify how well the simulated distance spectrum matches the measured distance spectrum, both histograms are compared using Pearson's χ^2-test. Its figure of merit is given by [39]

$$\chi^2 = \frac{1}{N^{\mathrm{sim}} N^{\mathrm{exp}}} \sum_{i=1}^{N_B} \frac{(N^{\mathrm{sim}} n_i^{\mathrm{exp}} - N^{\mathrm{exp}} n_i^{\mathrm{sim}})^2}{n_i^{\mathrm{sim}} + m_i^{\mathrm{exp}}}, \tag{3.13}$$

with N^{sim} and N^{exp} being the total number of entries in the simulated and in the experimental distance spectrum. n_i^{sim} and n_i^{exp} are the entries of the spectra in the i^{th} bin. N_B is the total number of bins. Note that both histograms are required to have the same binning. It can be shown that the quantity in eq. (3.13) corresponds to the well-known χ^2-value [39]. Thus, the reduced χ^2/Ndf defines the goodness of fit obtained by fitting the simulated to the experimental spectrum. The number of degrees of freedom Ndf is equivalent to N_B - 1. More details on Pearson's χ^2-test can be found in app. A.
The fit is implemented as a minimization algorithm of the figure of merit $\chi^2(\sigma)$ for σ ranging from σ_{min} to σ_{max}. For each $\sigma \in [\sigma_{\mathrm{min}}, \sigma_{\mathrm{max}}]$ a distance spectrum with sufficient statistics is simulated. These distance spectra are subsequently compared to the experimental distance spectrum using eq. (3.13). Hence, for each position smearing σ a corresponding χ^2 is calculated. The minimum of the obtained χ^2-distribution defines the position resolution σ. Note

[12] E.g the median of the set $\{1, 1, 2, 2, 1, 2, 18\}$ is 2 whereas the mean value is 3.9. Therefore, the mean is much more influenced by the outlier 18 that the median.

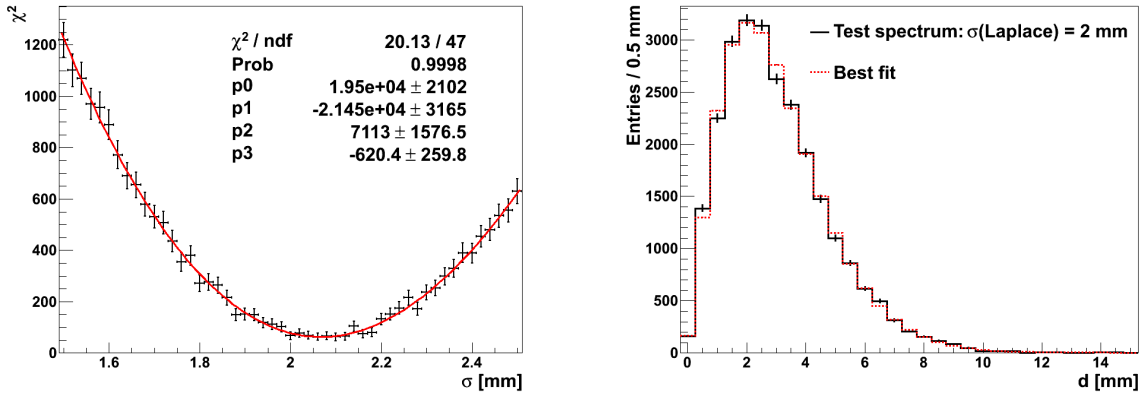

a) b)

Fig. 3.20: Test of the fit algorithm: Attempt to recover the simulated resolution of 2 mm according to a Laplace distribution. **a)** Obtained minimization function. Additionally the polynomial fit of order three is drawn which is needed to determine the minimum of the obtained χ^2-distribution. Its minimum at $\sigma_{\text{fit result}} = 1.99\,\text{mm}$ corresponds to the position resolution. **b)** Comparison of the distance spectrum corresponding to the best fit value and the test distribution with $\sigma = 2\,\text{mm}$. Both distance spectra match quite well ($\chi^2/Ndf = 0.97$).

that the simulated distance spectrum is created using Monte Carlo techniques, i.e. it is prone to statistical fluctuations. Thus, the calculated χ^2-value also suffers from statistical fluctuations. Therefore, the minimum cannot be found by looking at the smallest χ^2-value. As a result, no intelligent search algorithms such as the simplex method [40] can be used. Instead, the fit must be implemented as a slower grid search algorithm. First, the fit is performed on a coarse grid with $\sigma_{\text{min}} = 0$, $\sigma_{\text{max}} = 10$ mm and a step size of $\Delta\sigma = 0.1$ mm. Subsequently a fine grid, centered around the best fit result σ_{coarse} of the coarse grid, is used: $\sigma \in [\sigma_{\text{coarse}} - 0.5\,\text{mm}, \sigma_{\text{coarse}} + 0.5\,\text{mm}]$ with 0.02 mm wide steps. The algorithm calculates for each grid a χ^2-distribution as a function of the grid points σ. To take the statistical fluctuations of the Monte Carlo method into account, each χ^2-value is assigned an error. It is calculated with the Gaussian error propagation which is applied on eq. (3.13) (c.f. eq. (A.7) in app. A). Experience shows that the obtained minimization function can be described well by a polynomial of order three in the vicinity of the minimum. Hence, the polynomial is fitted to the $\chi^2(\sigma)$-values. The minimum of the best fitting polynomial corresponds to the best matching simulated distance spectra and thus defines the position resolution of the measurement.

Validation of the fit strategy

To validate the algorithm, it is used to determine the resolution of a spectrum with known position resolution. Thus, a test spectrum is simulated with Geant4 featuring a position resolution of $\sigma(\text{Laplace}) = 2\,\text{mm}$ according to a Laplace distribution. This test spectrum is treated as the experimental spectrum in the fit. The fit is performed assuming a position smearing according to a Laplace distribution. Fig. 3.20 a) shows the obtained $\chi^2(\sigma)$-values of the fine grid along with the corresponding polynomial fit. As there is a clear minimum the fit converged. The resulting resolution is about $\sigma_{\text{fit result}} = 1.99\,\text{mm}$. For a crosscheck fig. 3.20 b) displays a simulated distance spectra with the determined position resolution $\sigma_{\text{fit result}} = 1.99\,\text{mm}$ and the test spectrum with $\sigma(\text{Laplace}) = 2\,\text{mm}$. As these spectra match together very well the fitting procedures works.

In order to gain more statistics this test was repeated 300 times. The mean position resolution of all 300 fits is $\sigma = (2.01 \pm 0.01)\,\text{mm}$ which is consistent with the initial value of the test

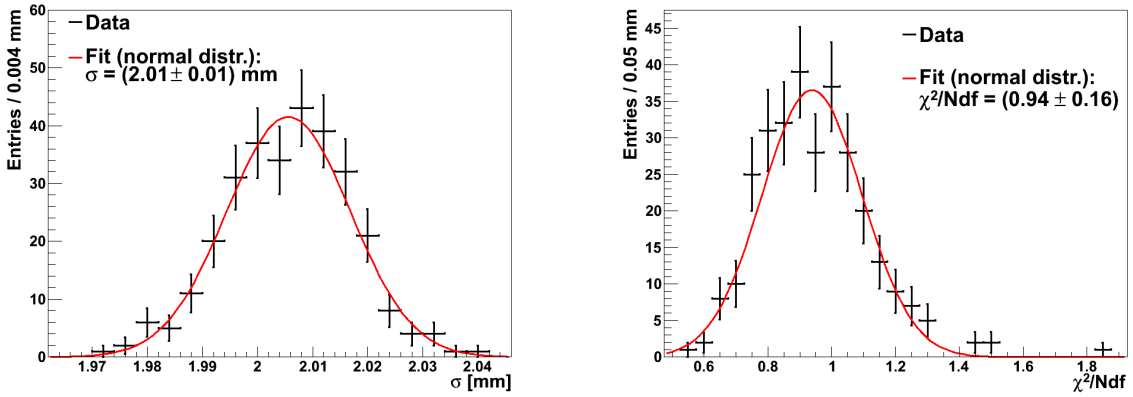

a) b)

Fig. 3.21: **a)** The distribution of the obtained position resolution of 300 fits. **b)** The corresponding χ^2/Ndf values of the fit.

distance spectrum. The error of the fit strategy is given by the standard deviation of the fit with a normal distribution in fig. 3.21 a). This excellent accuracy shows the potential of the method for the determination of the position resolution. It is also consistent with the excellent χ^2/Ndf-values resulting from the Pearson's χ^2-test between the test distance spectrum and the best fitting distance spectrum (c.f. fig. 3.21 b)).

Gaussian or Laplace position smearing?
As the Pearson χ^2-test takes all bins into account the whole shape of the simulated and the measured distance spectra are compared. Thus, the fit strategy can be used to determine whether the real distribution of the interaction points around their true coordinates is more Gaussian-shaped or a Laplace-shaped. Fig. 3.22 shows the test spectrum with $\sigma(\text{Laplace}) = 2\,\text{mm}$ again. Additionally, the best fitting distance spectrum according to a Laplace distribution as well as the best fitting distance spectrum assuming a Gaussian position smearing are visualized. Comparing the spectra, it is clear that the fit with the Laplace smearing matches much better than the Gaussian fit result. The spectrum resulting with the Gaussian smearing decays too fast. This is caused by the fact that the Gaussian distribution, contrary to the Laplace distribution, does not feature the dominant tail far away from the mean value (c.f. fig. 3.17). Furthermore, the broader peak of the Gaussian distribution leads to a maximum in the distance spectrum which is located at higher distances d compared to the maximum resulting from a Laplace smearing. The better consistency of the best fitting distance spectrum resulting from a Laplace smearing is reflected in the goodness of fit χ^2/Ndf (c.f. fig. 3.22). Hence, in the experiment with unknown distribution, the fit is performed twice, i.e. assuming a Gaussian and a Laplace distribution for the smearing of the simulated barycenters. Finally, the obtained χ^2/Ndf-value indicates which distribution is more likely.

Influence of the source position
Apart from that, the fit is suitable to study the influence of the source positioning. For this analysis the same test data with a 2 mm Laplace position smearing is chosen but instead of the correct source position a 1 mm shifted source is used. This results in an additional error of 0.1 mm in the position resolution.

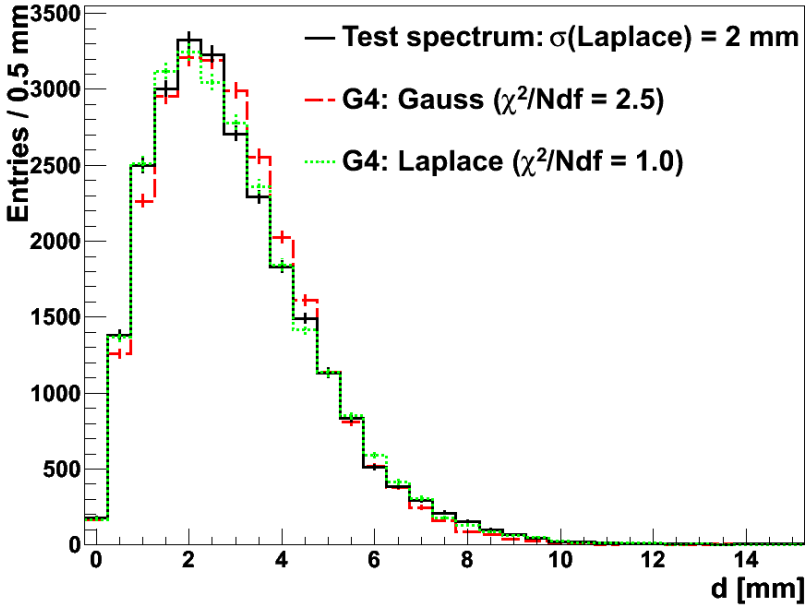

Fig. 3.22: Test distance spectrum with a defined position smearing of σ(Laplace) = 2 mm. Additionally the best fit result assuming a Gaussian and a Laplace position smearing distribution are visualized. As expected the Laplace smearing matches much better than the Gaussian smearing, as the shape of the distance spectrum depends on the distribution of the smeared barycenters around their true coordinates.

Influence of the grid

Additionally, the influence of the cubic grid of the signal basis JASS (1 mm spacing) and ADL (2 mm spacing) has to be studied as the PSA reconstructs only interaction points on the grid instead of interpolating between the grid points. Hence, analog to the validation of the fit strategy a test distance spectrum with known position resolution σ(Laplace) is simulated with Geant4. Additionally, the same distance spectrum is calculated but with the smeared interaction points being subsequently positioned on a 1 mm and 2 mm cubic grid, respectively. Finally, the position resolution of both test spectra is determined separately by fitting them[13]. The difference between the two fit results σ(with grid) and σ(without grid) corresponds solely to the influence of the grid. Fig. 3.23 shows the result of this analysis for various position resolutions σ(Laplace) following a Laplace distribution. As the difference σ(with grid) - σ(without grid) is always positive, the grid deteriorates the position resolution. As expected the influence of the grid increases with improving position resolution. Nevertheless, the influence is one order of magnitude below the current achieved position resolutions of the PSA (c.f. chaps. 4 and 5). Therefore, the grid can be neglected in the following analysis. Moreover, even though the 1 mm grid of the JASS basis has a smaller influence on the position resolution compared to the ADL basis, the JASS basis does currently not result in a better position resolution as the effect is still quite small.

[13] Only the test spectrum features the grid but not the simulated spectrum with is fitted to the test spectrum.

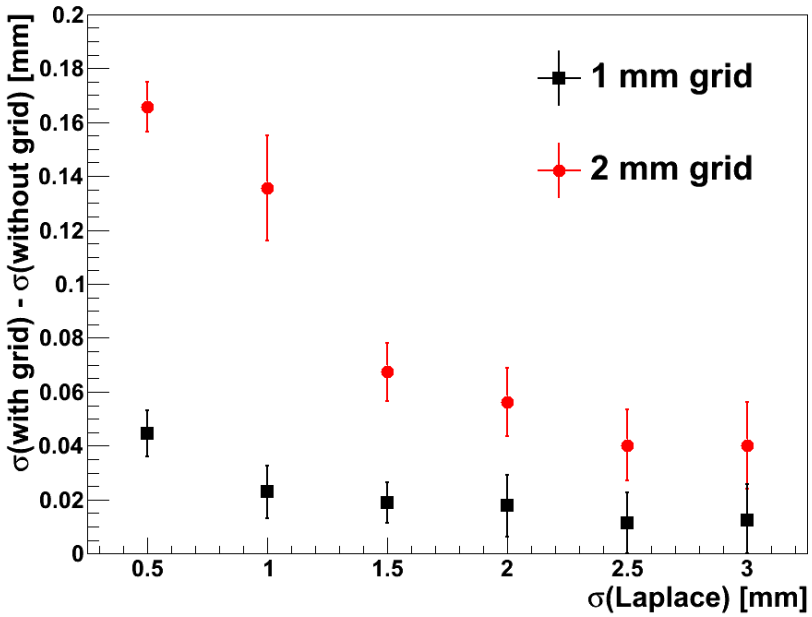

Fig. 3.23: σ(with grid) and σ(without grid) are the obtained position resolutions of simulated test distance spectra with a position resolution of σ(Laplace) with and without considering a 1 mm or a 2 mm cubic grid. Their difference shows that both grids deteriorate the position resolution to a small extend. However, the effect is one order of magnitude smaller than the current experimentally obtained position resolutions. Therefore, both grids can be neglected in the following analysis.

Chapter 4

Test Experiment with a Centered Source

In chap. 3 the analysis strategies of the calibration experiment were presented and exercised with simulation data. This chapter validates them with experimental data from a first test measurement. The setup was already detailed in sec. 2.2: A ^{22}Na source was positioned in the center of the three installed asymmetric triple clusters of the AGATA Demonstrator (c.f. fig. 2.3). Due to the required coincidence measurement of the annihilation γ-rays, only the position resolution of the A001 and A003 crystal can be studied. The experimental data is evaluated with both, the one hit-segment analysis (c.f. sec. 4.1) and the two hit-segment analysis (c.f. sec. 4.2). Additionally, a combined analysis is performed which is detailed in sec. 4.3.

4.1 One Hit-Segment Analysis

First, the results of the one hit-segment analysis are described. Sec. 4.1.1 presents the properties of the events passing the selection cuts which were discussed in sec. 3.3.1. Subsequently, the position resolution is determined using the first estimate (c.f. sec. 3.4.4) and by fitting the simulated to the experimental distance spectrum (c.f. sec. 3.4.5). Due to the symmetric setup and the assumption that both crystals feature the same resolution, both methods can only determine the mean position resolution of the A001 and A003 crystal. Sec. 4.1.4 introduces an approach to extract the position resolutions of individual crystals by combining all available experimental distance spectra. Finally, the distributions of the reconstructed interaction points are discussed in more detail in sec. 4.1.5 in order to find hints for systematic errors of the pulse shape bases.

4.1.1 Properties of the Selected Events

During the first test measurement all raw pulse shapes were written to file. This allows a reprocessing of the data using e.g. different pulse shape bases. Thus, the JASS and the ADL signal basis can be compared directly without introducing further systematic errors due to varying experimental conditions.
In the one hit-segment analysis each crystal is required to have a coincident energy deposition of $E = 511\,\mathrm{keV}$ in a single segment. The reconstructed interaction points of the A001 and the A003 crystal which pass these selection cuts are shown in fig. 4.1 for the JASS and the ADL signal basis. Analogous to fig. 3.13, some of the corresponding reconstructed barycenters are connected with a straight line. As expected from the angular correlation of the annihilation γ-rays, the lines are concentrated near the source which is located in the middle of the two

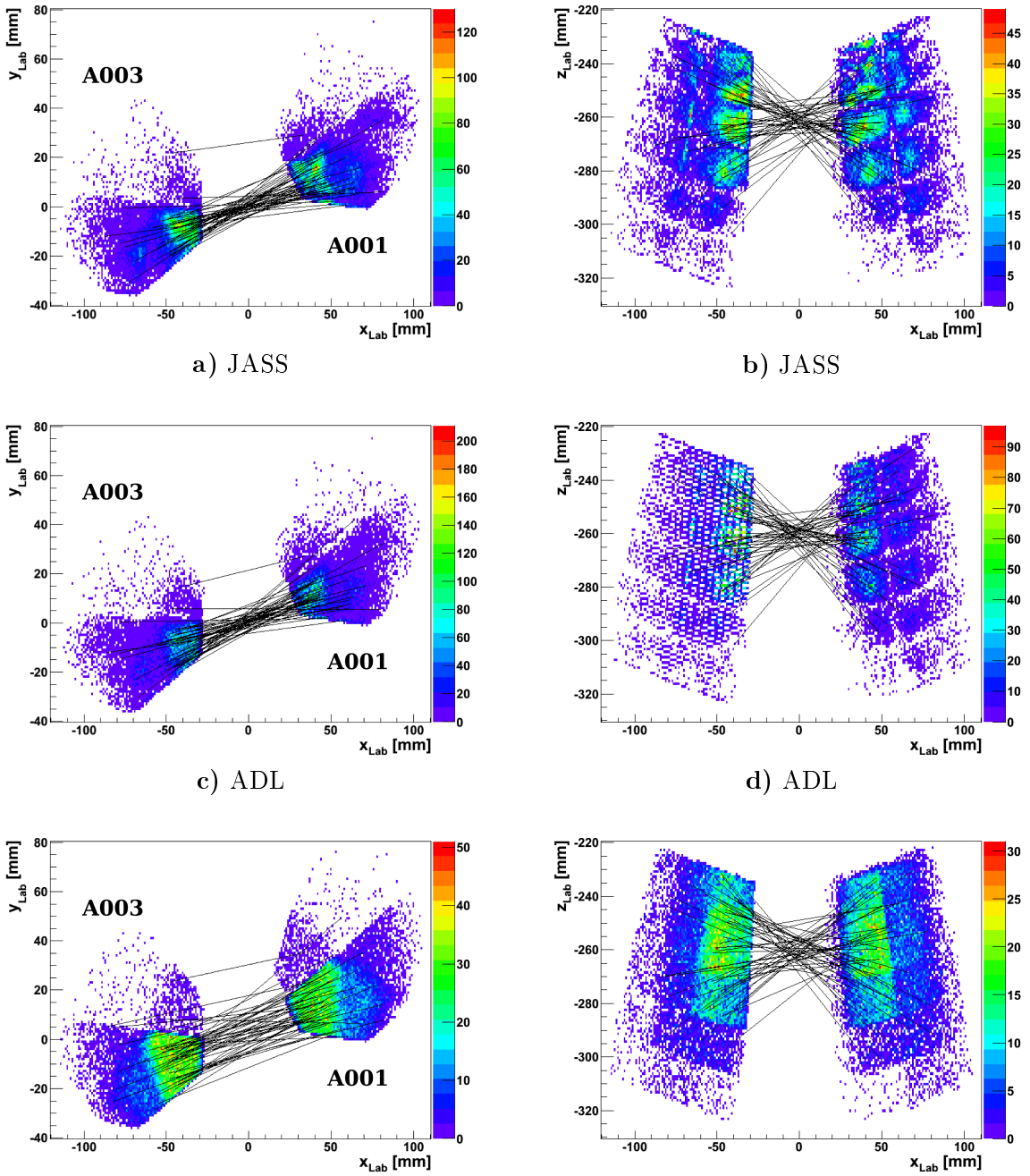

a) JASS **b)** JASS

c) ADL **d)** ADL

e) Random events **h)** Random events

Fig. 4.1: Spatial distribution of the reconstructed interaction points after the event selection of the one hit-segment analysis. The data were taken in the geometry shown in fig. 4.2. The first two rows show the results of the JASS and the ADL basis while the last row shows the distribution in the case the PSA fails completely. The left column represents are front view of the crystals while the right column a side view. Note that the reconstructed interaction points are positioned on a 1 mm cubic grid for the JASS basis and on a 2 mm cubic grid for the ADL basis. The 2 mm grid of ADL is slightly visible in panel **d)** for the A003 crystal.

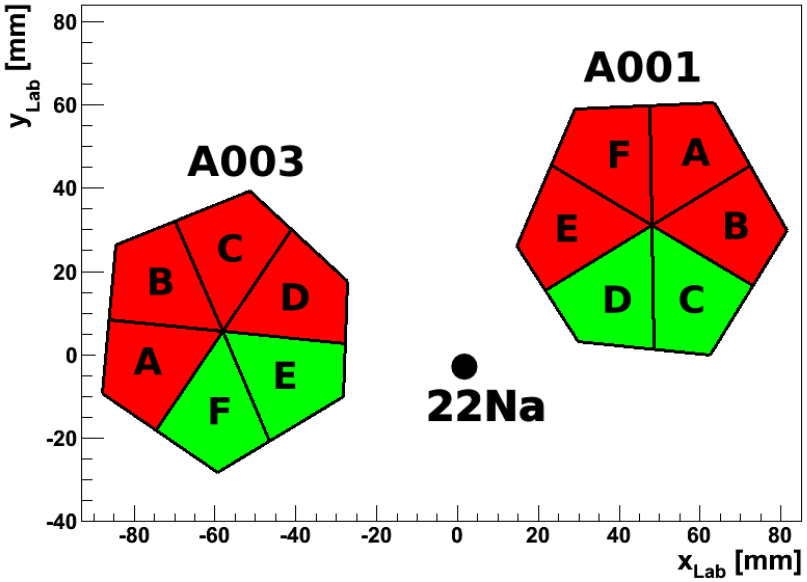

Fig. 4.2: The A001 and the A003 crystal in the laboratory frame. Additionally, their segments are shown. The geometrically allowed segments are visualized in light green whereas the forbidden segments are marked in red. Events in the red segments are discarded as they cannot originate from position annihilations in the ^{22}Na source.

detectors (c.f. fig. 2.3). However, in the experiment the smearing of the lines is significantly broader than in the Geant4 simulation with perfect position resolution (c.f. fig. 3.13). Thus, as described in sec. 3.4.1, the distribution of the lines clearly shows the impact of the position resolution. For comparison the worst scenario is visualized in figs. 4.1 e) and f) showing the smearing of the lines in the case the reconstruction of the interaction points would contain no additional information. Here, the same events are plotted but instead of the reconstructed barycenter a random point in the hit segment is used as interaction point[1]. Hence, the worst possible position resolution is mimicked. Comparing the smearing of the lines obtained for random events to the results of the active PSA, the PSA with both signal bases performs much better than just addressing random points in the hit segment.
Comparing the simulated (c.f. fig. 3.13) to the experimental distribution (c.f. fig. 4.1), there is another striking difference. In contrast to the simulation, the experiment features hits in segments which cannot be accessed due to the geometry of the setup and the required coincident detection of the annihilation γ-rays. The geometrically allowed sectors of the A001 and A003 detectors are illustrated in fig. 4.2 in light green. Nevertheless, in the experiment a non-negligible number of events are passing the selection cuts which are located in geometrically forbidden sectors. Thus, for the following analysis, these background events are discarded[2]. Their possible origin is discussed in sec. 4.1.2.

For the determination of the PSA position resolution the source position has to be known. It can be determined precisely by a fit minimizing the mean distance of the connection lines to the source (c.f. sec. 3.4.2). The fit is performed for the JASS and the ADL basis separately. The resulting source positions of the two signal bases coincide within 1 mm.

[1] The hit segment is never misidentified as it is the only segment showing a net charge signal in this analysis.
[2] Note that sector B in the A001 crystal is geometrically allowed, too. However, it is excluded as the expected count rate is quite low. Thus, a better background suppression is possible.

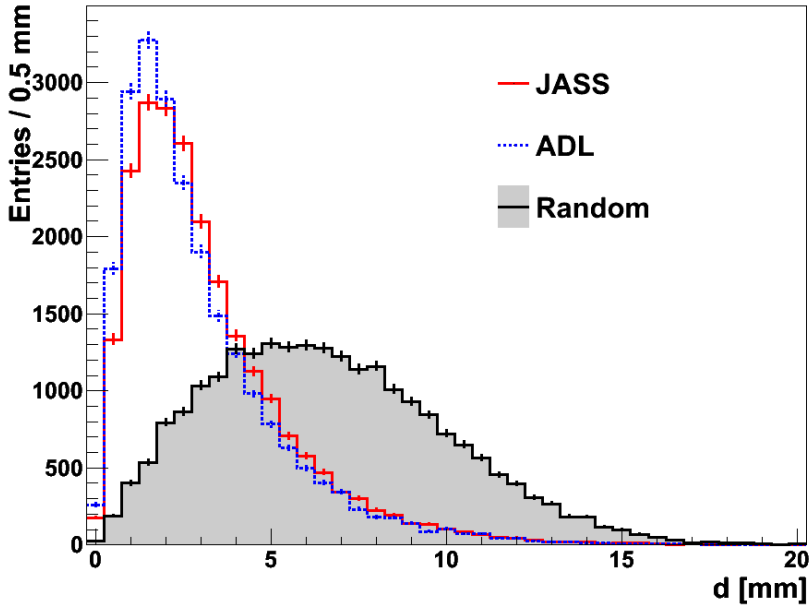

Fig. 4.3: The obtained experimental distance spectra from the symmetric test experiment using the JASS and the ADL signal basis. Additionally, the distance spectrum with the worst possible position resolution is shown.

signal basis	mean [mm]	median [mm]	σ(Gauss) [mm]		σ(Laplace) [mm]	
			mean	median	mean	median
JASS	3.23	2.61	2.9	2.5	2.1	1.9
ADL	2.98	2.33	2.5	2.1	1.8	1.6

Tab. 4.1: Mean position resolutions of the A001 and A003 crystal determined with the first estimation method described in sec. 3.4.4.

4.1.2 Mean Position Resolution

After the event selection and the fit of the source position, the PSA position resolution can be determined using the strategies described in sec. 3.4. As both methods are based on the analysis of the distance spectrum, it is discussed first.

Distance spectra
The distance spectra of events reconstructed with the JASS and the ADL signal basis are shown in fig. 4.3. For comparison the spectrum of the worst scenario with random interaction points is included, too. It differs significantly from the spectra obtained with JASS and ADL illustrating again the benefit of the PSA. The ADL basis perform slightly better than the JASS basis as the ADL distance spectrum is shifted towards smaller distances.

First estimate of the position resolution
As described in sec. 3.4.4, the position resolution of the reconstructed interaction points can be estimated using the mean and the median of the obtained distance spectrum. The position resolution is extracted from figs. 3.19 e) and f) by evaluating the cubic splines for the experimental mean and median. The results are summarized in tab. 4.1 for both signal bases. Comparing the position resolutions, the ADL basis has a slightly better performance than the JASS signal basis. This is consistent with the observation of fig. 4.3. To check the obtained

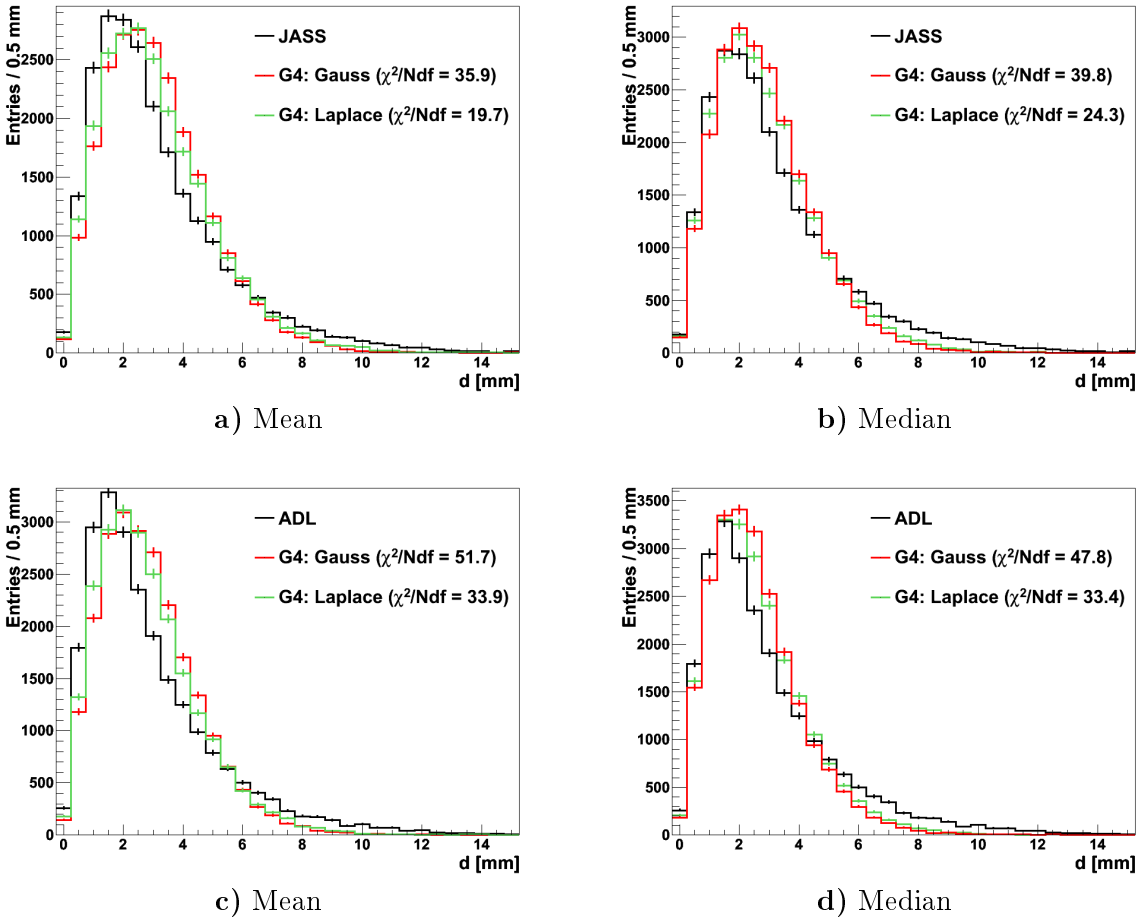

a) Mean **b)** Median

c) Mean **d)** Median

Fig. 4.4: Comparison of the measured and the simulated distance spectra obtained with the first estimate. The resolution used as input parameter for the simulations are taken from the results of the first estimate analysis (c.f. tab. 4.1).

position resolutions, the measured distance spectra are compared to simulated distance spectra (c.f. fig. 4.4). The latter are calculated using the resolutions of tab. 4.1 as input parameters. It is clearly visible that the shapes of all experimental distance spectra do not coincide with the corresponding shapes of the simulated distributions within errors. This is also indicated by the corresponding χ^2/Ndf-values[3] which are significantly larger than one. Hence, neither the Gaussian nor the Laplace distribution describes the distribution of the reconstructed barycenters around their true coordinates very well. Nevertheless, the Laplace distribution seems to be more likely in all cases.
Furthermore, there is a big discrepancy between the position resolutions which are determined using the mean and the median. It can be explained by the fact that the shapes of the experimental and the simulated distance spectra differ while the estimation of the position resolution assumes an identical shape. As this is not the case, it is likely that the mean and the median lead to different results. Comparing the agreement of the rising slope and the peak between the measured and the simulated spectra, the median (right column in fig. 4.4) seems to outperform the mean (left column in fig. 4.4). This can be caused by outliers e.g. background events in the experiment which are naturally not included in the Geant4 simulation. As these outliers can deteriorate the mean value of the measured distance spectrum the determined position resolution using the mean is worse compared to the median position resolution. Contrary, the

[3] They are calculated with Pearson's χ^2-test.

smearing distribution (JASS/ADL)	σ [mm]	χ^2/Ndf
Gauss	2.7 / 2.2	14.7 / 19.7
Laplace	2.1 / 1.8	9.5 / 13.1
86(87)% Gauss + 14(13)% randomly assigned points in the hit segment	2.0 / 1.6	1.3 / 2.0
88(88)% Laplace + 12(12)% randomly assigned points in the hit segment	1.5 / 1.2	1.4 / 1.5

Tab. 4.2: Mean position resolutions of the A001 and the A003 crystal determined by fitting the simulated to the experimental distance spectrum. The first two rows show the results of the one-parameter fit assuming a Gaussian and Laplace distribution. The last two rows display the results from two-parameter fits with modified Gaussian and Laplace distributions. Here, it is assumed that a certain amount of the simulated barycenters are smeared according to a Gaussian / Laplace distribution while for the rest of the events the true barycenter coordinates are ignored and instead a randomly chosen point in the hit segment is used.

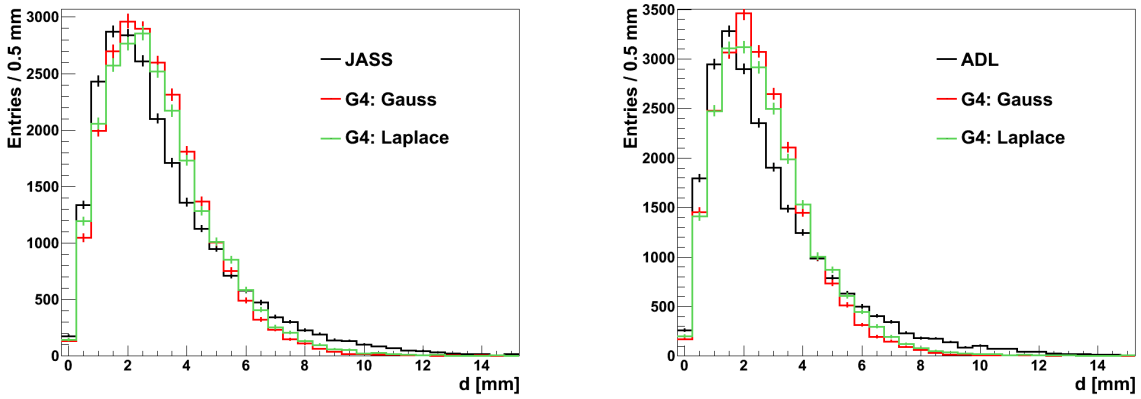

a) σ(Gauss) = 2.7 mm, σ(Laplace) = 2.1 mm

b) σ(Gauss) = 2.2 mm, σ(Laplace) = 1.8 mm

Fig. 4.5: Resulting simulated distance spectra of the one-parameter fit compared to the measured spectra of the JASS and the ADL basis. The shapes of the fitted distance spectra do not match the experimental spectra.

distance spectra based on the mean value describe the tail of the experimental spectra better. As a result, it can be concluded that the method using the mean and the median gives a first estimate of the position resolution. For a more exact determination, more sophisticated methods have to be used.

Determination of the position resolution by fitting the distance spectrum

The results of the first estimation of the position resolution already indicate that the shapes of the experimental distance spectra do not match to the simulated spectra. Thus, it is of great importance to include the whole shape of the spectra in a more quantitative way. This is possible by fitting the simulated distance spectrum to the experimental spectrum (c.f. sec. 3.4.5). The first two rows of tab. 4.2 summarize the obtained position resolutions of the JASS and the ADL basis assuming a Gaussian and a Laplace smearing. The corresponding distance spectra are shown in fig. 4.5. As the fitted position resolutions are in the corresponding σ-intervals given by the mean and the median, the results of the first estimate and the fits are consistent. Nevertheless, the χ^2/Ndf-values of the fits are significantly smaller than the obtained reduced χ^2-values of the first estimates. Therefore, the fit is a more powerful tool to

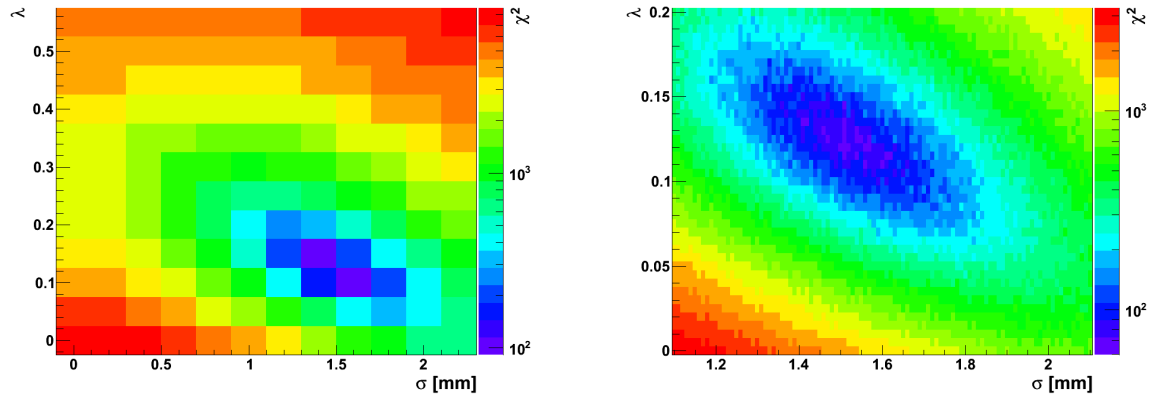

a) b)

Fig. 4.6: Minimization functions of the two-parameter fit for the JASS basis assuming the modified Laplace smearing distribution. **a)** Coarse grid. **b)** Fine grid. The minimum is located at $\sigma = 1.5\,\text{mm}$ and $\lambda = 0.12$.

determine the position resolution. This is expected as fitting a whole distribution is always more precise than just comparing a single quantity of the distribution such as the mean or the median. Furthermore, the χ^2/Ndf-values indicate that the Laplace distribution describes the experimental data better than the Gaussian distribution.

Modified smearing distribution for the simulated barycenters

Although the agreement between the measured and the simulated distance spectra is improved with the fit, the resulting χ^2/Ndf-values are still bigger than 10 (c.f. tab. 4.2). As a consequence, the distribution of the reconstructed barycenters around their true coordinates cannot be well described with a Laplace or a Gaussian probability density function. Hence, a different smearing distribution is chosen: The barycenters in the Geant4 simulation are divided into two groups. The barycenters of the first group are smeared according to a Gaussian or a Laplace distribution as described in sec. 3.4.3. Contrary, the simulated barycenters of the second group are replaced by a random point in the hit segment, i.e. their actual coordinates are ignored. This is equivalent to smear the Geant4 barycenters according to a flat probability density function which is constrained to the hit segment. The hit segment of these random events stays the same as a misidentification of the hit segment is not possible due to its net charge signal. Hence, the smearing distribution is defined by two parameters. The standard deviation σ of the Gaussian or the Laplace distribution and the fraction λ of the random events.

Two-parameter fit with the modified smearing distribution

As the modified smearing distribution is described by two parameters, the determination of the position resolution becomes more challenging. Analogous to sec. 3.4.5, a two-parameter fit is performed which is based on a grid search using a coarse and a fine grid: The two parameters σ and λ are varied until the measured and the simulated distance spectrum coincide. To speed up the fit, reasonable upper limits have to be set for both parameters. This is done by a set of dedicated fast algorithms. Subsequently, the distance spectra using the modified position smearing are simulated for all grid points (σ, λ) on the coarse grid. Each simulated spectrum can then be compared with the measured distance spectrum using Pearson's χ^2-test. An example of a resulting χ^2-distribution on the coarse grid is visualized in fig. 4.6 a). It shows a single minimum in the (σ, λ)-plane. Hence, the fit yields a unique result. The fit procedure is repeated on a finer grid around the minimum of the coarse grid (c.f. fig. 4.6 b)). The position

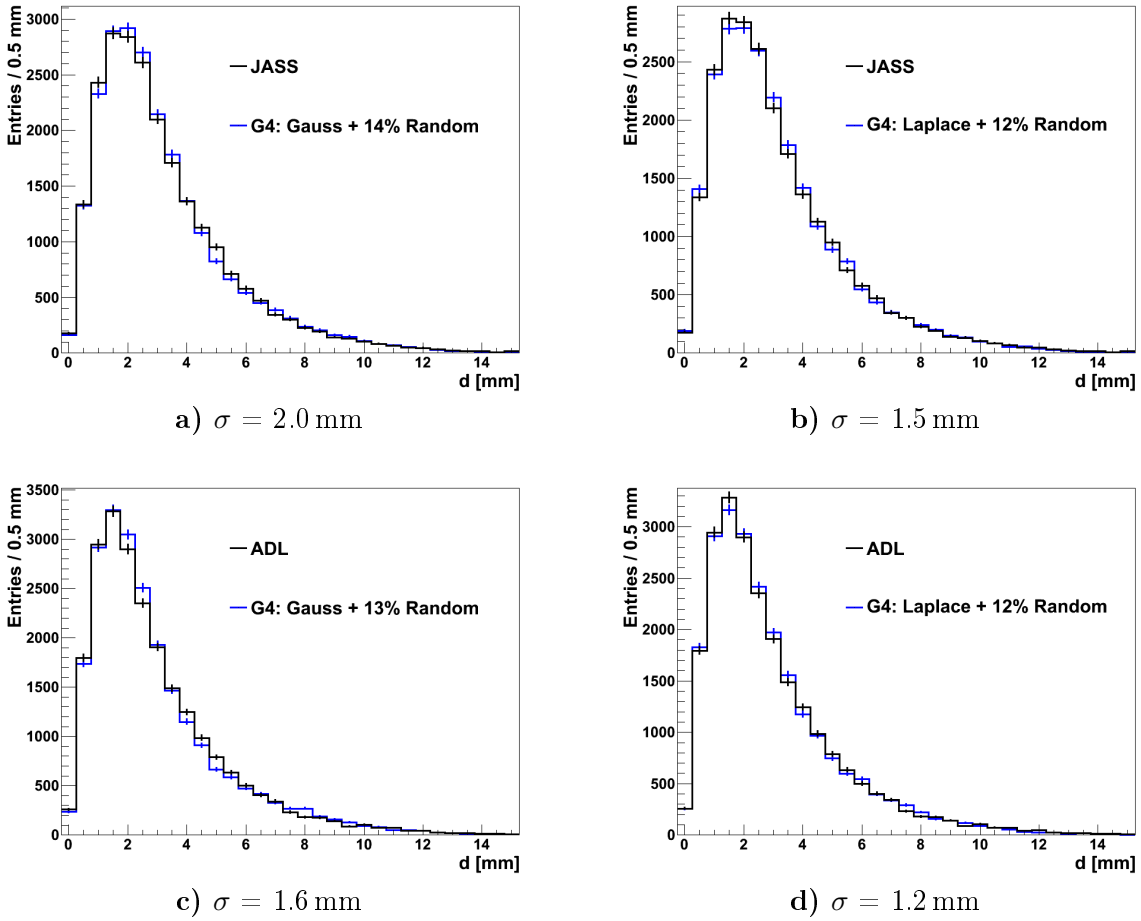

a) $\sigma = 2.0\,\mathrm{mm}$ **b)** $\sigma = 1.5\,\mathrm{mm}$

c) $\sigma = 1.6\,\mathrm{mm}$ **d)** $\sigma = 1.2\,\mathrm{mm}$

Fig. 4.7: Comparison of the best fitting simulated distance spectra of the two-parameter fit with the experimental spectra using the JASS and the ADL basis. The agreement between the experiment and the fit is always good.

of the minimum on the fine grid allows a precise determination of the final fit result (σ, λ). The results of the two-parameter fits are shown in the last two rows of tab. 4.2. Compared to the one dimensional fits, the agreement between the experimental and the simulated distance spectra is improved ($\chi^2/Ndf \leq 2.0$). The best fitting simulated distance spectra of the two-parameter fits are shown in fig. 4.7. The good agreement between the fits and the experiment indicates that the modeled smearing distribution based on the parameters σ and λ describes the experimental data of both signal bases well. Comparing the fraction λ of the random events assuming a Gaussian and a Laplace distribution, λ is slightly higher for the Gaussian distribution. This can be explained with the more pronounced tail of the Laplace distribution (c.f. fig. 3.17). Note that the obtained position resolutions are already with the one hit-segment analysis within the specifications of AGATA (FWHM $< 5\,\mathrm{mm}$ [6]) if the random events are neglected.
An example of the smearing distribution is visualized in fig. 4.8 assuming a Gaussian distribution with $\sigma(\mathrm{Gauss}) = 2\,\mathrm{mm}$ and $\lambda = 0.12$. Comparing the different components in fig. 4.8 the Gaussian distribution clearly dominates. Fig. 4.9 shows the distance spectrum, split into its components which correspond to the different parts of the modified smearing distribution. It illustrates that the random events have a strong impact of the shape of the distance spectrum. Hence, they cannot be neglected in the analysis of the PSA position resolution[4].

[4] In principle, also a three parameter fit can be performed, i.e. with two Gaussian / Laplace distributions

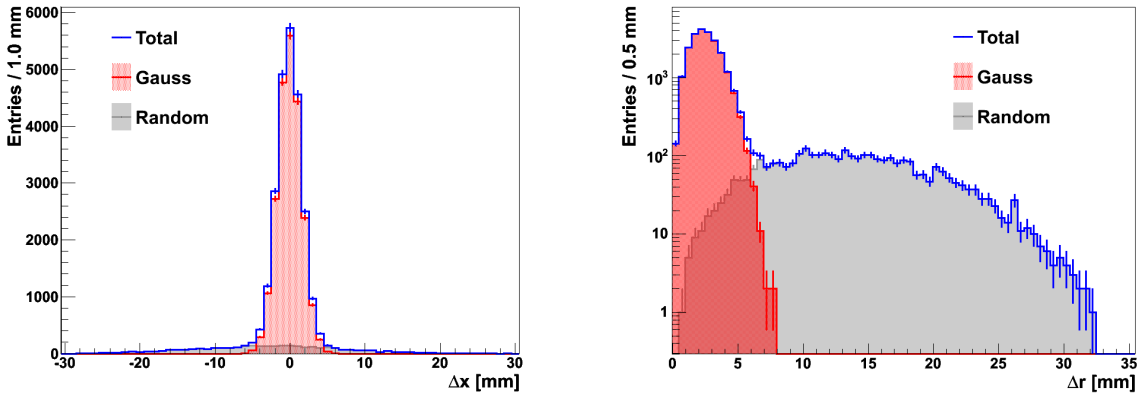

a) b)

Fig. 4.8: Components of the modified smearing distribution in the A001 crystal. 88% of the simulated barycenters are smeared according to a Gaussian distribution with $\sigma(\text{Gauss}) = 2\,\text{mm}$ while for the rest of the events the true barycenter coordinates are ignored and instead a random point in the hit segment is used. **a)** Distance between the x-coordinate of the smeared barycenter and the true barycenter position. **b)** Absolute distance Δr of the smeared and the true barycenter.

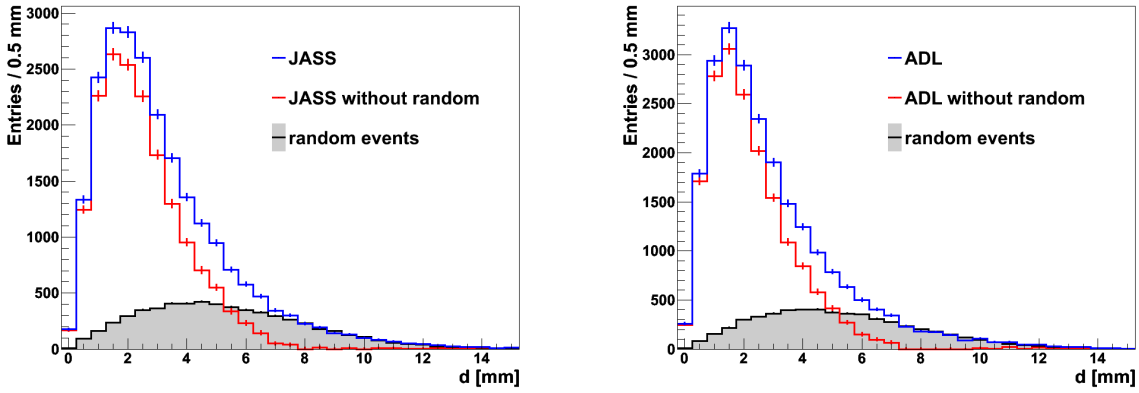

a) b)

Fig. 4.9: Components of the distance spectra for 12% random events. As the random distribution peaks at higher distances, it leads to a more pronounced tail in the total distance spectrum.

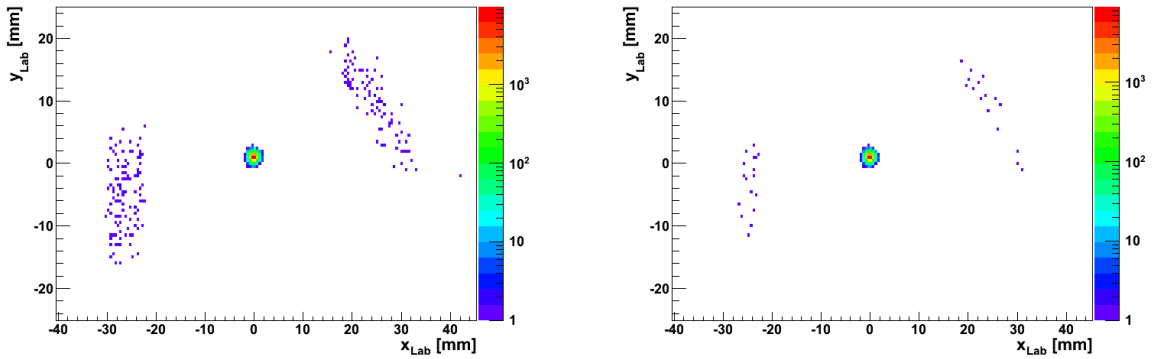

Fig. 4.10: Distributions of the simulated positron annihilation vertices. Most of the positions annihilate in the source, but some annihilate in the cryostat of the A001 and the A003 crystal. **a)** All vertices of the events selected in the one hit-segment analysis. **b)** The same events but additionally the segment look-up table has to be passed. The segment look-up table throws away 83% of the events with escaping positrons.

Interpretation of the random events

The amount of random events is nearly independent of the pulse shape basis. Thus, it is likely that the random events have the same origin for both signal bases. In principle, there are two possible interpretations. The first assumes that the PSA completely fails, as it is possible that the crystals feature regions which are described badly by both signal bases. This can be caused e.g. by a deviation of the space charge distribution from the expectation. Nevertheless, as discussed in the following and in chap. 5 the random events have predominantly a different origin which is related to the geometry of the ^{22}Na source. If the source containment is too thin, a certain fraction of the positrons has enough energy to escape from the source and annihilate somewhere else. This is visualized with a Geant4 simulation[5] in fig. 4.10 a). It shows the simulated distribution of the positron annihilation vertices of events passing the selection cuts of the one-hit segment analysis. Most of the annihilation vertices are concentrated in the source, but a non-negligible amount of positrons annihilates in the cryostat of the A001 or the A003 detector. The impact of the escaping positrons on the distance spectra is schematically displayed in fig. 4.11. As the annihilation vertex and the source position does no longer coincide in the case of escaping positions it is possible to get entries at high values in the distance spectrum even though the PSA works perfect. As a result, these escaping positions mimic a bad position resolution because they produce pseudo-random events. Furthermore, in contrast to the first interpretation, the escaping positrons also explain the events in the geometrically forbidden segments in fig. 4.1. Geometrically forbidden segment combinations can be excluded by using the look-up table from the two hit-segment analysis leading to a suppression of escaping positrons by 83% (c.f. fig. 4.10 b)). The influence of the look-up table is also directly visible in the experiment. Fig. 4.12 shows the obtained distance spectra with and without the look-up table for the JASS and the ADL basis. The look-up table rejects about 14% of the events in the distance spectra. This indicates that the experiment features

featuring different standard deviations σ. The third fit parameter is needed to define the ratio between the two Gaussian / Laplace distributions. Nevertheless, the resulting smearing distribution does not differ much from the described two-parameter distribution. Thus, the three parameter fit is not considered in this thesis as it is even more complicated and more demanding in terms of computation time.

[5] In the Geant4 simulation it is assumed that the ^{22}Na material has a cylindrical plastic coverage with 5 mm in diameter and a total height of 1 mm.

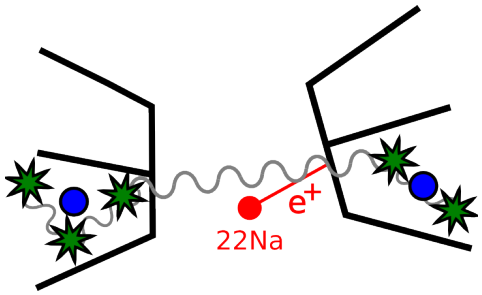

Fig. 4.11: The positrons of the ^{22}Na decay can escape the source if it is too thin. Subsequently, they can annihilate in the cryostat of one AGATA detector. Thus, the first interaction points and the source are not positioned on a straight line anymore. This leads to a background in the distance spectra at high distances as these events cannot be discriminated from annihilations in the source. As a result, escaping positrons mimic a worse position resolution.

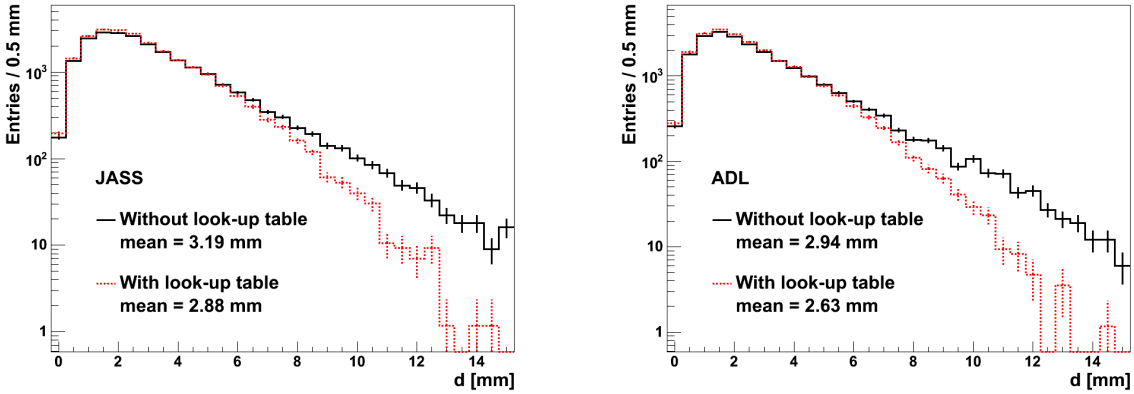

Fig. 4.12: Distance spectra of the JASS and the ADL basis with and without considering the look-up table introduced sec. 3.3.2. For a better comparison of the shapes the spectra with the look-up-table are normalized to the spectra without the look-up table.

indeed a significant amount of forbidden segment combinations which can be caused by escaping positions. Furthermore, the mean values of the distance spectra improve by at least 0.3 mm if the look-up table is considered as the rejected events are predominately situated in the tail of the distance spectra.
Combining these statements with the result of the second test measurement (c.f. chap. 5), it can be concluded that the random events are mainly due to escaping positrons. Hence, the random events included in the two-parameter fit describe the background, while the standard deviation of the Gaussian and Laplace smearing describes solely the position resolution.

Worst case: Position resolution of random events
As already stated, the position resolutions in tab. 4.2 fulfill the requirements of AGATA [6] as the standard deviations are better than 2 mm. To further show the benefit of the AGATA PSA, the resolution obtained by randomly assigned interaction positions is computed. For its determination a one-parameter fit (c.f. sec. 3.4.5) is performed with the distance spectrum of the random events (c.f. fig. 4.3). Assuming a Gaussian position smearing the position resolution is $\sigma(\text{Gauss}) = 7.5\,\text{mm}$ ($\chi^2/Ndf = 3.00$), while a Laplace smearing yields $\sigma(\text{Laplace}) = 5.7\,\text{mm}$ ($\chi^2/Ndf = 10.4$). Comparing the χ^2/Ndf-values, the Gaussian smearing seems to be more likely. Both resolutions are at least three times larger than the obtained values for the JASS and

smearing distribution (JASS/ADL)	σ [mm]	χ^2/Ndf
84(84)% Gauss + 16(16)% randomly assigned points in the hit segment	2.6 / 2.3	2.3 / 4.6
88(88)% Laplace + 12(12)% randomly assigned points in the hit segment	2.1 / 1.8	1.1 / 2.1

Tab. 4.3: Mean position resolutions of the first interaction point. Compared to the barycenter (c.f. tab. 4.2) its resolution is about 0.6 mm worse.

the ADL signal basis. This illustrates the impressive performance of the position reconstruction of γ-ray interaction points in AGATA, already at the low energies used here.

4.1.3 Influence of the Barycenter

In sec. 4.1.2 the mean barycenter position resolution of the A001 and A003 crystal was discussed. However, the position resolution of the first interaction point is of greater interest as it is needed for the Doppler correction of γ-ray spectra. Nevertheless, the current PSA algorithm is not capable to reconstruct the first interaction points as it packs all interaction points of a segment to the barycenter. Thus, the location of the first interaction point has to be approximated with the reconstructed barycenter although these two points do not coincide in most of the cases (c.f. fig. 3.8 b)). Hence, this section deals with the systematic error which is caused by this assumption. To determine the position resolution of the first interaction point the simulated distance spectrum is not calculated with the barycenter but with the first interaction points of the annihilation γ-rays. The resulting distance spectrum is fitted to the experimental spectrum using the two-parameter fit (c.f. sec. 4.1.2). The results for the JASS and the ADL basis are stated in tab. 4.3. In comparison of the barycenter results in tab. 4.2, the results of the first interaction points are about 0.6 mm worse which is a measure for the contribution of the barycenter to the resolution.

4.1.4 Estimation of the Position Resolution of Individual Crystals

Due to the symmetric setup of the first test measurement both crystals contribute with the same amount to the smearing of the connection lines in fig. 4.1. Consequently, with a single distance spectrum only the mean position resolution of the A001 and the A003 detector can be determined. As the two crystals of the test measurements are analyzed with two different signal bases, all possible permutations of the crystals and the signal bases can be studied. This leads to a total of four distance spectra which are visualized in fig. 4.13 a). They contain information about the individual crystal resolutions of the two signal bases. Thus, a multi-parameter fit with the four position resolutions as fit parameters is performed. The random events (c.f. fig. 4.9) are subtracted statistically before the fit to keep the number of free parameters minimal.

Fit strategy

In the following the fit strategy is described in more detail. As in the previous sections the fit is based on a grid search algorithm. However, a full grid search in four parameters cannot be performed because the required computation time is too long. Thus, the fit is realized in several steps.

Generally, each distance spectrum (d.s.) is influenced by two different position resolutions σ(crystal, basis) (c.f. fig. 4.13 b)). σ(A001, JASS) e.g. influences one distance spectrum together with σ(A003, JASS) (black spectrum in fig. 4.13 a)) and another together with

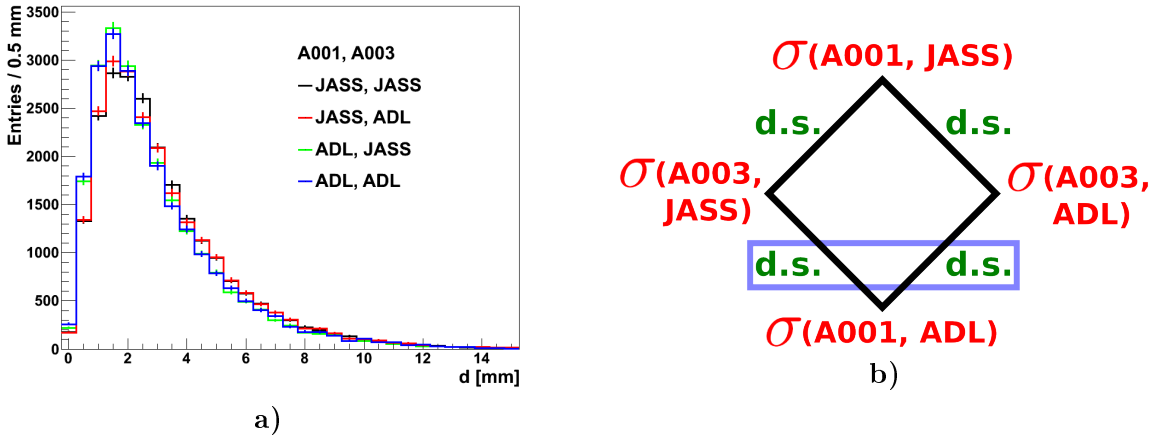

Fig. 4.13: a) The measured distance spectra for all permutations of the JASS and ADL basis. They can be used to determine the position resolution of the individual crystals. **b)** Schematic diagram of the fit strategy of the four-parameter fit. d.s. is short for distance spectrum. For details see sec. 4.1.4.

σ(A003, ADL) (red spectrum in fig. 4.13 a)). However, no distance spectrum is directly influenced by σ(A001, JASS) and σ(A001, ADL) at the same time as both resolutions belong to the same crystal. Thus, for a given σ(A001, JASS), the JASS and ADL position resolutions of the A003 crystal can be determined independently from each other with two separate one-parameter fits. As a result, a triple with these position resolutions is created: {σ(A001, JASS), σ(A003, JASS), σ(A003, ADL)}. The remaining parameter σ(A001, ADL) is determined by a combined one-parameter fit by minimizing the sum of the χ^2-values of the two remaining distance spectra. Thus, a quadruplet is created which contains all four position resolutions. At each fit the χ^2-value can be calculated with Pearson's χ^2-comparison test. The quadruplets and their corresponding χ^2-values are determined for a broad range of σ(A001, JASS)-values. The quadruplet which best matches the experimental data is finally determined by minimizing the global χ^2 given by the sum of the χ^2-values of the four distance spectra.
Assuming a Laplace position smearing, fig. 4.14 a) shows the global χ^2-distribution as a function of σ(A001, JASS). Its minimum at about σ(A001, Jass) $\approx$ 1.4 mm defines the best fitting quadruplet. Figs. 4.14 c) and d) display the minimization function of the black and the red distance spectra for this quadruplet, respectively. They show the χ^2-values of the one-parameter fits with σ(A001, JASS) fixed to 1.4 mm. Their minima correspond to the resolutions of the A003 crystal for both bases. Fig. 4.14 b) visualizes the minimization function for the last unknown resolution σ(A001, ADL) of the quadruplet. As it has to match to the green and the blue distance spectrum, the sum of the χ^2-values of the combined fit to both distance spectra is plotted. All minimization functions show minima indicating that the fit is truly sensitive to the individual position resolutions of the crystals.

Fit results
The obtained position resolutions of the four-parameter fit are summarized in tab. 4.4. In the A003 crystal the JASS and the ADL basis feature the same position resolution. This is also indicated in the distance spectra in fig. 4.13 a) as they do not change much if only the basis of the A003 crystal is exchanged. Contrary, the ADL signal basis outperforms the JASS basis in the A001 detector as σ(ADL, A001) is at least a factor of two better than σ(JASS, A001). The distance spectra in fig. 4.13 a) show the same behavior as there is a clear improvement of the spectrum if the JASS basis in A001 is replaced by the ADL basis. Thus, the statement of

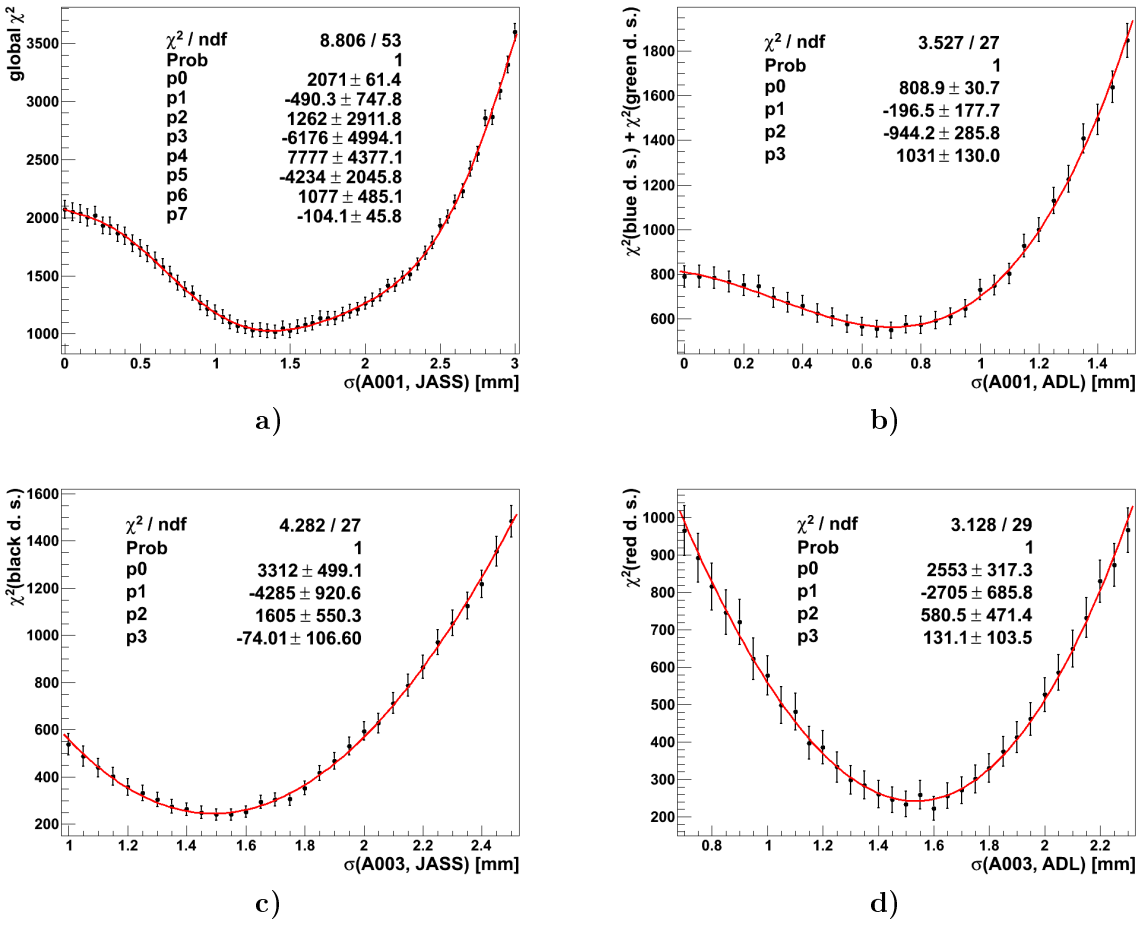

Fig. 4.14: Minimization functions of the four-parameter fit assuming a Laplace smearing distribution. **a)** Global χ^2-values determining the best fitting quadruplet which is defined by σ(A001, JASS). The remaining minimization functions show the χ^2-distributions of this quadruplet. Their minima define the other three position resolutions of the A001 and A003 crystal for the signal basis JASS and ADL. d.s. is short for distance spectrum. The colors used to identify the distance spectrum correspond to the colors used in fig. 4.13 a)

smearing distribution	σ(A001, JASS) [mm]	σ(A003, JASS) [mm]	σ(A001, ADL) [mm]	σ(A003, ADL) [mm]
Gauss	1.8	2.2	0.7	2.1
Laplace	1.4	1.5	0.7	1.5

Tab. 4.4: Obtained position resolutions of the four-parameter fits.

the last section that ADL is generally slightly better than JASS has to be revised. This is only true for the A001 crystal. The results of the four-parameter fit are also consistent with the results of the two-parameter fits as the mean values of tab. 4.4 coincide well with the position resolutions given in tab. 4.2.

4.1.5 Systematic Errors of the Pulse Shape Bases

The obtained position resolutions in secs. 4.1.2 and 4.1.4 always refer to the whole crystal. Nevertheless, for improving the pulse shape basis it is useful to know which regions in the crystal feature worse position resolutions. One method to localize the problematic regions is to look at the two dimensional spatial distributions of the reconstructed interaction points. Figs. 4.15 and 4.16 display all barycenters of the A001 and A003 crystal in the x-y plane of the crystal coordinate system[6] which are passing the event selection of the one hit-segment analysis. Furthermore, the distributions are plotted for each segment row separately. For comparison, the distributions of the simulated barycenters without position smearing are additionally visualized. In general, it can be concluded that the obtained distributions of the ADL basis matched quite good with the Geant4 simulation for both crystals. The JASS basis features regions where no interaction points are reconstructed, e.g. in the tip of the segments in the first row of the A001 crystal. A possible reason can be wrong mobility parameters (c.f. tabs. 1.3 and 1.4).Furthermore, the reconstructed interaction points of the JASS basis tend to cluster in the segment center to a higher extent than expected due to the barycenter. Comparing the distributions of the JASS basis the clustering is stronger in the A001 crystal than in the A003 crystal. The clustering is also present in the ADL basis, however to a smaller extent. Nevertheless, the outstanding performance of the ADL basis of the A001 crystal is not proven by this method. Apart from that, it has to be mentioned that both bases have in the same regions problems, e.g. in row four of the A003 crystal. This can be caused by wrong input parameters of the pulse shape simulations.
The "holes" and the clustering beyond the barycenter influence indicate that the assumption of a Laplace or a Gaussian smearing distribution is not totally true. This leads to an additional systematic error for the obtained position resolutions.

4.2 Two Hit-Segment Analysis

After the position resolution of the barycenter is determined, this section deals with the position resolution of single interaction points. Single interaction positions are selected by the two hit-segment analysis, presented in sec. 3.3.2. Their properties are briefly described in sec. 4.2.1. Based on the distance spectra, the mean position resolution of single γ-ray interactions is determined (c.f. sec. 4.2.2). Finally, the obtained results are discussed in sec. 4.2.3.

4.2.1 Properties of the Selected Events

The two hit-segment analysis considers events which feature a Compton scattering of the annihilation γ-rays from one segment into a neighboring segment in both crystals. The spatial distribution of the interaction points in the Compton segment reconstructed with the JASS and the ADL basis are displayed in fig. 4.17. For both bases the smearing of the connection lines around the source position is significantly broader compared to the one hit-segment analysis (c.f. fig. 4.1). Generally, the larger smearing can be due to two different reasons: First, the position resolution is indeed worse e.g. due to the lower deposited energies (c.f. sec. 3.3.2) or

[6] The x-axis of the crystal coordinate system passes the tip of the segment A. The z-axis corresponds to the symmetry axis of the detector.

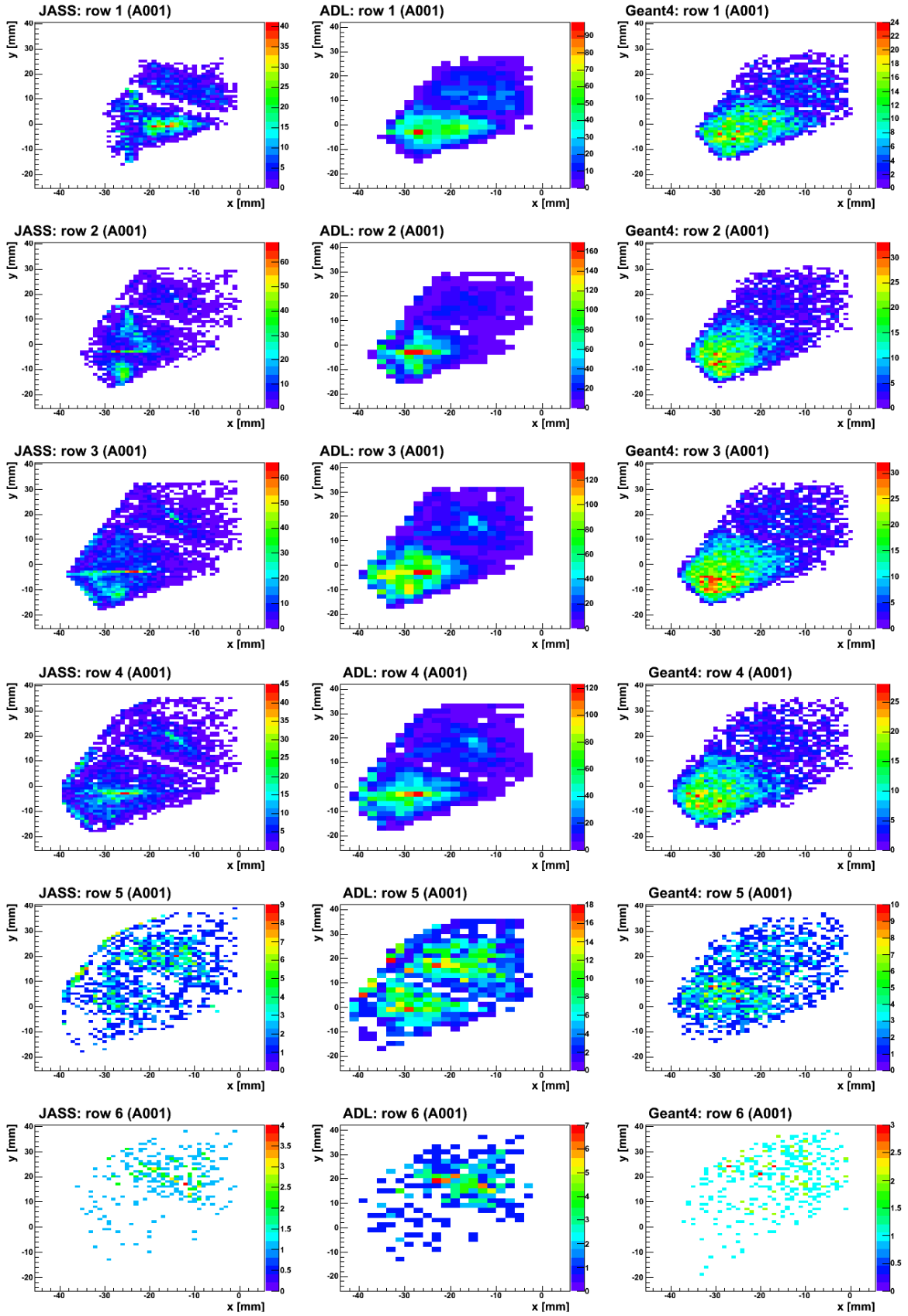

Fig. 4.15: Front view of the spatial distributions of the barycenters in the A001 crystal. Only events which have an energy deposition of 511 keV in one segment are considered. Note that the JASS basis is calculated on a 1 mm grid while the ADL basis uses a 2 mm grid.

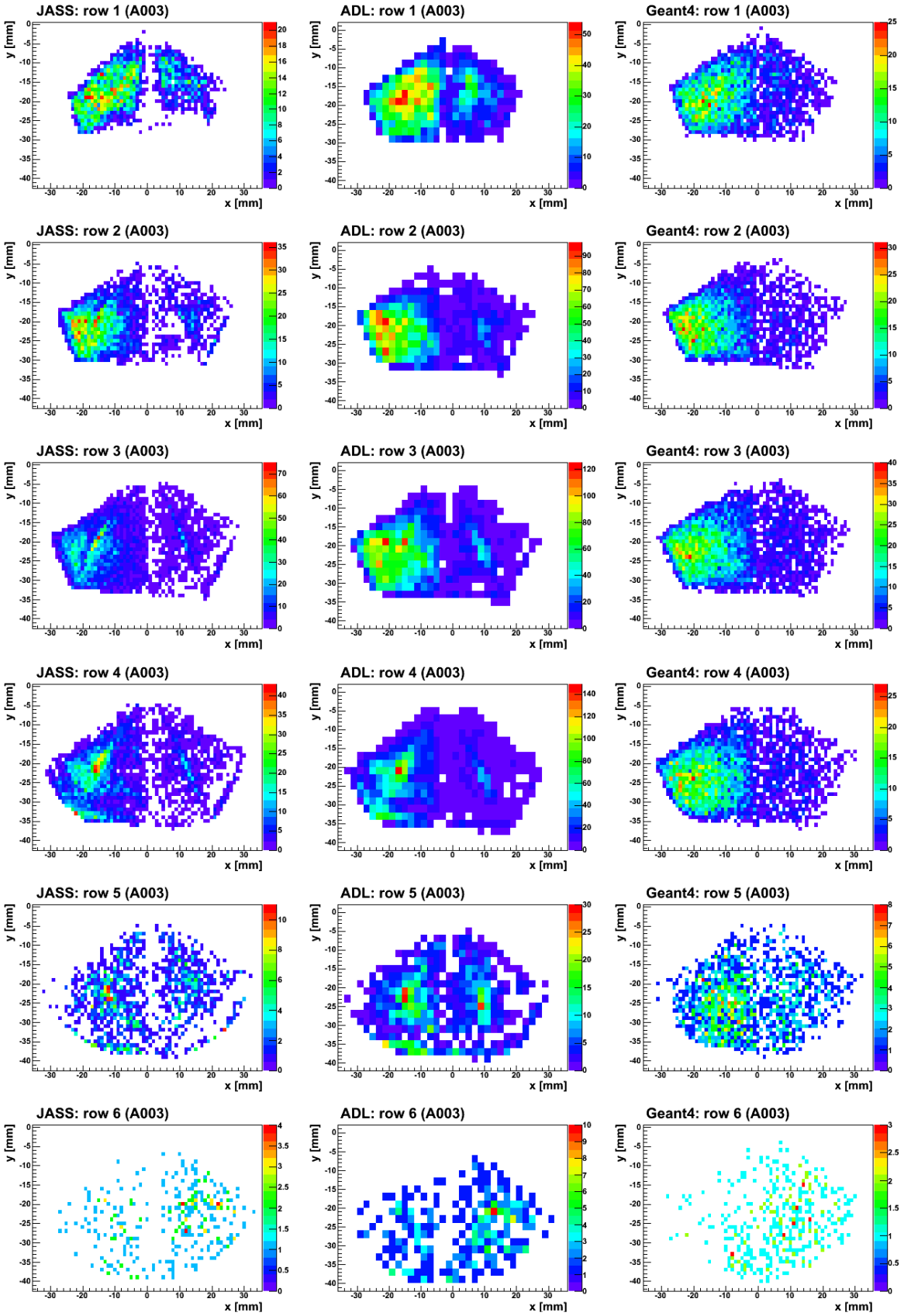

Fig. 4.16: Front view of the spatial distributions of the barycenters in the A003 crystal. Only events which have an energy deposition of 511 keV in one segment are considered. Note that the JASS basis is calculated on a 1 mm grid while the ADL basis uses a 2 mm grid.

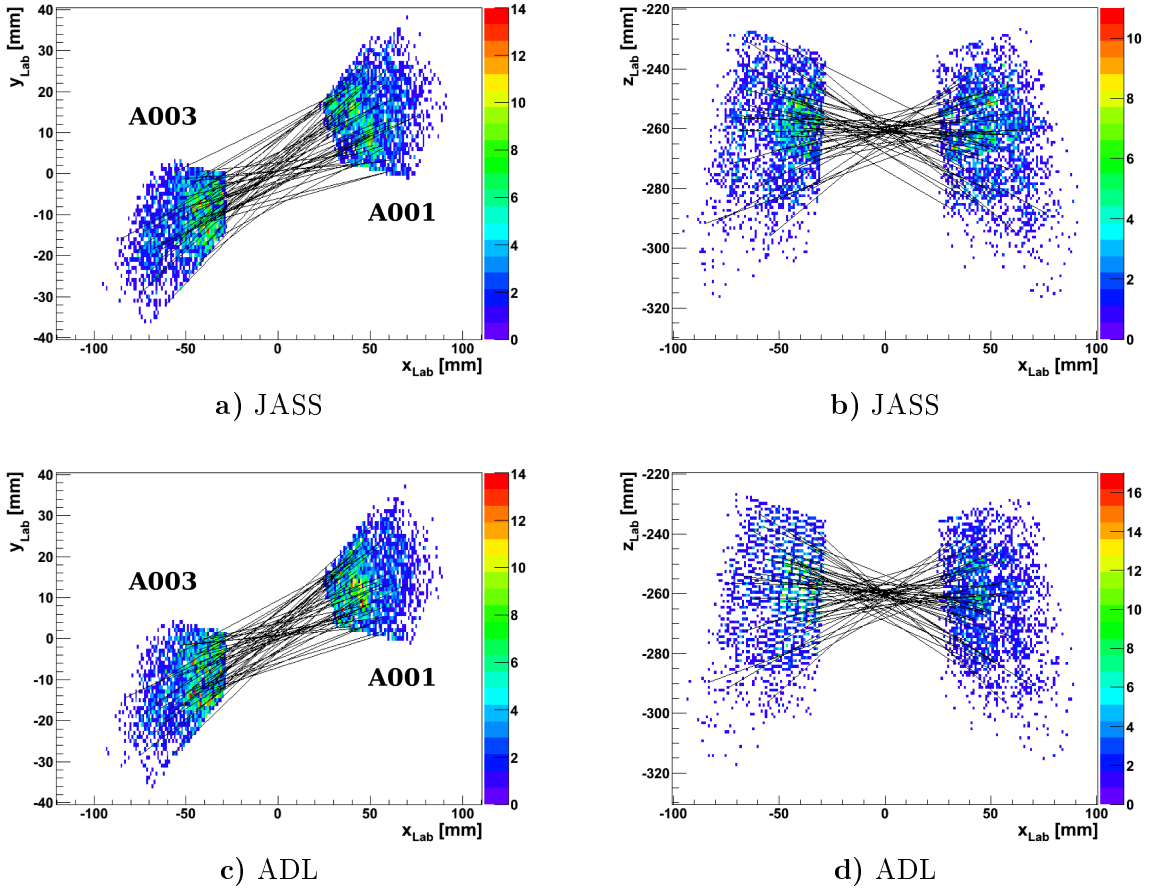

Fig. 4.17: Spatial distributions of the reconstructed barycenters of the Compton segment. The first row shows the results of the JASS signal basis while the second row presents the results of the ADL basis.

due to the PSA algorithm (c.f. sec. 3.2.2). Second, the scattering path of the γ-ray can be misidentified. Thus, the connection line can have a large distance to the source, even if the position reconstruction works perfect.
Nevertheless, there is one effect which leads to a reduction of the smearing of the lines in the two hit-segment analysis compared to the one hit-segment analysis: The influence of the escaping positrons is dramatically reduced by the look-up table which is needed to select Compton scatterings (c.f. sec. 4.1.2). However, despite the look-up table, there are still positrons escaping the source (c.f. fig. 4.10 b)). Thus, the escaping positrons have to be considered in the two hit-segment analysis, too.

4.2.2 Mean Position Resolution

The mean position resolution of the A001 and A003 detector for single interaction positions is determined by a fit of the distance spectrum. For the calculation of the experimental distance spectra the source position of the one hit-segment analysis is used to avoid problems due to misidentified scattering paths. Due to the low statistics, the ratio of random events modeling the escaping positrons cannot be determined precisely by a two parameter fit. Thus, the ratio obtained from the one hit-segment analysis is used, considering additionally the influence

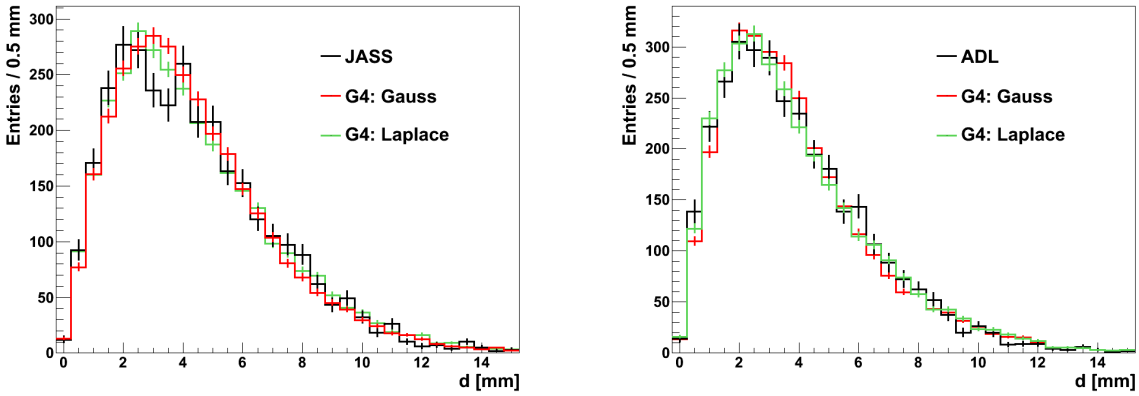

Fig. 4.18: Distance spectra obtained in the two hit-segment analysis using the JASS and the ADL basis. Additionally, the best matching simulated distance spectra are drawn for a Gaussian and a Laplace position smearing including random events.

smearing distribution	random events [%] (fixed)	σ_0(JASS / ADL) [mm] (fitted)	χ^2/Ndf (JASS / ADL)
Gauss	14 / 13	2.3 / 1.9	1.2 / 0.9
Laplace	12	1.8 / 1.5	1.0 / 0.8

Tab. 4.5: The resulting position resolutions of the two hit-segment analysis. They are obtained by a one-parameter fit of the simulated to the experimental distance spectra. The position resolution of the simulation is modeled with a Gaussian or a Laplace distribution including random events to take the escaping positions from the source into account.

of the look-up table[7]. Furthermore, the energy dependence of the PSA position resolution has to be taken into account, since the energy depositions in the Compton segment are not constant. As a reminder, events with an energy deposition between 100 keV and 300 keV in the Compton segment are considered. Low energy depositions yield low signal amplitudes at the detector electrodes which correspond to low signal to noise ratios. Thus, the position resolution deteriorates with decreasing energy. Following the approach of [3], the energy dependence of the position resolution is approximated by

$$\sigma(E) = \sigma_0 \sqrt{\frac{511\,\mathrm{keV}}{E_{\mathrm{Compton}}}}, \tag{4.1}$$

with E_{Compton} being the detected energy in the Compton segment. Eq. (4.1) also explains why the lower energy cut at 100 keV is introduced (c.f. sec. 3.3.2). It ensures that the square root does not dominate over σ_0.
For the determination of the position resolution the simulated distance spectrum is fitted to the experimental distance spectrum using σ_0 as fit parameter. The results for the JASS and the ADL signal basis are summarized in fig. 4.18 and tab. 4.5. Again, the obtained position resolutions are within the requirements of AGATA (FWHM < 5 mm at 1 MeV) if the results are scaled to 1 MeV with the help of eq. 4.1. However, the ADL basis shows again a slightly better performance than the JASS basis. Assuming that the energy dependence of the PSA position resolution, given in eq. (4.1) is correct, the position resolution of the two hit-segment analysis

[7] Note that the position smearing has to be performed before the events are treated with the look-up table. Otherwise the random events would be strongly overestimated.

can be scaled to 511 keV. As a result, the position resolution of the single interaction points is about 0.3 mm worse than the position resolution of the barycenter in the one hit-segment analysis (c.f. tab. 4.2). Possible reasons for this difference are discussed in the following section 4.2.3.

4.2.3 Contributions to the Position Resolution

The discrepancy of the position resolution between the one hit-segment and the two hit-segment analysis can have several reasons. First, it is possible that the energy dependence of the position resolution is not modeled correctly. A further discussion on the energy dependence can be found in sec. 5.4 indicating that the model is not too bad. However, due to the low statistics a reliable statement is not possible. Additionally, the PSA grid search algorithm deteriorates the position resolution in the case of multiple hit segments. As already detailed in sec. 3.2.2 a full grid search is not feasible due to too long computation times. Instead, a faster search algorithm had been implemented which, however, leads to additional errors. Nevertheless, at the current stage, it is not possible to quantitatively investigate the impact of the PSA algorithm on the position resolution. This is done in the scope of the second test measurement in chap. 5 using a different event selection and analysis.

4.3 Combined Analysis

In secs. 4.1 and 4.2 the results of the one and the two hit-segment analysis are presented leading to a position resolution of the barycenter and of single interaction points, respectively. This section deals with a combined analysis: In one crystal single hit segments with a total energy deposition of 511 keV are selected while in the other crystal Compton scatterings of the 511 keV γ-ray from one segment into a neighboring segment are considered. In contrast to the two hit-segment analysis, the combined analysis has several advantages: Due to the look-up table needed in the two hit-segment analysis, the statistics in the distance spectra is poor as ambiguous events are ignored. In the combined analysis the statistics is increased by a factor of 2.6 as only one γ-ray scattering path can feature an ambiguity. Furthermore, assuming that the position resolutions determined by the four-parameter fit are correct (c.f. sec. 4.1.4), the position resolutions of single interaction points for individual crystals can be investigated. This is realized by a one-parameter fit of the simulated to the experimental distance spectrum. As the error of the four-parameter fit is significantly larger, the fit is performed for various resolutions of the barycenter. Note that the random events describing the background due to escaping positrons have to be considered, too. Their percentage is taken from the results of the barycenter analysis (c.f. tab. 4.2).
The results of the combined analysis are summarized in tabs. 4.6 and 4.7 for the Compton scattering being in the A001 and the A003 crystal, respectively. All possible basis permutations have been fitted. The combination of both event selections and both signal bases allows a consistent check. Each position resolution for single interactions is fitted twice using both, the JASS or the ADL signal basis in the other crystal. Thus, the fit results are expected being equal. Comparing the obtained resolutions in tabs. 4.6 and 4.7 this is indeed the case. Thus, for each crystal a mean position resolution can be calculated from both fits. For a better overview these mean values are summarized in tab. 4.8. The mean values of the A001 and A003 crystal coincide with the results from the two hit-segment analysis (c.f. tab. 4.5). Like in the four-parameter fit the obtained position resolution of the ADL basis in the A001 crystal outperforms the other resolutions (c.f. tab. 4.4). Furthermore, the resolutions of the JASS basis and the ADL resolution in the A003 crystal are quite similar which is consistent with the result of the four-parameter fit.

smearing distr.	random events [%]	A003 basis	σ(A003) [mm] (fixed)	A001 basis	σ_0(A001) [mm] (fitted)	χ^2/Ndf
Gauss	14	JASS	2.2	JASS	2.1	1.8
Gauss	13.5	ADL	2.1	JASS	2.2	2.0
Gauss	13.5	JASS	2.2	ADL	1.5	2.4
Gauss	13	ADL	2.1	ADL	1.5	2.1
Laplace	12	JASS	1.5	JASS	1.8	1.5
Laplace	12	ADL	1.5	JASS	1.8	1.5
Laplace	12	JASS	1.5	ADL	1.3	2.0
Laplace	12	ADL	1.5	ADL	1.2	1.8

Tab. 4.6: Results of the combined analysis. In the A001 crystal events are selected according to the two hit-segment analysis while the event selection of the A003 detector is based on the one hit-segment analysis. For the energy dependence of the position smearing of the Compton events in A001 eq. (4.1) is assumed.

smearing distr.	random events [%]	A001 basis	σ(A001) [mm] (fixed)	A003 basis	σ_0(A003) [mm] (fitted)	χ^2/Ndf
Gauss	14	JASS	1.8	JASS	2.2	1.8
Gauss	13.5	ADL	0.7	JASS	2.2	1.9
Gauss	13.5	JASS	1.8	ADL	2.1	1.6
Gauss	13	ADL	0.7	ADL	2.2	2.0
Laplace	12	JASS	1.4	JASS	1.7	1.7
Laplace	12	ADL	0.7	JASS	1.7	1.8
Laplace	12	JASS	1.4	ADL	1.8	1.6
Laplace	12	ADL	0.7	ADL	1.7	2.0

Tab. 4.7: Results of the combined analysis. In the A003 crystal events are selected according to the two hit-segment analysis while the event selection of the A001 detector is based on the one hit-segment analysis. For the energy dependence of the position smearing of the Compton events in A003 eq. (4.1) is assumed.

smearing distribution	σ_0(A001, JASS) [mm]	σ_0(A003, JASS) [mm]	σ_0(A001, ADL) [mm]	σ_0(A003, ADL) [mm]
Gauss	2.1	2.2	1.5	2.2
Laplace	1.8	1.7	1.3	1.8

Tab. 4.8: Obtained position resolutions of the A001 and A003 crystal for single γ-ray interaction points derived from mean values of column six from tabs. 4.6 and 4.7.

Chapter 5

Test Experiment with an Asymmetric Source Position

The results of the symmetric test experiment have demonstrated that the calibration experiment is capable to extract the position resolution of the AGATA detectors. However, the determination of the resolution of individual crystals is challenging, time consuming and not fully independent. Thus, a second test measurement was performed. Its setup is visualized in fig. 2.4. In contrast to the symmetric test experiment, the ^{22}Na source is positioned on the cryostat wall of the A006 crystal (c.f. sec. 2.2). Due to the asymmetric source position the position resolution of the A006 detector can be determined nearly independently of the resolution of other crystals (c.f. sec. 5.1). Sec. 5.2 deals with the reconstruction of the segment barycenter whereas sec. 5.3 discusses the position resolution of single interaction points. Furthermore, the energy dependence of the position resolution is studied in sec. 5.4. The chapter concludes in sec. 5.5 with a new event selection which allows to determine the position resolution of single interactions without the negative influence of the PSA algorithm.

5.1 Advantage of the Asymmetric Source Position

In the symmetric test experiment the source is positioned in the center between the analyzed crystals. Thus, the distance spectra is influenced by the position resolution of both crystals to the same degree as the mean lever arms of the source to the interaction points in the crystals have both the same length. Contrary, in the asymmetric test measurement the source is positioned as close as possible to one crystal, i.e. at its cryostat (c.f. fig. 5.1 a)). As a result, the lever arm to the near detector is much shorter than the lever arm to the far detector. Therefore, the distance spectra is mainly influenced by the near detector. This behavior is further illustrated in fig. 5.1 b) showing four simulated distance spectra with different position smearing in the near and the far detector[1]. If the position resolutions of the near detector are kept constant the distance spectra are quite similar even though the resolutions of the far detector differ in 2 mm. However, if the position resolution of the near detector is varied by 2 mm, the spectra are significantly different, even if the position resolution of the far detector does not change. Therefore, the influence of the near crystal is indeed dominant. Fig. 5.2 quantifies the influence of the far detector. It shows the resulting resolution σ(fitted) of the near detector obtained by fitting simulated distance spectra with different resolutions of the near (σ(near)) and the far detector (σ(far)). In the fit it is assumed that both crystals feature the same position resolution. Due to the shorter lever arm of the near crystal to the source, the fitted resolutions are still close to the initial resolution of the near detector A006 with

[1] As an example the A002 crystal is chosen as far detector.

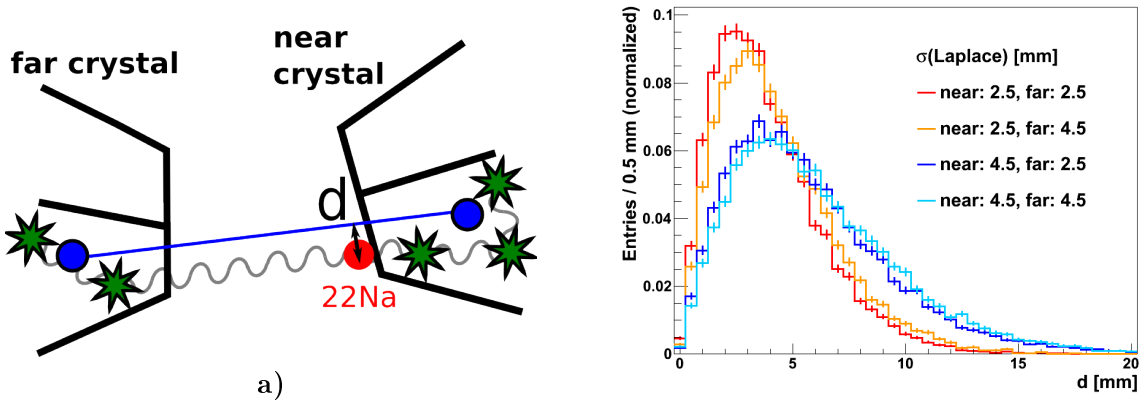

Fig. 5.1: **a)** Advantage of the asymmetric source position. Due to the short lever arm of the source to the interaction point in the near detector compared to the long lever arm of the interaction positions in the far detector, the distance d is mainly influenced by the position resolution of the near detector. Thus, the resolution of the near detector can be determined almost independently of the resolution of the far detector. Note that the image if not to scale. **b)** Simulated distance spectra with different smearing of the near and the far detector.

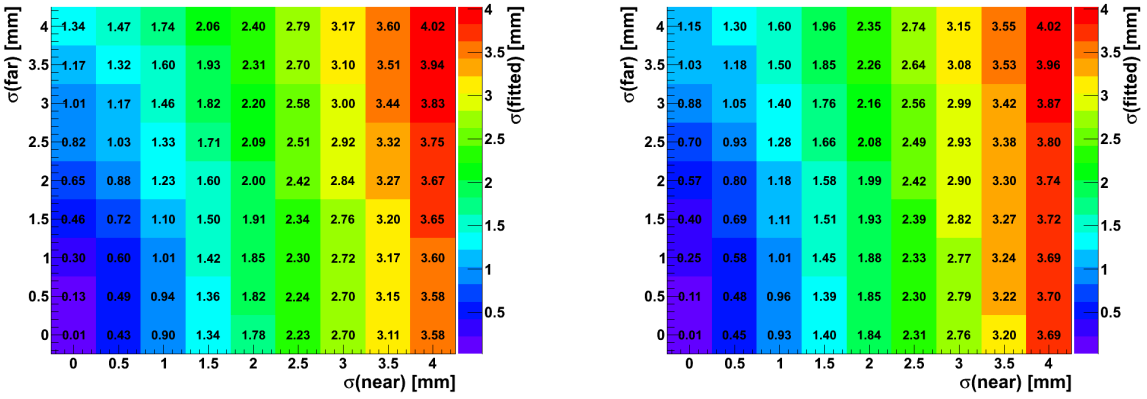

a) A006 in coincidence with A002 **b)** A006 in coincidence with A003

Fig. 5.2: Fitted position resolutions σ(fitted) of the near detector A006 for different simulated Laplace resolutions of the near (σ(near)) and the far detector (σ(far)). The fit assumes that the resolution in the near and the far detector are equal. As far detector the A002 and the A003 crystal are chosen. The source is positioned at segment E4 of the A006 detector.

only a slight shift in the direction of the resolution of the far detector. The precision of the obtained resolution is significantly improved if the resolution of the far detector is at least roughly known. As a result, the position resolution of individual crystals can be determined.

5.2 One Hit-Segment Analysis

In this section the results of the one hit-segment analysis are presented for the JASS and the ADL signal basis. Thus, the position resolution of the reconstructed barycenter in the near crystal A006 is determined. The event selection is based on sec. 3.3.1: In the A006 crystal one 511 keV γ-ray of the ^{22}Na source has to be totally absorbed in a single segment. The second annihilation γ-ray is detected in coincidence in one of the opposing detectors A002 or A003. The distance spectrum is calculated with the events passing the selection cuts. It is subsequently fitted to determine the position resolution of the barycenters (c.f. sec. 3.4.5). The obtained position resolutions are presented and discussed in sec. 5.2.1. Sec. 5.2.2 details an alternative analysis that replaces the reconstructed barycenters of the far detector with the segment center of the hit segment. This approximation allows to determine the position resolution of the near A006 crystal independently of the position resolution of the far detector. Furthermore, the analyses are performed separately for both crystals A002 and A003.

5.2.1 Using the Reconstructed Barycenter of the Far Detector

Spatial distributions of the reconstructed interaction positions
The reconstructed barycenters of the JASS and the ADL basis which pass the event selection are displayed in figs. 5.3 and 5.4 for the exemplary source position at segment E4 (row 4, sector E) of the A006 cryostat. For a better comparison the reconstructed barycenters of a Geant4 simulation with perfect position resolution are displayed, too. In contrast to the symmetric test measurement, the smearing of the lines in the simulation and the experiment differ not much. Hence, the position resolution of the A006 crystal seems to be better than the resolutions of the crystals A001 and A003 used in the first test experiment.
Due to the orientation of the A002 and the A003 detector with respect to the A006 crystal, the analyzed area in the A006 crystal depends on the crystal which detects the second γ-ray. The distribution of the simulated barycenters in the A006 detector is visualized in fig. 5.5 for coincident events in the A002 and the A003 crystal, respectively. Both analyzed regions are almost disjunct. Combining both regions, the whole x-y plane of the A006 crystal is covered. Additionally, the reconstructed interaction points in the A006 detector of the JASS and the ADL basis are shown in app. C.

Position resolution of the A006 crystal
Before the distance spectra can be calculated the source positions have to be determined. They are fitted following the procedure introduced in sec. 3.4.2. Like in the symmetric test measurement the obtained source positions of the JASS and the ADL basis coincide well. In the Geant4 simulation the mean source position is used. A summary of all seven source positions is visualized in fig. 2.4 b) with respect to the segmentation of the A006 crystal.
The position resolution of the A006 detector is determined with a one-parameter fit of the simulated to the experimental distance spectra. The fit is performed twice, assuming a Gaussian and a Laplace distribution for the position smearing in the simulation, respectively. An example of the measured and the best fitting simulated distance spectra are shown in fig. 5.6 for the source being positioned at the segment E4 (row 4, sector E) of the A006 crystal. Comparing the measured with the simulated distance spectra, all fits perform well. Thus, contrary to the symmetric test experiment, no additional random contribution in the smearing distribution is

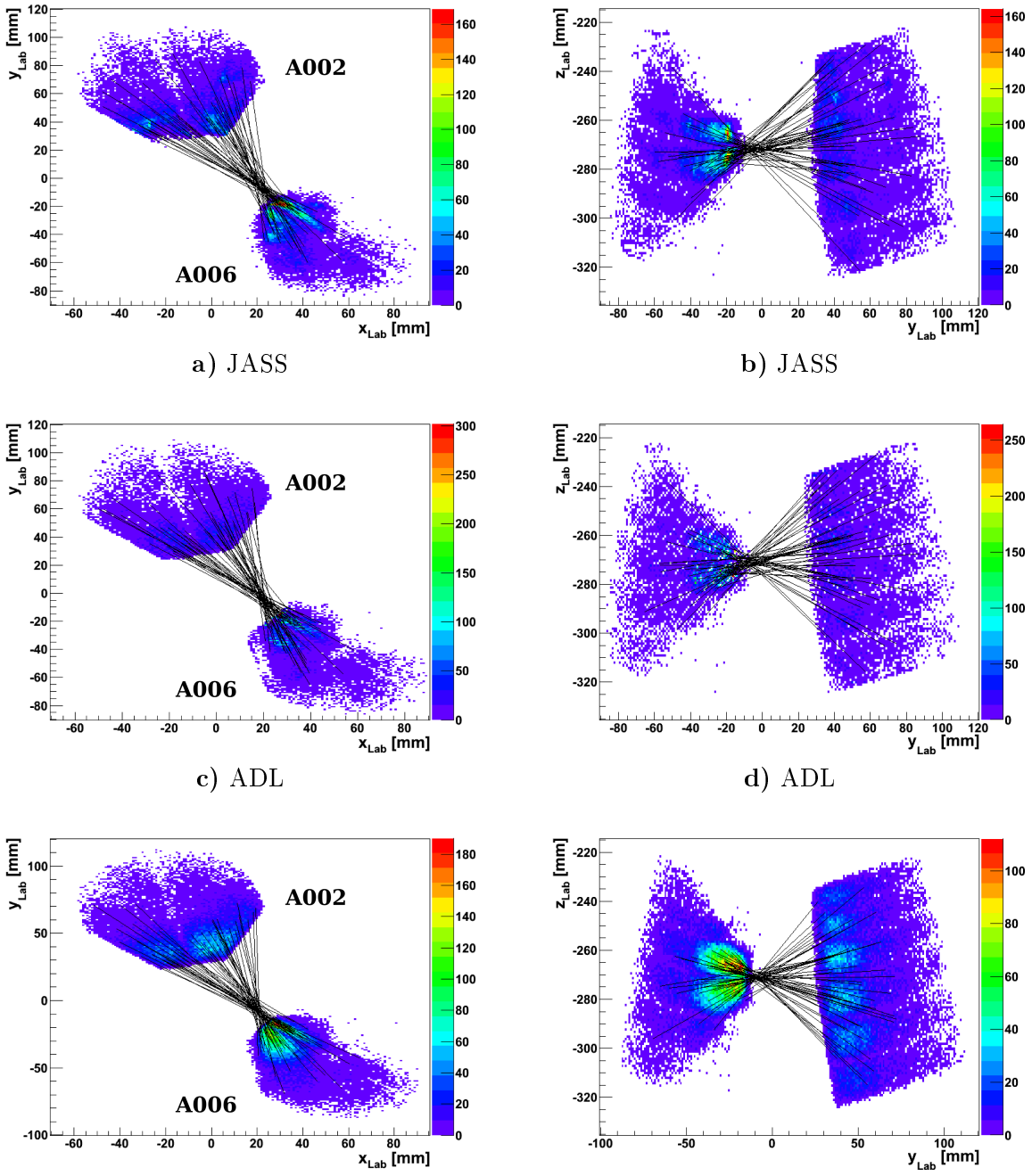

a) JASS b) JASS

c) ADL d) ADL

e) Geant4 f) Geant4

Fig. 5.3: Two dimensional plots of the coincident interaction positions of the A006 crystal and the A002 crystal. The first and second row show the barycenters reconstructed with the JASS and the ADL basis, respectively. For comparison the bottom row displays the interaction points of a Geant4 simulation with perfect position resolution. The ^{22}Na source is positioned at row four of the A006 cryostat. The left column presents a front view of the crystals whereas in the right column a side view of the same events selected is shown.

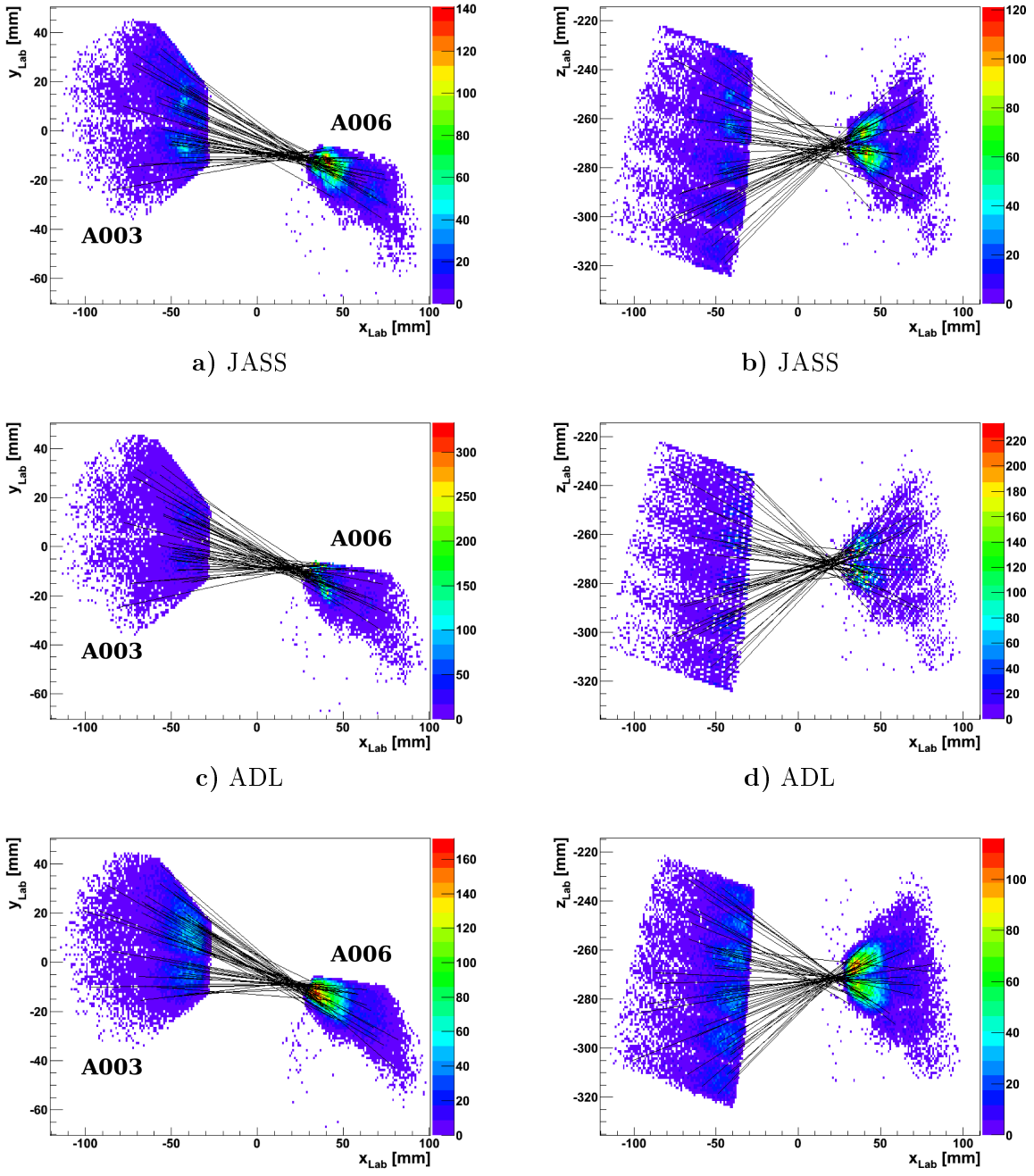

a) JASS b) JASS

c) ADL d) ADL

e) Geant4 f) Geant4

Fig. 5.4: Two dimensional plots of the coincident interaction positions of the A006 crystal and the A003 crystal. The first and second row show the barycenters reconstructed with the JASS and the ADL basis, respectively. For comparison the bottom row displays the interaction points of a Geant4 simulation with perfect position resolution. The ^{22}Na source is positioned at row four of the A006 cryostat. The left column presents a front view of the crystals whereas in the right column a side view of the same events selected is shown.

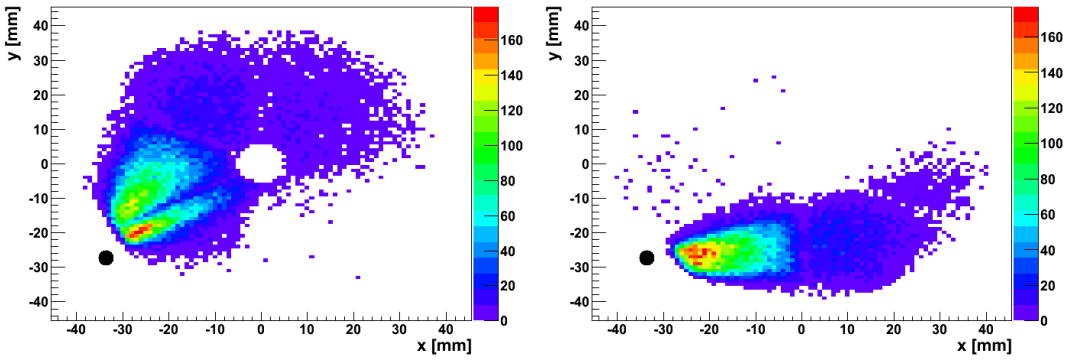

Fig. 5.5: Simulated distributions of the barycenters in the A006 detector in coincidence with the A002 crystal (**a**)) and the A003 crystal (**b**)). The source position is marked with a black dot. As the barycenter tend to cluster in the segment center, the segmentation lines are visible.

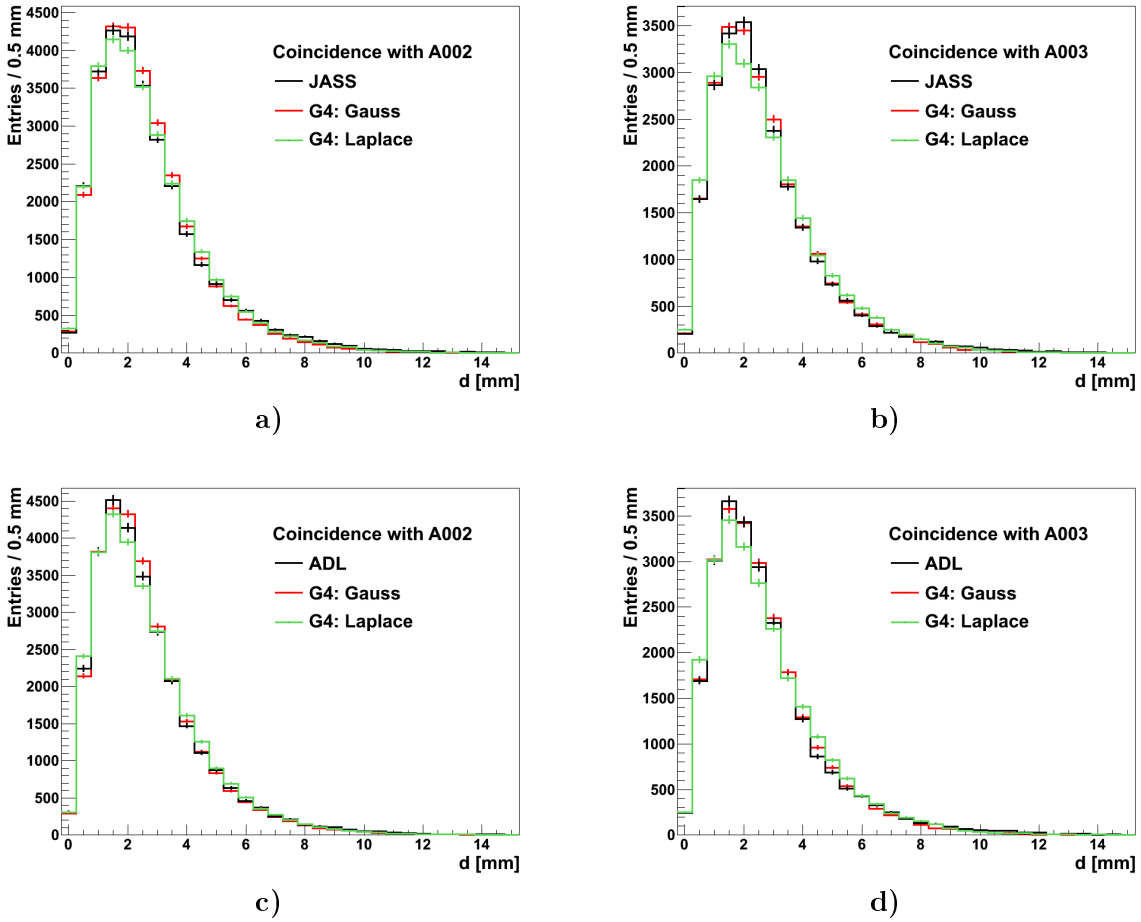

Fig. 5.6: Comparison of the experimental and best fitting Geant4 distance spectra for the JASS and the ADL basis. The source is positioned at segment E4 of the A006 cryostat. The A006 crystal was analyzed separately in coincidence with the crystals A002 and A003.

segment	basis	σ(Laplace) [mm] A002 / A003	χ^2/Ndf A002 / A003	σ(Gauss) [mm] A002 / A003	χ^2/Ndf A002 / A003
E1	JASS	1.2 / 1.5	1.3 / 1.6	1.6 / 1.9	1.7 / 1.1
	ADL	1.3 / 1.5	1.3 / 1.4	1.7 / 1.9	1.9 / 1.3
E1	JASS	1.2 / 1.5	1.3 / 1.1	1.5 / 1.9	2.0 / 1.0
	ADL	1.1 / 1.3	0.9 / 1.3	1.4 / 1.7	0.9 / 1.1
E2	JASS	1.5 / 1.5	1.7 / 1.3	1.9 / 2.0	2.8 / 1.5
	ADL	1.1 / 1.2	0.9 / 1.2	1.4 / 1.5	1.6 / 1.0
E3	JASS	1.4 / 1.2	3.1 / 2.6	1.8 / 1.6	4.0 / 2.0
	ADL	1.2 / 1.2	2.5 / 3.0	1.5 / 1.6	2.1 / 2.9
E4	JASS	1.4 / 1.4	3.2 / 3.2	1.8 / 1.8	4.5 / 2.1
	ADL	1.3 / 1.3	1.9 / 3.7	1.7 / 1.7	1.8 / 2.7
E5	JASS	1.5 / 1.6	1.5 / 1.7	2.0 / 2.1	1.8 / 1.2
	ADL	1.3 / 1.5	1.2 / 1.6	1.7 / 2.0	1.1 / 1.8
E6	JASS	1.7 / 1.8	1.0 / 1.6	2.3 / 2.4	1.3 / 0.9
	ADL	1.8 / 2.0	1.4 / 2.5	2.4 / 2.6	1.0 / 1.3

Tab. 5.1: Position resolutions of the A006 detector in the asymmetric ^{22}Na test measurement. The resolutions are determined by fitting the experimental distance spectra. They are calculated with the reconstructed barycenters of the A006 and of the A002 / A003 crystal.

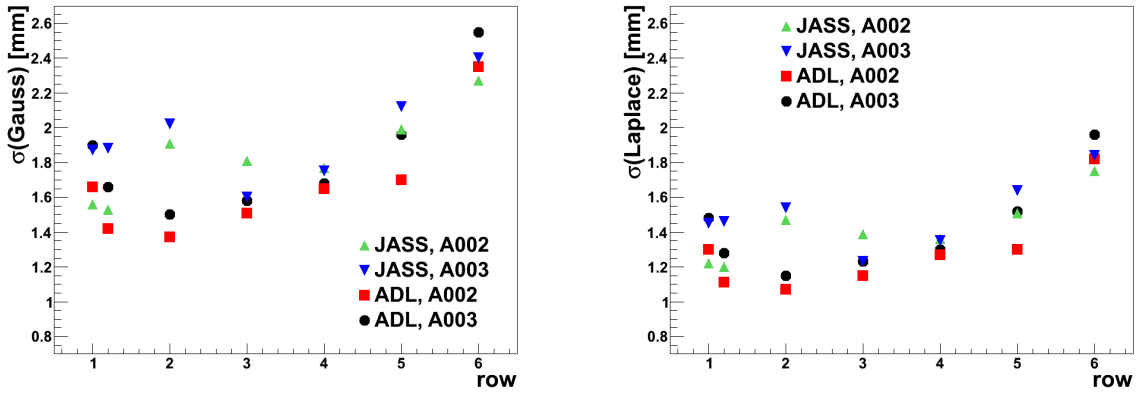

Fig. 5.7: Obtained position resolutions of the A006 detector. The x-axis corresponds to the row where the source is located. The position resolutions are determined by fitting the experimental distance spectra. They are calculated with the reconstructed barycenters of the A006 and of the A002 / A003 crystal.

necessary. Hence, this result indicates that the random events in the first test experiments are indeed due to escaping positrons which mimic a degraded position resolution.
The obtained position resolutions for all seven source positions are summarized in tab. 5.1 and fig. 5.7 for a Gaussian and a Laplace position smearing, respectively. According to the χ^2/Ndf-values the distance spectra of the measurement and the simulation coincide. However, it cannot be concluded that one smearing model always outperforms the other. All obtained resolutions fulfill the requirements for the AGATA PSA (FWHM $<$ 5 mm at 1 MeV [6]). Furthermore, the JASS basis leads to a better position resolution in the first and the last row of the A006 crystal than the ADL basis. In the other rows, the ADL basis outperforms JASS.
The general dependence of the position resolution on the crystal row where the source is

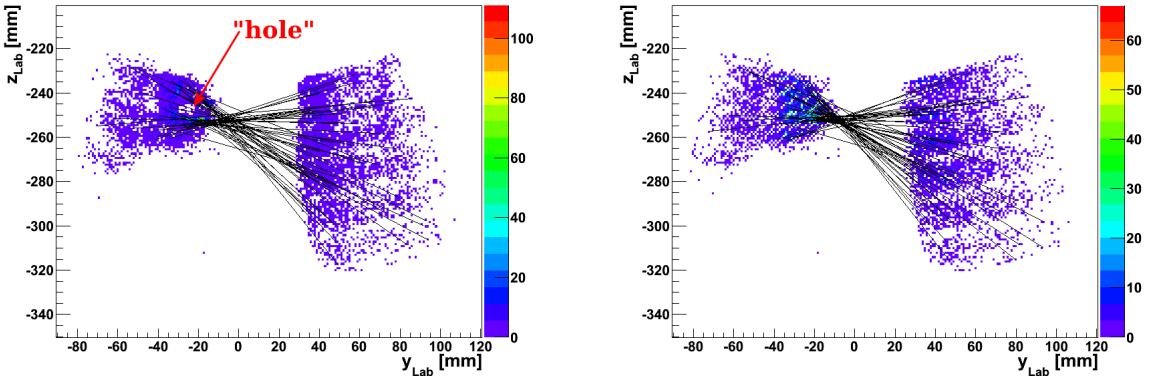

Fig. 5.8: Comparison of the distribution of the interaction points reconstructed with the JASS and the ADL basis. Due to the systematic shifts in JASS resulting in a "hole" in the spatial distribution of the A006 crystal near the source position, the position resolution is worse compared to the ADL basis.

positioned, is not random. The first row features a deteriorated resolution compared to the second row. This can be caused by the complicated structure of the electric field in the first row which is challenging to calculate in the signal basis (c.f. fig. 1.7 a)). Small errors in the electric field can yield wrong trajectories for the drifting electrons and holes and consequently to badly modeled pulse shapes. Another reason can be the PSA itself. As detailed in sec. 3.2.2 the PSA performance deteriorates if the hit segment is not totally surrounded by neighboring segments which are included in the PSA. Hence, the same fact also leads to a worse position resolution in the last segment row. Furthermore, from row two to six, the position resolution degrades as the volume of the effective segments increases with increasing row number. In huge segments it is more likely that a γ-ray interaction point is reconstructed with a large error. However, comparing the ADL results with the JASS results, there is a clear outlier in row two of the JASS basis. It can be explained with fig. 5.8 showing the spatial distributions of the corresponding reconstructed barycenters. Comparing the plots, there is a clear "hole" for the JASS basis at the border between segment row one and two which is not present in the ADL basis and the Geant4 simulation. The "hole" indicates a systematic error in JASS signal basis.

5.2.2 Using the Segment Center of the Far Detector

The fitted position resolutions in sec. 5.2.1 provide a deep insight into the resolution of the whole A006 crystal. Nevertheless, the impact of the far detector on the obtained position resolution cannot be neglected. Therefore, a slightly different analysis is performed. Instead of the reconstructed barycenter of the far crystal with unknown resolution the segment center of the hit segment is used as input to calculate the distance spectrum of both, of the measurement and of the simulation. Thus, the impact of the far detector is the same in the experiment and in the simulation. Although replacing the reconstructed barycenter with the segment center is a rough approximation, the long lever arm of the source to the far detector ensures that the influence of the segment center does not dominate over the influence of the A006 position resolution in the distance spectrum. This is also illustrated in fig. 5.9 showing simulated distance spectra with different position smearing in the A006 crystal and with taking the segment center in the far detector.
As a result, the position resolution of the A006 detector can be determined independently

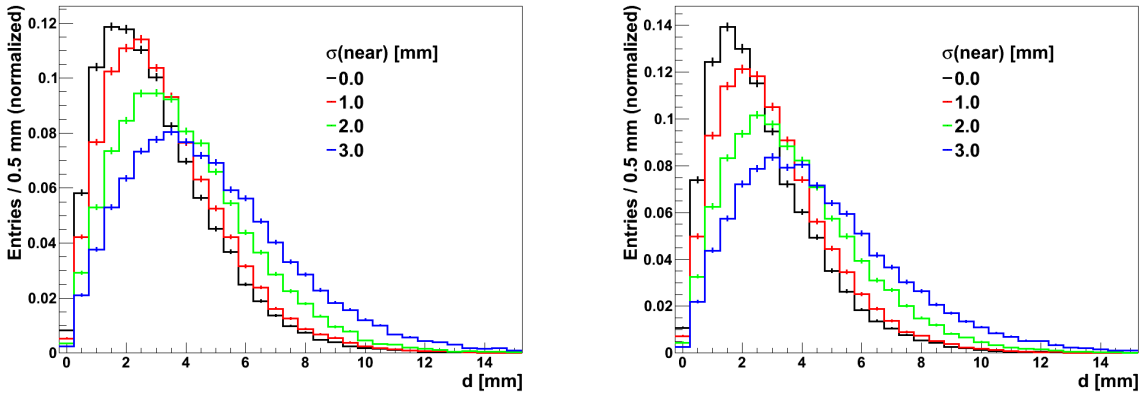

Fig. 5.9: Simulated distance spectra. In the near A006 crystal a Laplace position smearing is assumed while in the far crystals A002 (**a**)) and A003 **b)** the segment center is used to calculate the spectra.

segment	basis	σ(Laplace) [mm] A002 / A003	χ^2/Ndf A002 / A003	σ(Gauss) [mm] A002 / A003	χ^2/Ndf A002 / A003
E1	JASS	0.80 / 1.4	1.0 / 1.3	1.1 / 1.7	1.1 / 1.0
	ADL	1.1 / 1.5	1.2 / 2.0	1.5 / 2.0	1.8 / 1.6
E1	JASS	0.88 / 1.3	1.1 / 1.4	1.2 / 1.6	1.3 / 1.4
	ADL	0.88 / 1.1	1.3 / 1.2	1.2 / 1.4	1.1 / 1.1
E2	JASS	1.3 / 1.5	1.7 / 1.3	1.7 / 2.0	1.5 / 1.1
	ADL	0.8 / 1.1	1.2 / 1.4	1.2 / 1.5	1.2 / 1.3
E3	JASS	1.0 / 0.9	2.6 / 2.4	1.3 / 1.2	2.7 / 4.3
	ADL	0.8 / 1.0	3.4 / 3.7	1.2 / 1.2	4.0 / 2.7
E4	JASS	0.8 / 1.1	3.3 / 3.0	1.1 / 1.5	4.0 / 2.2
	ADL	0.9 / 1.2	2.4 / 4.5	1.2 / 1.6	1.9 / 4.7
E5	JASS	1.3 / 1.4	1.0 / 1.4	1.7 / 1.8	1.1 / 1.6
	ADL	1.1 / 1.4	1.0 / 2.4	1.4 / 1.9	1.1 / 2.3
E6	JASS	1.5 / 1.6	1.4 / 1.3	2.0 / 2.1	1.3 / 1.3
	ADL	1.6 / 1.8	1.8 / 1.9	2.1 / 2.4	1.5 / 2.0

Tab. 5.2: Position resolutions of the A006 detector in the asymmetric ^{22}Na test measurement. The resolutions are determined by fitting the experimental distance spectra. They are calculated with the reconstructed barycenters of the A006 and the segment centers of the hit segment in the A002 / A003 crystal.

of the resolution of the far detector. This is done with a one-parameter fit of the distance spectrum using the resolution of the near detector as free parameter. The obtained resolutions are summarized in tab. 5.2 and fig. 5.10. All resolutions fulfill the demand of AGATA, i.e. a FWHM < 5 mm for a 1 MeV γ-ray energy deposition for the PSA position resolution [6]. Moreover, the resolutions of the A006 crystal obtained in coincidence of the A002 crystal are slightly better for both bases than the resolution obtained in coincidence with A003. Thus, the segment E of the A006 crystal features a better PSA performance than segment D (c.f. fig. 5.5). Generally, the results in fig. 5.10 obtained with the segment center in the far detector (barycenter - segment center analysis) are close to the results obtained with the barycenter in the far detector (barycenter - barycenter analysis) in fig. 5.7. For a more detailed comparison,

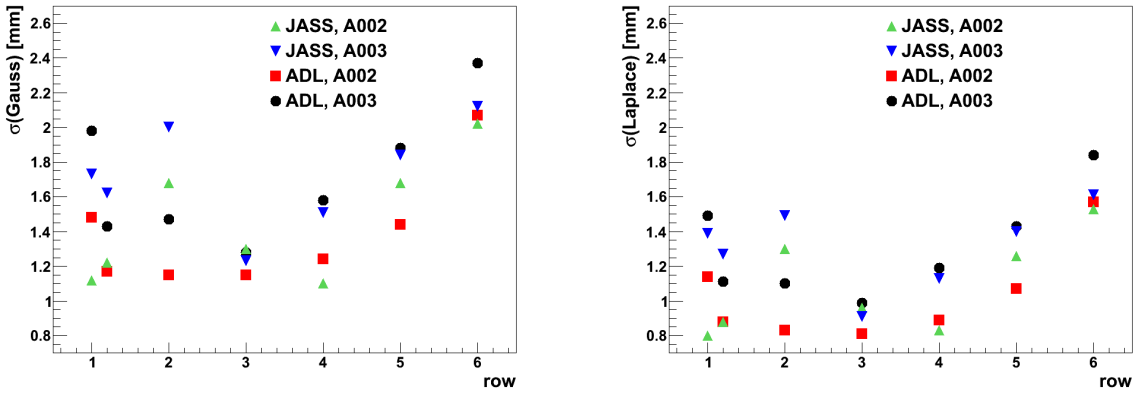

Fig. 5.10: Obtained position resolutions of the A006 detector. The x-axis corresponds to the row where the source is located. The position resolutions are determined by a fit of the distance spectra which are calculated with the barycenter of the A006 and the segment center of hit segment of the far crystals (A002 / A003).

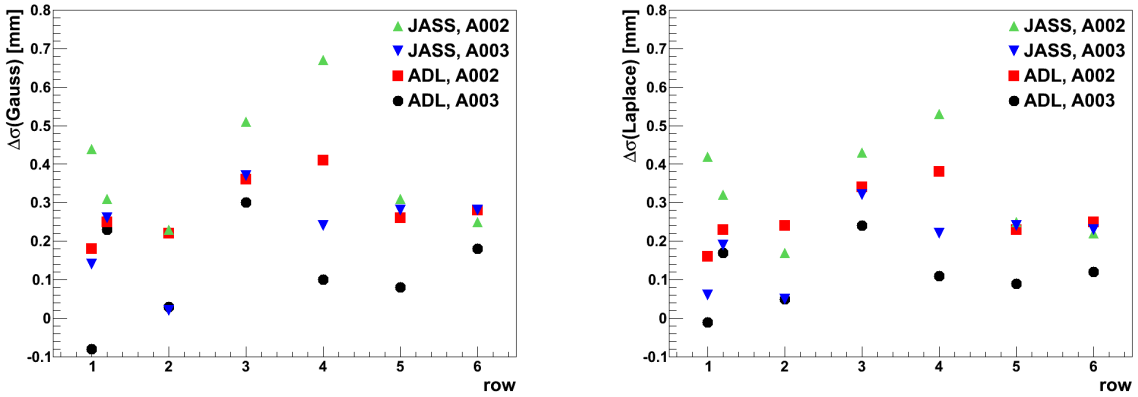

Fig. 5.11: The deviation $\Delta\sigma = \sigma$(barycenter - barycenter analysis) - σ(barycenter - segment center analysis). The resolution σ(barycenter - barycenter analysis) is obtained using the reconstructed barycenter in the far detector (c.f. fig. 5.7) while σ(barycenter - segment center analysis) corresponds to the resolution using the segment center of the hit segment in the far crystal (c.f. fig. 5.10).

the deviation of the position resolutions of both analysis types is presented in fig. 5.11. The difference σ(barycenter - barycenter analysis) - σ(barycenter - segment center analysis) is related to the different treatment of the far detector in the two analyses: The barycenter - barycenter analysis considers the reconstructed interaction points of the far detector. Contrary, the barycenter - segment center analysis is completely independent of the resolution of the far detector as it always uses the segment center in the far crystal instead of the reconstructed interaction point. Therefore, the comparison of the both analyses shows the influence of the position resolution of the far detector. According to figs. 5.2 the fitted position resolution of the A006 crystal in the barycenter - barycenter analysis is always shifted towards the position resolution of the far detector because the fit assumes that the position resolution of the near and the far detector is the same. Therefore, the positive difference σ(barycenter - barycenter analysis) - σ(barycenter - segment center analysis) shows that the position resolution of the far crystals A002 and A003 is worse compared to the position resolution of the A006 crystal. This

segment	basis	σ(Laplace) [mm] A002 / A003	χ^2/Ndf A002 / A003	σ(Gauss) [mm] A002 / A003	χ^2/Ndf A002 / A003
E3	JASS	1.9 / 1.6	12.0 / 1.1	2.4 / 2.1	22.9 / 3.3
	ADL	1.4 / 1.5	6.1 / 3.3	1.8 / 1.9	11.0 / 7.0
E4	JASS	1.8 / 1.8	18.6 / 1.5	2.2 / 2.3	33.9 / 4.9
	ADL	1.3 / 1.5	11.2 / 2.5	1.6 / 1.9	16.0 / 6.0

Tab. 5.3: Obtained resolutions of the A006 crystal of the combined analysis, i.e. events with a Compton scattering in the A006 detector are considered. To be independent of the position resolution of the far detector the distance spectra are calculated using the segment center of the segment featuring the energy deposition.

result is also consistent with the obtained resolutions of the A003 crystal in the symmetric test measurement (c.f. tab. 4.4). However, the deviations between the analysis with the barycenter and the segment center are not severe. Thus, the influence of the far detector is indeed not essential.

5.3 Combined Analysis

In the previous section the resolution of the barycenter in the A006 detector was discussed. This section deals with the position resolution of single interaction points. Therefore, events featuring a Compton scattering of one annihilation γ-ray from one segment into a neighboring segment of the A006 crystal are selected according to sec. 3.3.2. The second annihilation γ-ray is detected in coincidence in the far detector A002 or A003. For the determination of the position resolution, the distance spectrum is calculated using the reconstructed barycenter in the Compton segment of the A006 detector and the segment center in the far detector to be completely independent of the position resolution of the far detector. Nevertheless, the analysis can only be performed with the source positions E3 and E4 as the other measurements do not have enough statistics.
Analog to sec. 5.2 the data were analyzed separately for both far detectors A002 and A003. Furthermore, the same energy dependence as in sec. 4.2 is assumed which is given by eq. (4.1). The results of a one-parameter fit to the experimental distance spectra of the JASS and the ADL basis are presented in tab. 5.3. Contrary to the one-hit-segment analysis the Laplace distributions always seems to be more realistic than the Gaussian distribution. However, according to the goodness of fit χ^2/Ndf only the reconstructed barycenters of the A006 detector in coincidence with the A003 crystal can be described sufficiently well with a Laplace distribution. The χ^2/Ndf-values obtained with the A002 crystal are much worse. To get a better understanding of this discrepancy, the spatial distribution of the reconstructed barycenters in the Compton segment of the A006 crystal are plotted in figs. 5.12 and 5.13 for the source at segment E3 and E4, respectively. Comparing the obtained x-y-distributions of the JASS and the ADL signal basis with the Geant4 simulation, both signal bases feature additional peaks in the reconstructed barycenters of the A006 crystal in coincidence with the A002 crystal. These clusters are visible for both source positions and are marked with arrows in figs. 5.12 and 5.13. Thus, the distance spectrum can be divided into two parts, the spectrum with events outside and inside these clusters (c.f. fig. 5.14). As expected, the cluster feature predominantly high entries in the distance spectra which corresponds to a worse position resolution. Therefore, the distribution of the reconstructed barycenters around their true coordinates cannot be described by a simple Gaussian or Laplace distribution. As the events are clearly divided into two groups the smearing distribution should reflect this division. Therefore, the modified

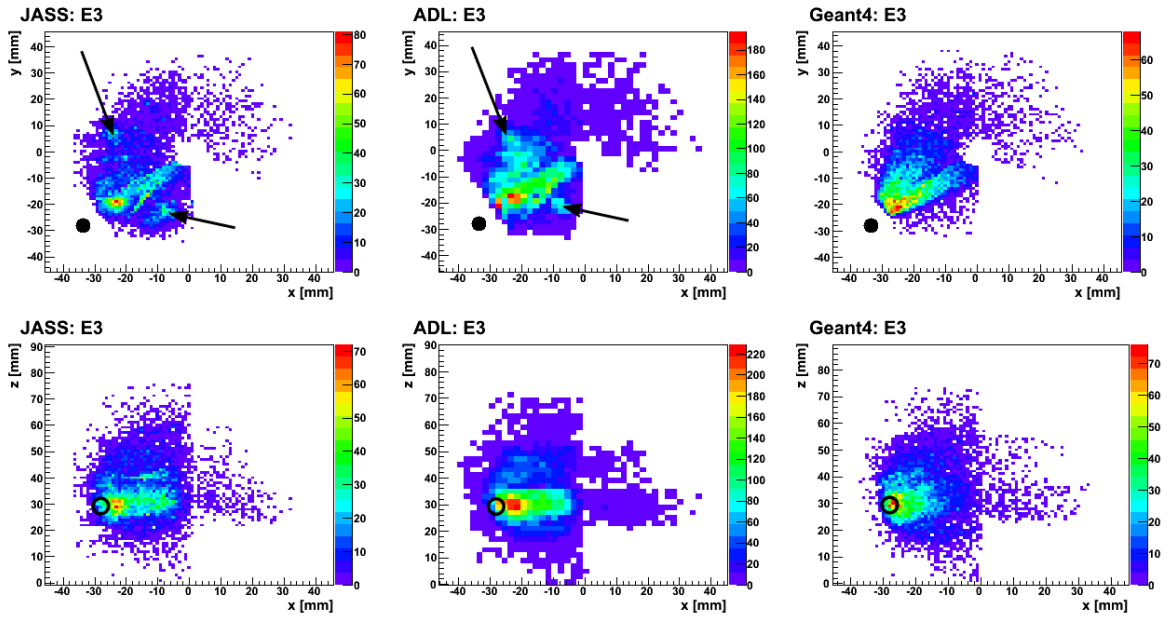

a) A006 in coincidence with A002

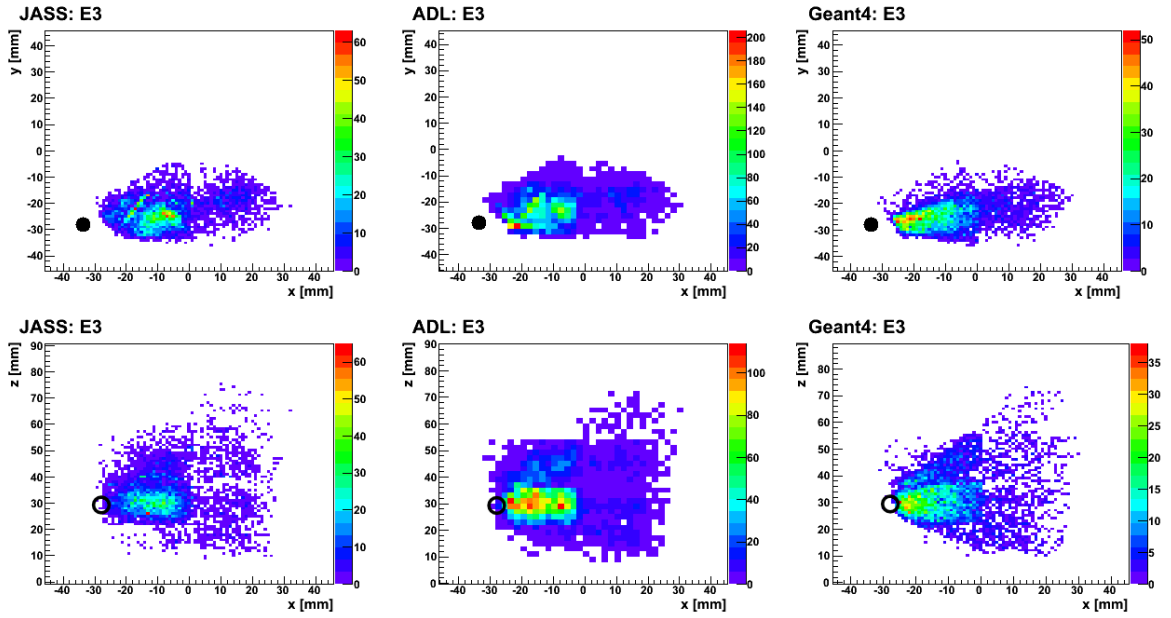

b) A006 in coincidence with A003

Fig. 5.12: Spatial distribution of the interaction points in the Compton segment of the A006 crystal. The source is positioned at row 3 (segment E3) at the A006 cryostat wall. It is marked with a black dot or open circle. The arrows show the clusters with badly reconstructed interaction points.

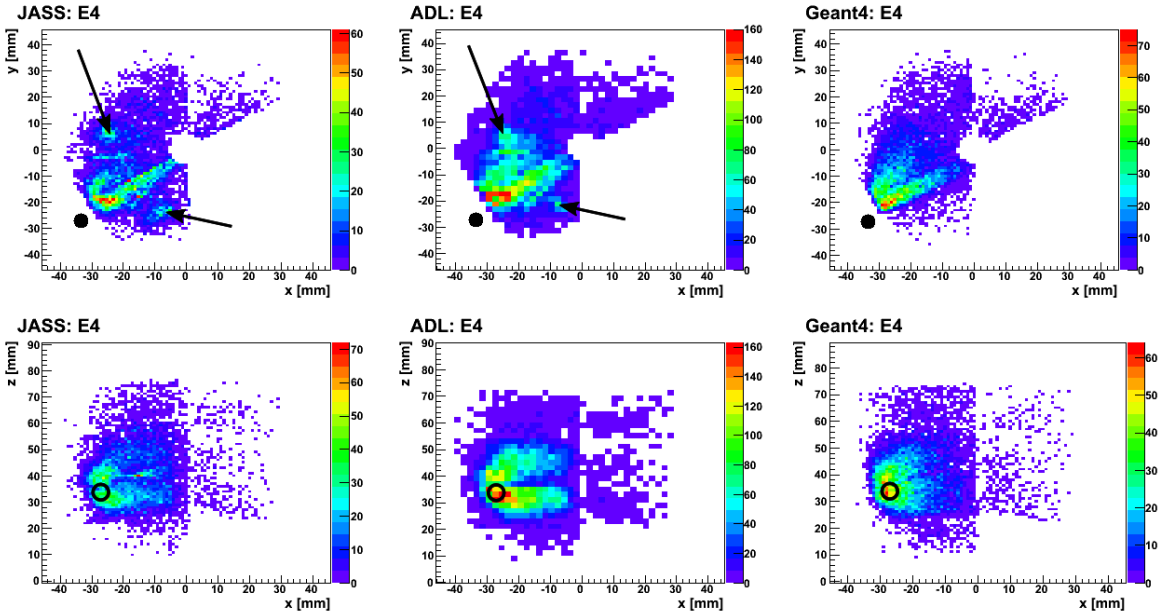

a) A006 in coincidence with A002

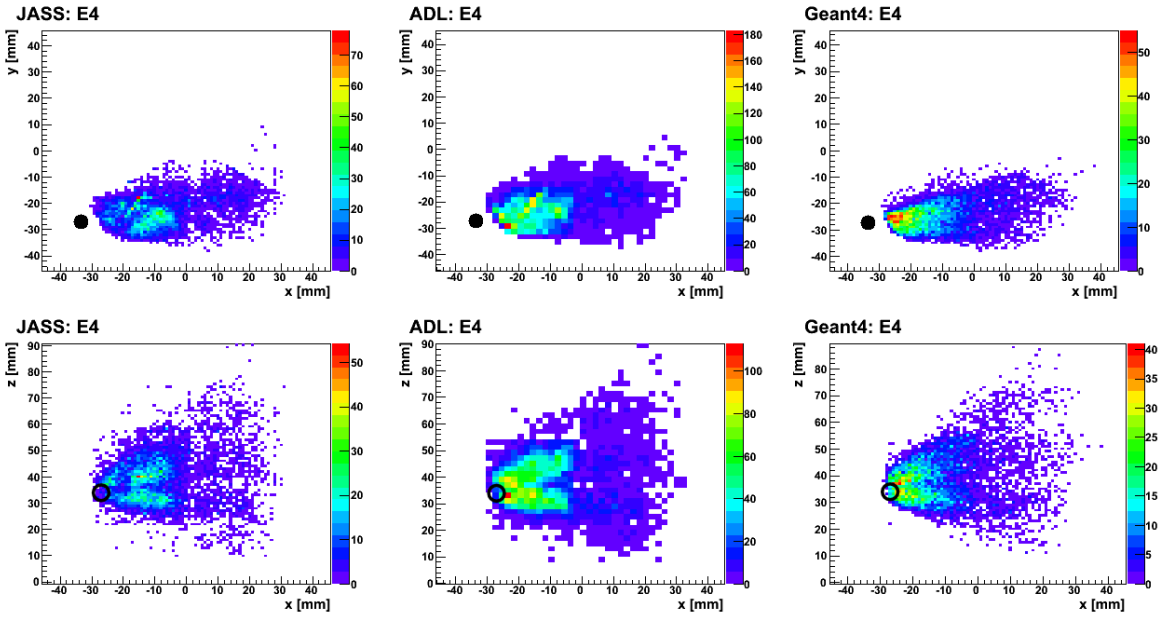

b) A006 in coincidence with A003

Fig. 5.13: Spatial distribution of the interaction points in the Compton segment of the A006 crystal. The source is positioned at row 4 (segment E4) at the A006 cryostat wall. It is marked with a black dot or open circle. The arrows show the clusters with badly reconstructed interaction points.

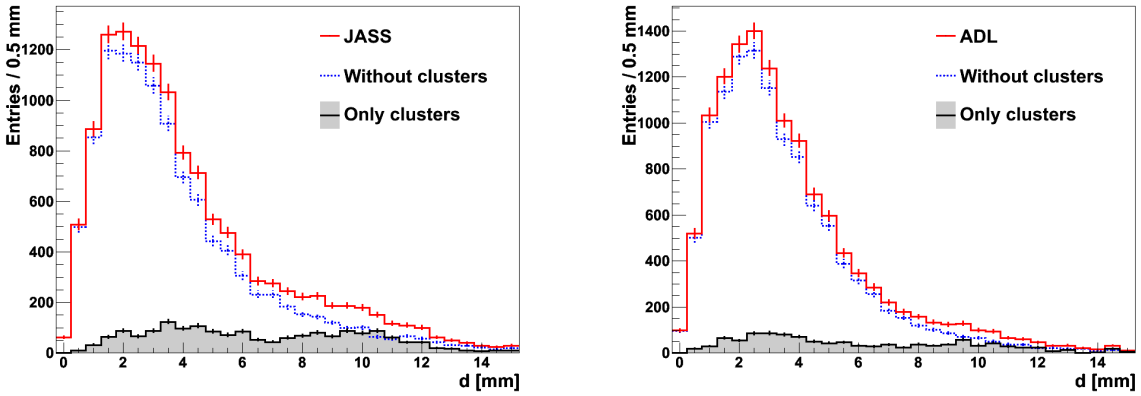

Fig. 5.14: The distance spectra for events in coincidence with the A002 detector. Due to the broad distribution of the cluster distance spectra, events in the clusters feature a deteriorated position resolution compared to events outside the clusters. The source is positioned at row 4 (segment E4) at the A006 cryostat.

segment	basis	σ(Laplace) [mm]	λ(Laplace)	χ^2/Ndf	σ(Gauss) [mm]	λ(Gauss)	χ^2/Ndf
E3	JASS	1.3	0.17	4.0	1.5	0.22	4.9
	ADL	1.2	0.04	3.8	1.5	0.10	3.7
E4	JASS	0.9	0.23	2.8	1.2	0.25	2.6
	ADL	1.0	0.11	2.0	1.3	0.13	2.6

Tab. 5.4: Position resolution of single interactions in the A006 crystal obtained with a two-parameter fit. The annihilation γ-rays are detected in the A002 and the A006 crystal. The fit is performed using the reconstructed barycenter in the Compton segment of the A006 crystal and the segment center in the A002 crystal. λ describes the fraction of the random events which corresponds to the clusters.

smearing distribution, introduced in sec. 4.1.2, is used again. It consists of a Gaussian or Laplace distribution with an additional random distribution. However, contrary to sec. 4.1.2, the random distribution does not describe escaping positions but the badly reconstructed interaction positions in the clusters. Thus, a two-parameter fit analogously to sec. 4.1.2 has to be performed. Its results are summarized in tab. 5.4. The goodness of fit of the two-parameter fits is much better than the results of the one-parameter fit. As expected the fraction of the random events is higher for the JASS signal basis than for the ADL basis because the clusters are much more dominant in the JASS basis.

Possible reasons for the clusters

It is possible that the clusters correspond to a region in the crystal which is badly modeled in the calculation of the pulse shapes. As an example the actual space charge distribution can feature a deviation from the assumed value in pulse shape simulation. Furthermore, it can happen that the crosstalk is not properly corrected resulting in a clustering of the reconstructed interaction points. These two explanations would also be consistent with the observation of the one hit-segment analysis as the clusters are also slightly present there (c.f. figs. C.1 and C.2). Additionally, the currently implemented PSA algorithm (c.f. sec. 3.2.2) leads to additional errors if it has to deal with two hit segments. Nevertheless, on the basis of the current measurement it is not possible to determine the true cause of the clusters.

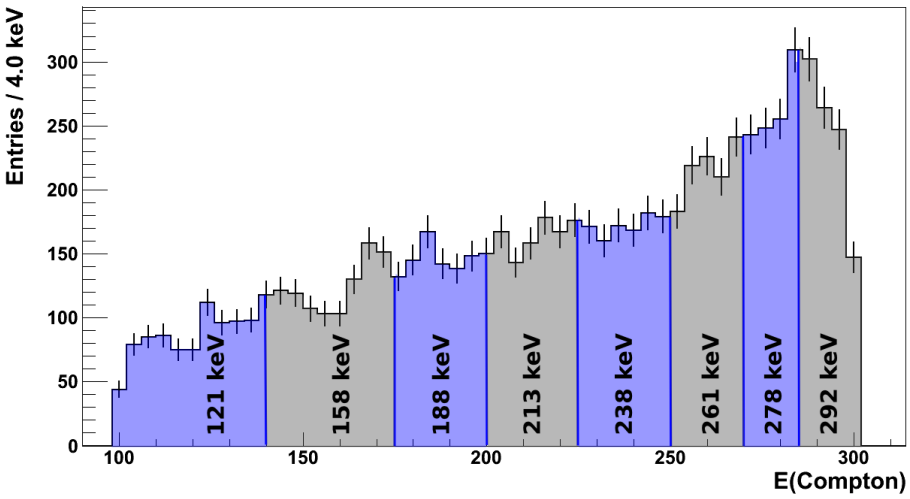

Fig. 5.15: Energy spectrum of the reconstructed barycenters in the A006 crystal of the combined analysis. Additionally, the intervals with their mean values are displayed which are used to determine the energy dependence of the positions resolution.

5.4 Energy Dependence of the Position Resolution

One important factor of the PSA position resolution is its energy dependence. Generally, it is assumed that the position resolution is inversely proportional to the square root of the deposited energy E in the interaction point [3]

$$\sigma(E) = \sigma_0 \sqrt{\frac{511\,\mathrm{keV}}{E}}, \tag{5.1}$$

To verify eq. (5.1) it is essential to study reconstructed interaction positions featuring a broad energy range. With Compton scatterings of the annihilation γ-rays of ^{22}Na energies up to 300 keV are accessible (c.f. event selection described in sec. 3.3.2). The analysis is based on the combined analysis of the asymmetric test measurement (c.f. sec. 5.3). However, the energy dependence is only determined for the events in coincidence with the A003 crystal as these reconstructed interaction points in the A006 detector do not feature the clustering mentioned in sec. 5.3. Furthermore, due to the highest statistics only the source position at row four of the A006 crystal is analyzed. Additionally, the energy spectrum of the reconstructed barycenters in the A006 crystal is divided into small intervals. This is visualized in fig. 5.15. In one interval it is assumed that the energy is constant. It is equivalent to the average energy of interval (c.f. fig. 5.15). Finally, the one-parameter fit can be performed for each energy interval separately assuming an energy independent position resolution σ. The results of the fits are shown in fig. 5.16 for a Gaussian and a Laplace smearing distribution. As expected the position resolution improves with increasing energy. For a quantitative check of the assumed energy dependence of the position resolution, the obtained resolutions are fitted with eq. (5.1). The best fit is also included in fig. 5.16. The final fit parameters σ_0 are summarized in tab. 5.5. These values agree quite well with the values given in tab. 5.3 as they are within the fluctuations seen in fig. 5.16.

5.5 Compton Scattering from the Near into a Far Detector

Until now, the position resolution of single interaction points are studied by selecting Compton scatterings from one segment into a neighboring segment of the same crystal. Thus, the

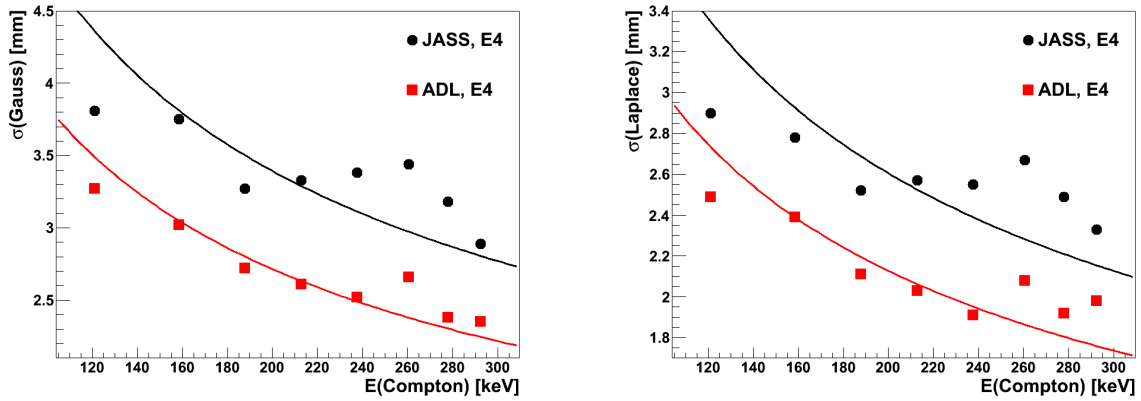

a) b)

Fig. 5.16: Energy dependence of the position resolution in the A006 detector. The source is positioned at segment E4 at the wall of the A006 cryostat. The second annihilation γ-ray is detected in the A003 crystal.

smearing distribution	σ_0(JASS) [mm]	σ_0(ADL) [mm]
Gauss	2.1	1.7
Laplace	1.6	1.3

Tab. 5.5: Fit results of fig. 5.16. The fit parameter σ_0 of eq. (5.1) is shown. It differs only in 0.2 mm from the results of tab. 5.3.

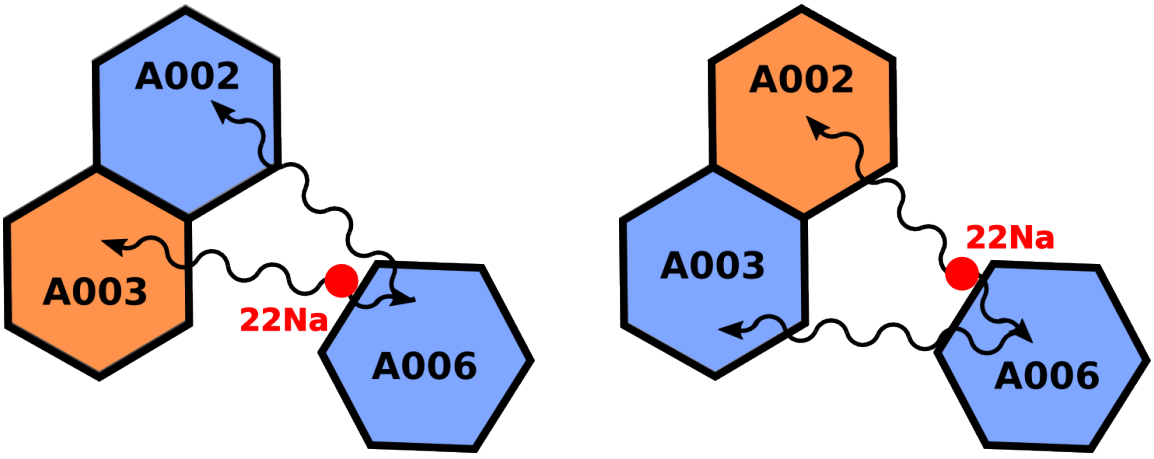

a) b)

Fig. 5.17: Scattering paths of the annihilation γ-rays for the event selection in sec. 5.5.

obtained position resolution depends not only on the quality of the pulse shape basis but also on the performance of the PSA algorithm as it has to deal with more than one hit segment (c.f. sec. 3.2.2). To reduce the influence of the PSA algorithm on the position resolution a different analysis method is needed which allows to select single hits and features only one hit segment in the crystal. Therefore, this section deals with Compton scatterings from one crystal (A006) into another crystal (A002 or A003). In terms of the asymmetric test measurement this means that a backscattering of one annihilation γ-ray from the A006 to the A002 (A003) is considered. The second annihilation γ-ray is detected in coincidence in the remaining detector A003 (A002). These two possibilities are visualized in fig. 5.17.

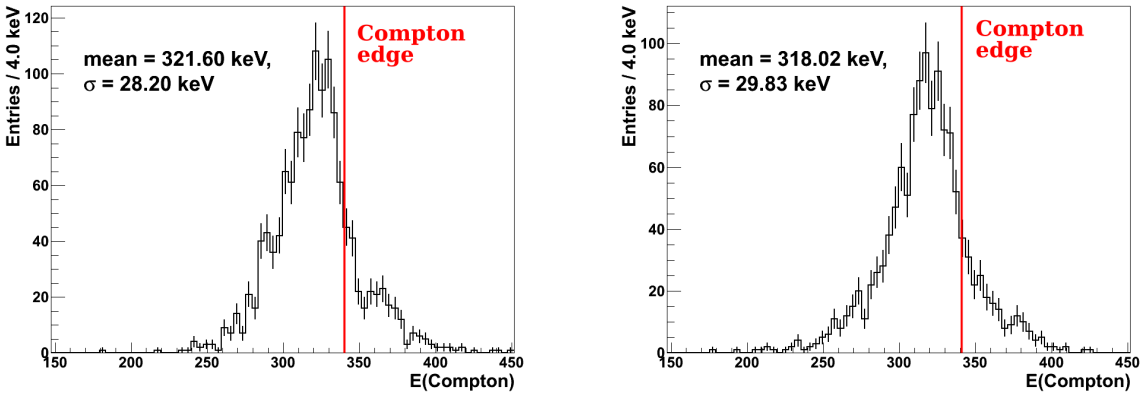

a) Scattering from A006 in A002 **b)** Scattering from A006 in A003

Fig. 5.18: Energy spectra of the reconstructed barycenters in the A006 crystal which pass the event selection of sec. 5.5.

Event selection

Thus, the selected events have to fulfill the following conditions: Each of the three crystals must have exactly one hit segment with energy depositions according to (c.f. fig. 5.17 a) / b))

$$E(\text{A002 / A003}) + E(\text{A006}) \approx 511\,\text{keV} \text{ and } E(\text{A003 / A002}) \approx 511\,\text{keV}. \tag{5.2}$$

However, contrary to the selection of Compton scattered events in sec. 3.3.2, a misidentification of the γ-ray scattering path is not possible due to the geometry. Therefore, no look-up table is necessary. The ratio between Compton scattered events with one interaction point in the A006 detector and selected events is about 65%. Thus, the performance of the selection cuts is quite similar to the cuts introduced in sec. 3.3.2. Therefore, the obtained resolutions in this section are comparable to the resolutions in secs. 5.3 and 5.4. If an additional cut on the Compton edge is considered $E(\text{A006}) < 340\,\text{keV}$, the ratio increases to about 79% as only events with multiple interaction points in the A006 segment can exceed the Compton edge at 340 keV.

Position resolution

This analysis deals with backscattered γ-rays. Thus, it is likely that the reconstructed barycenters in the A006 segment have a sharp energy near the Compton edge $E_{\text{Compton edge}} = 340\,\text{keV}$. This is confirmed in fig. 5.18 showing the deposited energy in the A006 crystal for the selected events. As a result, the position resolution in the Geant4 simulation need not to be energy dependent. It is determined by a one-parameter fit of the distance spectrum obtained with the reconstructed barycenters in the A006 crystal and the segment center of the segment which detects the second annihilation γ-ray. The resulting position resolutions are summarized in tabs. 5.6, 5.7 and fig. 5.19. Comparing the results with and without the additional energy cut on the Compton edge, they coincide quite well. Furthermore, the performance of the JASS and the ADL basis are similar. All resolutions are within the requirements of AGATA as their FWHM is less than 5 mm if they are interpolated to 1 MeV.

Influence of the PSA algorithm on the position resolution

The main motivation of this event selection is to reduce the influence of the PSA algorithm on the position resolution and to see the pure influence of the signal basis. But looking at the difference of the obtained resolutions of the Compton scatterings from one segment to another segment of the A006 crystal and the Compton scatterings from the A006 crystal into another crystal also the influence of the PSA algorithm on multiple hit segments can be

segment	basis	σ(Laplace) [mm] scattering in A003 / A002	χ^2/Ndf scattering in A003 / A002	σ(Gauss) [mm] scattering in A003 / A002	χ^2/Ndf scattering in A003 / A002
E3	JASS	1.2 / 1.3	2.3 / 1.7	1.5 / 1.7	4.5 / 1.1
	ADL	1.1 / 1.0	1.7 / 1.2	1.5 / 1.4	1.5 / 0.9
E4	JASS	1.1 / 1.5	2.7 / 1.4	1.4 / 2.0	3.2 / 1.4
	ADL	1.1 / 1.3	1.3 / 2.6	1.4 / 1.7	1.3 / 1.9

Tab. 5.6: Position resolutions of single interaction points in the A006 crystal. The selected events feature a backscattering from the A006 detector in an opposing detector (c.f. 5.17). An additional cut on the deposited energy in the A006 segment is not imposed.

segment	basis	σ(Laplace) [mm] scattering in A003 / A002	χ^2/Ndf scattering in A003 / A002	σ(Gauss) [mm] scattering in A003 / A002	χ^2/Ndf scattering in A003 / A002
E3	JASS	1.2 / 1.3	1.7 / 1.5	1.6 / 1.7	2.1 / 0.9
	ADL	1.1 / 1.1	1.5 / 1.3	1.4 / 1.5	1.2 / 1.5
E4	JASS	1.2 / 1.6	2.5 / 1.2	1.4 / 2.1	2.2 / 1.0
	ADL	1.1 / 1.3	1.3 / 2.2	1.4 / 1.7	1.9 / 2.1

Tab. 5.7: Position resolutions of single interaction points in the A006 crystal. The selected events feature a backscattering from the A006 detector in an opposing detector (c.f. 5.17). Furthermore, to select mainly single hit events, a cut on $E(\text{A006}) < 340\,\text{keV}$ is imposed. The results are also visualized in fig. 5.19

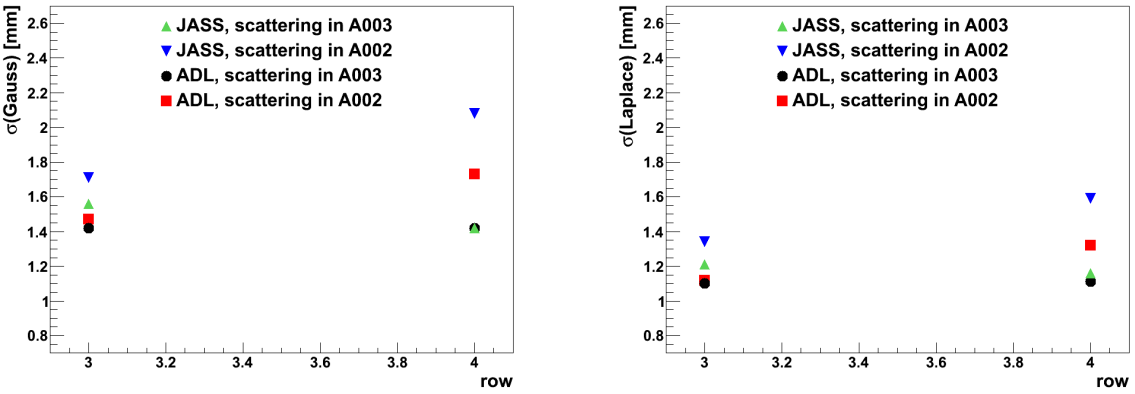

a) b)

Fig. 5.19: Obtained position resolutions of single interaction points in the A006 crystal for events featuring a backscattering from the A006 crystal to the A002 / A003 crystal.

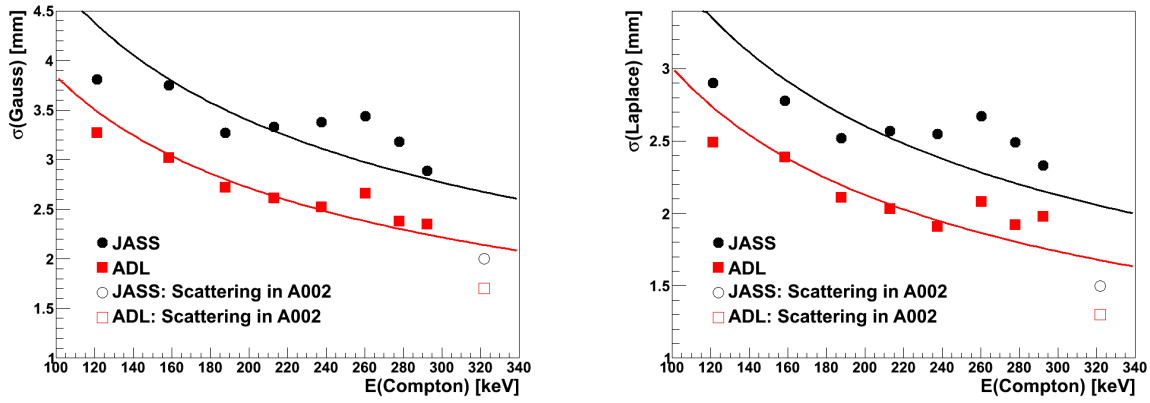

a) b)

Fig. 5.20: Energy dependence of the position resolution in the A006 detector. Both plots compare the position resolution of events featuring a Compton scattering from one segment to another segment (solid points) and of events with a Compton scattering from the A006 detector into the A002 detector (open points). The second annihilation γ-ray is detected in the A003 crystal. The source is positioned at segment E4 of the A006 detector. The drop of the position resolution at 320 keV is due to the fact that the PSA has only to deal with one hit segment.

studied. While the first analysis deals with two hit segments the latter features only one hit segment. Therefore, the performance of the PSA algorithms with multiple hit segments can be directly compared to the performance of the PSA algorithms with only one hit segment. To receive comparable results of both analyses the additional energy cut on the Compton edge is not imposed to ensure that the ratio between Compton events and selected events is the same. Fig. 5.20 compares the results of both analyses. The obtained resolutions with only one hit segment in the A006 crystal is always clearly below the best fit resulting from the resolutions with two hit segments in the A006 detector. As expected, the PSA performs worse if it has to deal with multiple hit segments. At 320 keV the PSA algorithm deteriorates the position resolution by about $\Delta\sigma = 0.5\,\mathrm{mm}$ if two hit segments occur.

Chapter 6

Discussion and Outlook

In Europe and in the USA, a new generation of γ-ray spectrometers is currently under construction: the Advanced GAmma Tracking Array AGATA and the Gamma-Ray Energy Tracking Array GRETA. The expected performance of both detector arrays is based on the concepts of γ-ray tracking, i.e. the reconstruction of γ-ray scattering paths in these highly electrically segmented HPGe crystals. An important input for the γ-ray tracking algorithms are the interaction points of the γ-rays. They are obtained by the so called pulse shape analysis (PSA) from the detected pulse shapes on the segment electrodes which are characteristic for the γ-ray interaction positions. The PSA compares a set of experimental signals from the 36 segments of one crystal to simulated signals from a pulse shape basis with known interaction positions. The best matching basis signal defines the interaction point. In its current implementation the PSA reconstructs exactly one interaction point per segment featuring an energy deposition. If there are multiple interactions in a segment, the reconstructed interaction position corresponds to their energy weighted barycenter.

In the course of this thesis a calibration experiment for the AGATA PSA was developed. It allows to determine the performance of the PSA in terms of the position resolution of the AGATA crystals and its dependence on the simulated signal bases. In this thesis, the pulse shape bases JASS and ADL of the AGATA array are compared. The position resolution was extracted exploiting the angular correlation of annihilation γ-rays e.g. from a β^+-emitter such as ^{22}Na. Both annihilation γ-rays are detected in coincidence in two opposing AGATA crystals. The analysis is based on a comparison of the experimental data to a Geant4 Monte Carlo simulation. In contrast to the experiment, the interaction points in the Geant4 simulation have a perfect position resolution. Thus, for a proper comparison, the position resolution has to be included in the simulation. Hence, the simulated interaction points are smeared around their true coordinates using two different distributions: the Gaussian distribution and the Laplace distribution. Two different event selections have been used to examine the PSA performance. By focusing on events with all energy of the annihilation γ-ray being deposited in a single segment per crystal, the spatial resolution of the reconstructed barycenter is investigated, as 511 keV γ-rays undergo around two to three interactions in germanium and only 22% of those photons are immediately absorbed by photoelectric effect in a single interaction point. To additionally study the resolution of single interactions points, events featuring a Compton scattering from one segment into a neighboring segment or even into a different crystal have been selected.

To verify the concept of the PSA calibration experiment, two test measurements were performed at the Laboratori Nazionali di Legnaro, Italy using the first installed AGATA triple clusters:

crystal	σ(Laplace) [mm] JASS / ADL	σ(Gauss) [mm] JASS / ADL
A001 and A003	1.5 / 1.2	2.0 / 1.6
A001	1.4 / 0.7	1.8 / 0.7
A003	1.5 / 1.5	2.2 / 2.1
A006 (sectors D, E)	1.1 / 1.0	1.4 / 1.4
A006 (sector E)	1.3 / 1.3	1.7 / 1.7

a) Position resolutions of the energy weighted barycenter of all interaction points of the 511 keV γ-rays.

crystal	σ_0(Laplace) [mm] JASS / ADL	σ_0(Gauss) [mm] JASS / ADL
A001 and A003	1.8 / 1.5	2.3 / 1.9
A001	1.8 / 1.3	2.1 / 1.5
A003	1.7 / 1.8	2.2 / 2.2
A006 (sectors D, E)	1.1 (0.20) / 1.1 (0.08)	1.3 (0.24) / 1.4 (0.12)
A006 (sector E)	1.7 / 1.5	2.2 / 1.9

b) Position resolutions of single interaction points. The energy dependence of the position resolution was taken into account according to $\sigma(E) = \sigma_0\sqrt{\frac{511\,\mathrm{keV}}{E}}$ with E being the energy deposited in the interaction.

Tab. 6.1: Obtained position resolutions (standard deviations σ) of the test measurements in the AGATA asymmetric crystals A001, A003 and A006 for the JASS and the ADL signal basis. The results of the A001 and the A003 crystal are determined with the symmetric setup. Contrary, the asymmetric test measurement was used to investigate the position resolution of the A006 detector. As several source positions have been measured the values in the table state only the mean position resolution. The values given in brackets correspond to the fraction of events where the PSA fails.

In the first test measurement a ^{22}Na source was positioned in the center of three mounted triple clusters. Due to the required coincident detection of the annihilation γ-rays, only two crystals (A001 and A003) can be studied with this setup. The analysis of this first data showed that positrons escaping the source mimic a bad PSA performance. Hence, they have to be explicitly considered to extract the correct position resolution. As the source was positioned in the middle of the crystals, an analysis based on the interactions points of both detectors is only sensitive to their average position resolution. Additionally, a method was developed to determine the resolution of individual crystals and their dependence on the two different signal bases, JASS and ADL. This method is based on a global multi-parameter fit which takes the interaction points in both crystals reconstructed with each basis simultaneously into account. The achieved position resolutions of the JASS and the ADL basis are summarized in tab. 6.1 for the barycenters and for single interaction positions. All resolutions fulfill the requirements of AGATA (FWHM < 5 mm for 1 MeV energy depositions) and therefore demonstrate the benefit of the AGATA PSA. Comparing the obtained values of the A001 and the A003 crystal, the JASS and the ADL basis have similar resolutions except the outstanding performance of the ADL basis in the A001 crystal. Moreover, the obtained resolutions for the single interaction points are worse than those of the barycenters. This effect could be explained by the analysis of the dataset with an asymmetric source position close to one detector.

The second, improved test measurement featured a ^{22}Na source which was additionally enclosed with aluminum to prevent the positrons from escaping the source material. An asymmetric setup was chosen with the source being located as close as possible to the A006 crystal. This allowed to determine its position resolution independently of the resolution of the other crystals. Due to the geometry and the required coincident detection of the annihilation γ-rays, different regions of the A006 crystal could be analyzed dependent on the second crystal which was used to detect the second γ-ray. Furthermore, as the source was directly positioned on the A006 cryostat, only a small part of the crystal was illuminated. Therefore, several measurements with different source positions were conducted to study the position resolutions of all segment rows of the A006 crystal separately. The average value of the obtained position resolutions of all rows are given in tab. 6.1. Like in the symmetric test measurement, the obtained resolutions of the A006 crystal are within the requirements of AGATA. The ADL basis performs slightly better in the inner segment rows whereas the JASS basis achieves a better resolution in the front and in the last row. Moreover, the analysis showed that the A006 crystal contains regions featuring a higher amount of badly reconstructed events. Their fraction is additionally given in brackets in tab. 6.1.
Furthermore, the data of the asymmetric test experiment was used to investigate the energy dependence of the position resolution. The general assumption that the position resolution is inversely proportional to the square root of the deposited energy was confirmed for the energy region $E \in [100, 300]\,\mathrm{keV}$, accessible with the $E_\gamma = 511\,\mathrm{keV}$ γ-rays, using events with a Compton scattering from one segment into a neighboring segment of the A006 crystal.
Apart from that, the geometry of the asymmetric test measurement allowed to analyze Compton scatterings from the A006 crystal into another crystal. Therefore, single interactions could be studied while the PSA had to deal with only one segment with an energy deposition per crystal. A comparison of the position resolution from these inter-crystal scatterings to the results of the intra-crystal scatterings clearly showed that multiple energy depositions per crystal deteriorate the position resolution. This degradation is solely caused by the implementation of the PSA algorithm and not by the signal basis. As this method is capable to study the multi hit performance of the PSA algorithm, new improved PSA algorithms can be easily tested with this setup, even using the data which is already collected.

The test measurements clearly illustrated that the calibration methods developed in this thesis are indeed good tools to study AGATA's PSA performance. The calibration measurement is designed as an online experiment featuring a simple setup as no modifications of the crystal positions and the electronics are necessary. These issues combined with the short measurement time make it perfectly suitable to perform the PSA calibration also during and in between beam times. Furthermore, it was shown that AGATA's goal to obtain a position resolution better than 5 mm (FWHM) for 1 MeV energy depositions is already achieved. Therefore, both signal bases JASS and ADL perform well.
To further improve the pulse shape basis, single parameters of the codes which produce the signal bases can be modified and their spacial influence can be extracted from the same experimental dataset to optimize the basis for each individual crystal. Hence, it can be systematically studied whether the JASS or the ADL mobility parameter set is more likely. Additionally, a direct comparison of the position resolutions determined with the AGATA scanning systems to the results presented in this thesis on the same crystals would be very useful to get a final validation of the signal bases.
Besides the signal bases, the PSA algorithm which compares the experimental pulse shapes to the pulse shapes of the simulated dataset needs further improvement. It still has problems to analyze more than one net charge signal at the same time leading to a degradation which is in the same order of magnitude than the position resolution. Thus, in the future, it is im-

portant to replace the time consuming grid search based PSA algorithms by faster and more sophisticated algorithms such as the Particle Swarm Algorithm (c.f. [6]).

The calibration experiment which is detailed in this thesis uses the angular correlation of annihilation γ-rays to extract the position resolution of the PSA. Alternatively, the nature of the Compton scattering process can be exploited. The Compton scattering angle θ can be determined with two different methods. First, it can be calculated from the deposited energies using the Compton formula (θ_{energy}) and second from the scattering path using the reconstructed interaction points (θ_{geo}). In case of perfect position (and energy) resolution both angles θ_{energy} and θ_{geo} coincide. Contrary, the deviation of the angles increases if the position resolution of the interaction points deteriorates. Hence, the distribution of $|\theta_{\text{geo}} - \theta_{\text{energy}}|$ is directly connected to the position resolution. This method which is very much related to γ-ray tracking has the advantage that it is not constrained to annihilation γ-rays. As a result, it is possible to use any calibration source. Hence, the position resolution of different energy regions can be determined. Thus, the energy dependence of the position resolution can be investigated using a broader energy range than in the calibration experiment with 511 keV annihilation γ-rays. However, a drawback of this method is that always two reconstructed interaction points are used to determine the position resolution. Thus, in case of a bad resolution, it is challenging to decide which interaction point is worse reconstructed. Therefore, in contrast to the calibration experiment, it is difficult to analyze different crystal regions separately. Furthermore, very good statistics are needed in this kind of experiment as the Doppler effect smears the correlation quite significantly and only interaction points at large distances should be chosen. As a result, a combined method would be optimal: Annihilation γ-rays allow to detect badly modeled regions of the signal basis in the crystal, whereas analyzing the quantity $|\theta_{\text{geo}} - \theta_{\text{energy}}|$ with different calibration sources provide the energy dependence of the position resolution for a broad energy range.

Appendix A

Comparing two Histograms with Pearson's χ^2-Test

A common method in data analysis to decide whether two histograms follow the same probability density function is Pearson's chi-square test [39], [41]. As an example the two unweighted[1] histograms h_N and h_M shall be compared. Both histograms have N_B bins in total with the same binning. The number of events in bin i of the first histogram h_N is denoted with n_i. Analogously, m_i is the number of events in the same bin i of the second histogram h_M. Thus, the total number of entries are given by

$$N = \sum_{i=1}^{N_B} n_i \quad \text{and} \quad M = \sum_{i=1}^{N_B} m_i \tag{A.1}$$

for h_N and h_M, respectively.
Assuming the hypothesis that both histograms are caused by the same probability density function is correct, the probability for a random value to be in bin i is the same for both histograms. It is denoted with p_i fulfilling the normalization condition

$$\sum_{i=1}^{N_B} p_i = 1. \tag{A.2}$$

Therefore, the number of events n_i (m_i) in bin i can be approximated by a Poisson probability distribution with the expectation value Np_i (Mp_i)

$$P_{Np_i}(n_i) = \frac{(Np_i)^{n_i}}{n_i!}\, e^{-Np_i} \quad \text{and} \quad P_{Mp_i}(m_i) = \frac{(Mp_i)^{m_i}}{m_i!}\, e^{-Mp_i}. \tag{A.3}$$

A good estimation of the probabilities p_i is achieved by adding both histograms. This results in a new histogram with a total number of events of $N + M$. Thus, p_i for each bin can be approximated by the quantity

$$\hat{p}_i = \frac{n_i + m_i}{N + M}. \tag{A.4}$$

Now the expected entries of each bin i can be written as $\hat{p}_i N$ and $\hat{p}_i M$ for the first and the second histogram, respectively. Finally, a figure of merit is defined to decide weather e.g. the histogram h_N follows the assumed distribution

$$\chi^2_N = \sum_{i=1}^{N_B} \frac{(\text{observed value - expected value})^2}{\text{expected value}} = \sum_{i=1}^{N_B} \frac{(n_i - N\hat{p}_i)^2}{N\hat{p}_i}. \tag{A.5}$$

[1] In an unweighted histogram each entry has weight one.

Hence, the figure of merit to decide if both histograms follow the same distribution reads

$$\chi^2 = \chi^2_N + \chi^2_M = \sum_{i=1}^{N_B} \frac{(n_i - N\hat{p}_i)^2}{N\hat{p}_i} + \sum_{i=1}^{N_B} \frac{(m_i - M\hat{p}_i)^2}{M\hat{p}_i} = \frac{1}{NM} \sum_{i=1}^{N_B} \frac{(Mn_i - Nm_i)^2}{n_i + m_i}. \quad \text{(A.6)}$$

It is called Pearson's χ^2-statistic. Low values indicate that the hypothesis is valid.
It can be shown that χ^2 can be approximated by the well known χ^2-distribution with $N_B - 1$ degrees of freedom. Therefore, if $\chi^2/(N_B - 1) \approx 1$ the two histograms coincide well.

Error calculation
The Pearson χ^2-tests in this thesis suffer from statistical fluctuations as the reference histogram is created with Monte Carlo techniques. Thus, the figure of merit χ^2 features a statistical error $\Delta\chi^2$. It is calculated applying Gaussian error propagation on eq. A.6:

$$\chi^2 = \sum_{i=1}^{N_B} \chi^2_i \quad \text{with} \quad \chi^2_i = \frac{(Mn_i - Nm_i)^2}{n_i + m_i} \quad \Rightarrow \quad \Delta\chi^2 = \sqrt{\sum_{i=1}^{N_B} (\Delta\chi^2_i)^2}. \quad \text{(A.7)}$$

$\Delta\chi^2_i$ reads

$$\Delta\chi^2_i = \sqrt{(\Delta N)^2 \left(\frac{\partial\chi^2_i}{\partial N}\right)^2 + (\Delta M)^2 \left(\frac{\partial\chi^2_i}{\partial M}\right)^2 + (\Delta n_i)^2 \left(\frac{\partial\chi^2_i}{\partial n_i}\right)^2 + (\Delta m_i)^2 \left(\frac{\partial\chi^2_i}{\partial m_i}\right)^2}. \quad \text{(A.8)}$$

Assuming that the entries in each bin are distributed according to Poisson's distribution, the errors are given by

$$\Delta N = \sqrt{N} \quad \text{and} \quad \Delta M = \sqrt{M} \quad \text{and} \quad \Delta n_i = \sqrt{n_i} \quad \text{and} \quad \Delta m_i = \sqrt{m_i}. \quad \text{(A.9)}$$

The derivatives in eq. (A.8) can be written as

$$\frac{\partial\chi^2_i}{\partial N} = \frac{\frac{m_i^2}{M} - \frac{M}{N^2} n_i^2}{n_i + m_i} \quad \text{(A.10)}$$

$$\frac{\partial\chi^2_i}{\partial M} = \frac{\frac{n_i^2}{N} - \frac{N}{M^2} m_i^2}{n_i + m_i} \quad \text{(A.11)}$$

$$\frac{\partial\chi^2_i}{\partial n_i} = \frac{\frac{n_i}{N} - \frac{m_i}{M}}{(n_i + m_i)^2} \cdot [2Mm_i + Mn_i + Nm_i] \quad \text{(A.12)}$$

$$\frac{\partial\chi^2_i}{\partial m_i} = -\frac{\frac{n_i}{N} - \frac{m_i}{M}}{(n_i + m_i)^2} \cdot [2Nn_i + Mn_i + Nm_i]. \quad \text{(A.13)}$$

Appendix B

β-Spectrum of ^{22}Na

According to the level scheme in fig. 2.8a) ^{22}Na undergoes a allowed β^+-decay as the transition features $\Delta J = 1$ without a parity change. The deviation of the β-spectrum of ^{22}Na follows the approach of [26].
The number of ^{22}Na decays per unit time $N(p_e)$ with positron momenta in $[p_e, p_e + dp_e]$ is given by Fermi's Golden Rule

$$N(p_e)dp_e = \frac{2\pi}{\hbar}|\langle f|\hat{H}|i\rangle|^2\rho_f, \tag{B.1}$$

where $\langle f|\hat{H}|i\rangle$ is the transition matrix element and ρ_f the density of the final states. The transition matrix element $\langle f|\hat{H}|i\rangle$ consists of the Hamilton operator of the β^+-decay and the initial and final states of the nucleus $|i\rangle$ and $|f\rangle$, respectively. In the Fermi theory the interaction can be treated point-like which corresponds to a constant transition matrix element. Therefore, the shape of the β-spectrum is solely determined by the density of the final states ρ_f which is calculated in the following.
Momentum conservation in the rest frame of the decaying proton $p \to n + e^+ + \nu_e$ leads to

$$\vec{p}_n + \vec{p}_e + \vec{p}_\nu = 0, \tag{B.2}$$

with $\vec{p}_n$, $\vec{p}_e$ and $\vec{p}_\nu$ being the momenta of the neutron, the position and the neutrino. For simplicity, it is assumed that the recoil of the daughter nucleus can be neglected and that the neutrino mass is zero. The number of all possible positron final states with momenta in $[p_e, p_e + dp_e]$, volume V and solid angle $d\Omega = 4\pi$ can be written as

$$dN_e = \frac{dN_e}{d^3p_e}\, d^3p_e = \frac{1}{(2\pi\hbar)^3/V}\, d^3p_e = \frac{V}{(2\pi\hbar)^3}\, p_e^2\, dp_e\, d\Omega = \frac{V\cdot 4\pi}{(2\pi\hbar)^3}\, p_e^2\, dp_e. \tag{B.3}$$

Analogous for the neutrino it follows[1]

$$dN_\nu = \frac{V\cdot 4\pi}{(2\pi\hbar)^3}\, p_\nu^2\, dp_\nu. \tag{B.4}$$

Thus, the number of final states is given by

$$dN_f = dN_e\, dN_\nu = \frac{V^2}{4\pi^4\hbar^6}\, p_e^2\, p_\nu^2\, dp_e\, dp_\nu. \tag{B.5}$$

[1] There is no density-of-states factor for the neutron as its momentum is defined by the positron and the neutrino momentum.

The neutrino momentum p_ν can be expressed with the Q-value corresponding to the maximal available energy of the ^{22}Na decay $E_0 = 2843\,\text{keV}$ [28]:

$$E_0 = E_e + E_\nu \quad \text{and} \quad E_\nu = p_\nu\, c \quad \Rightarrow \quad p_\nu = \frac{E_0 - E_e}{c} \quad \Rightarrow \quad \frac{dp_\nu}{dE_0} = \frac{1}{c}. \tag{B.6}$$

As a result, the density of final states is

$$\rho_f = \frac{dN_f}{dE_0} = \frac{V^2}{4\pi^4\hbar^6 c^3}\; p_e^2\; (E_0 - E_e)^2\; dp_e. \tag{B.7}$$

Therefore the number of positrons in $[p_e, p_e{+}dp_e]$ is proportional to $p_e^2\,(E_0{-}E_e)^2\,dp_e$. With the relativistic energy-momentum relationship $E_e^2 = p_e^2c^2 + m_ec^2$ the β-spectrum can be rewritten as

$$N(E_e)\; dE_e \;\propto\; p_e\; E_e\; (E_0 - E_e)^2\; dE_e. \tag{B.8}$$

Until now the decaying proton is considered as free, but in reality the whole nucleus is present. Thus, the influence of the Coulomb field of the nucleus on the emitted positron must be taken into account to determine the correct shape of the β-spectrum. This correction factor is called Fermi function $F(Z, E_e)$ and can be expressed with the following formula for allowed β^+-decays [27]:

$$F(Z, E_e) \approx 2\;(1+\gamma_0)\;\left(\frac{2p_eR}{\hbar}\right)^{2(\gamma_0-1)}\; e^{\pi\nu}\;\frac{|\Gamma(\gamma_0 + i\nu)|^2}{(\Gamma(2\gamma_0+1))^2} \tag{B.9}$$

with the abbreviation $\gamma_0 = \sqrt{1-(\alpha Z)^2}$, the fine-structure constant $\alpha = e^2/\hbar c$, $\nu = -\alpha\frac{ZE_e}{cp_e}$, the nuclear radius R and the charge Z of the daughter nucleus in terms of the elementary charge e. Furthermore, for small positron energies $E_e \leq 100\,\text{keV}$ the screening of the Coulomb field by atomic electrons is important which leads to another correction factor. The Fermi function considering both effects reads [27]

$$F^*(Z, E_e) = F(Z, E_e + V_0)\;\sqrt{\frac{(E_e/m_ec^2 + V_0)^2 - 1}{(E_e/m_ec^2)^2 - 1}}\left(\frac{E_e/m_ec^2 + V_0}{E_e/m_ec^2}\right) \tag{B.10}$$

with the shift V_0 in the potential energy of the nucleus. According to the Thomas-Fermi model the shift can be approximated by $V_0 \approx 1.13\;\alpha^2 Z^{4/3}$.

Generally, it is common to write the β-spectrum as a function of the kinetic energy $T_e = E_e - m_ec^2$ of the positron

$$N(T_e)\; dT_e \;\propto\; F^*(Z, E_e)\; p_e\; E_e\; (E_0 - E_e)^2\; dT_e. \tag{B.11}$$

The resulting β^+-spectrum of one million ^{22}Na decays is visualized in fig. 2.8 b). It has a mean energy of 216 keV and an end point energy of 546 keV. These values coincide well with [28].

Appendix C

Distributions of the Interaction Points of the 2nd Test Measurement

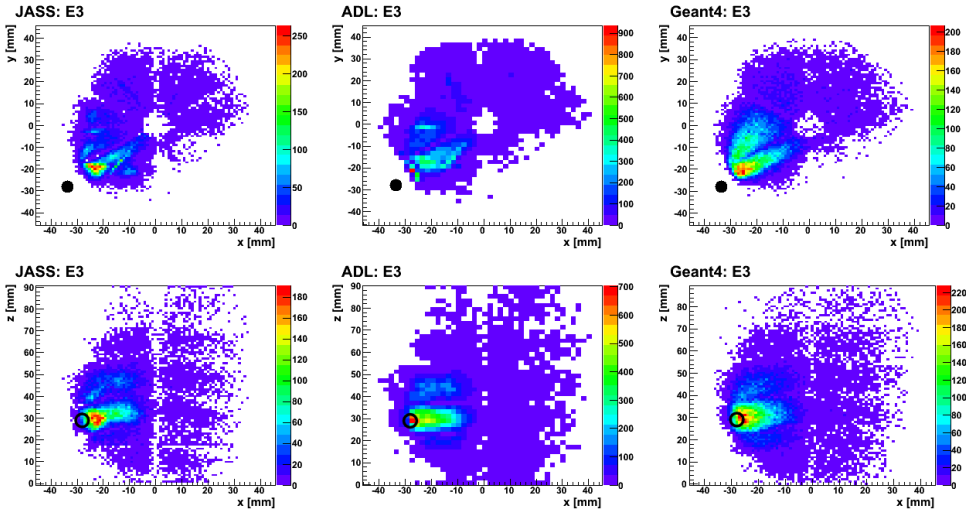

a) A006 in coincidence with A002

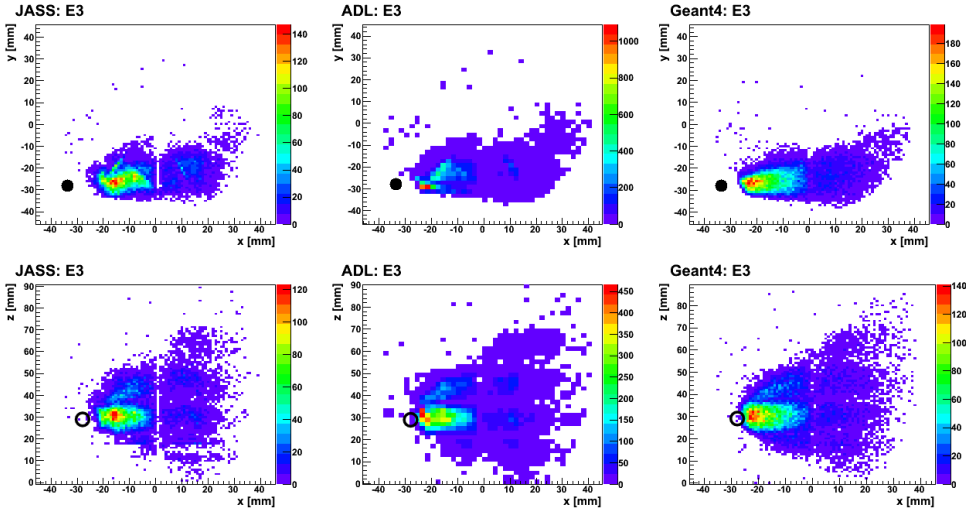

b) A006 in coincidence with A003

Fig. C.1: Spatial distributions of the interaction points using the one hit-segment analysis. The source (marked with a black circle) is positioned at the third segment row of A006.

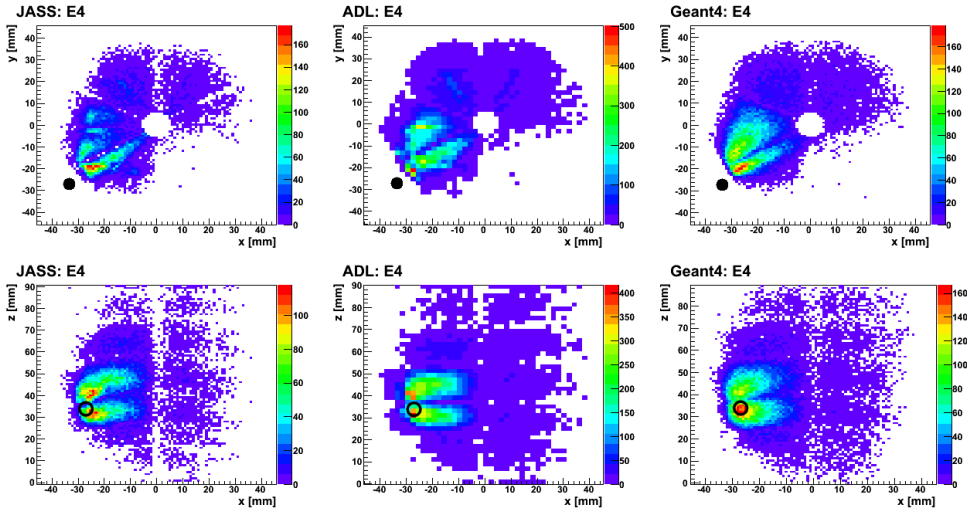

a) A006 in coincidence with A002

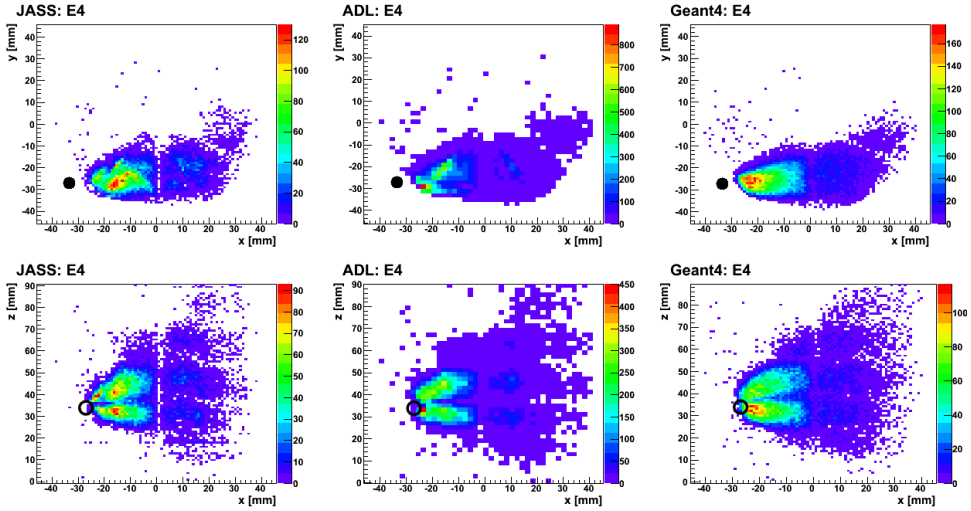

b) A006 in coincidence with A003

Fig. C.2: Spatial distributions of the interaction points using the one hit-segment analysis. The source (marked with a black circle) is positioned at the fourth segment row of A006.

Bibliography

[1] D. Bazzacco, B. Cederwall, J. Cresswell, G. Duchêne, J. Eberth, W. Gast, J. Gerl, W. Korten, I. Lazarus, R. Lieder, J. Simpson, and D. Weisshaar, "AGATA Technical Proposal," 2001. `http://www-w2k.gsi.de/agata/publications.htm`.

[2] J. Eberth and J. Simpson, "From Ge(Li) detectors to gamma-ray tracking arrays - 50 years of gamma spectroscopy with germanium detectors," *Progress in Particle and Nuclear Physics*, vol. 60, no. 2, pp. 283 – 337, 2008.

[3] F. Recchia, *In-beam test and imaging capabilities of the AGATA prototype detector*. PhD thesis, University of Padua, 2008.

[4] B. Bruyneel, "Advances in HPGe Technology: The new AGATA Triple Cluster." talk, June 2008. AGATA Workshop, Munich.

[5] J. Simpson, J. Nyberg, and W. Korten, "AGATA Technical Design Report," 2008. `http://www-w2k.gsi.de/agata/publications.htm`.

[6] M. Schlarb, *Simulation and Real-Time Analysis of Pulse Shapes from segmented HPGe-Detectors*. PhD thesis, Technische Universität München, 2009.

[7] X. Grave, R. Canedo, J.-F. Cavelin, S. Du, and E. Legay, "NARVAL a Modular Distributed Data Acquisition System with Ada 95 and RTAI," *IEEE Real Time*, 2005.

[8] "AGATA Demonstrator Inauguration at INFN, Laboratori Nazionali di Legnaro." webpage, April 2010. `http://agata.lnl.infn.it/Inaugurazione/foto/index_en.htm`.

[9] P. Reiter, "Status of the AGATA detectors." talk, November 2010. 10th AGATA Week, Lyon.

[10] G. F. Knoll, *Radiation detection and measurement*. John Wiley and Sons, 2 ed., 1989.

[11] S. Antman, D. Landis, and R. Pehl, "Measurements of the Fano factor and the energy per hole-electron pair in germanium," *Nuclear Instruments and Methods*, vol. 40, no. 2, pp. 272 – 276, 1966.

[12] Canberra, *AGATA: Encapsulated Germanium Detectors. Operating Manual.*

[13] B. Birkenbach, "Characterization of AGATA detectors." talk, March 2011. DPG Frühjahrstagung 2011, Münster.

[14] B. Birkenbach, B. Bruyneel, G. Pascovici, J. Eberth, H. Hess, D. Lersch, P. Reiter, and A. Wiens, "Determination of space charge distributions in highly segmented large volume HPGe detectors from capacitance-voltage measurements," *Nuclear Instruments and Methods in Physics Research Section A: Accelerators, Spectrometers, Detectors and Associated Equipment*, vol. In Press, Uncorrected Proof, pp. –, 2011.

[15] B. Bruyneel and B. Birkenbach, "AGATA Detector simulation Library (ADL) v.2.0," November 2008. http://www.ikp.uni-koeln.de/research/agata/index.php?show=download.

[16] B. Bruyneel, P. Reiter, and G. Pascovici, "Characterization of large volume HPGe detectors. Part I: Electron and hole mobility parameterization," *Nuclear Instruments and Methods in Physics Research Section A: Accelerators, Spectrometers, Detectors and Associated Equipment*, vol. 569, no. 3, pp. 764 – 773, 2006.

[17] L. Nelson, M. Dimmock, A. Boston, H. Boston, J. Cresswell, P. Nolan, I. Lazarus, J. Simpson, P. Medina, C. Santos, and C. Parisel, "Characterisation of an AGATA symmetric prototype detector," *Nuclear Instruments and Methods in Physics Research Section A: Accelerators, Spectrometers, Detectors and Associated Equipment*, vol. 573, no. 1-2, pp. 153 – 156, 2007. Proceedings of the 7th International Conference on Position-Sensitive Detectors - PSD-7, 7th International Conference on Position-Sensitive Detectors.

[18] F. Recchia, D. Bazzacco, E. Farnea, A. Gadea, R. Venturelli, T. Beck, P. Bednarczyk, A. Buerger, A. Dewald, M. Dimmock, G. Duchêne, J. Eberth, T. Faul, J. Gerl, R. Gernhäuser, K. Hauschild, A. Holler, P. Jones, W. Korten, T. Kröll, R. Krücken, N. Kurz, J. Ljungvall, S. Lunardi, P. Maierbeck, D. Mengoni, J. Nyberg, L. Nelson, G. Pascovici, P. Reiter, H. Schaffner, M. Schlarb, T. Steinhardt, O. Thelen, C. Ur, J. V. Dobon, and D. Weißhaar, "Position resolution of the prototype AGATA triple-cluster detector from an in-beam experiment," *Nuclear Instruments and Methods in Physics Research Section A: Accelerators, Spectrometers, Detectors and Associated Equipment*, vol. 604, no. 3, pp. 555 – 562, 2009.

[19] I. Procházka, "Positron Annihilation Spectroscopy," *Materials Structure in Chemistry, Biology, Physics and Technology*, vol. 8, no. 2, pp. 55–60, 2001.

[20] D. K. Schroder, *Semiconductor Material and Device Characterization*. John Wiley and Sons, 3 ed., 2006.

[21] S. Aydin, F. Recchia, D. Bazzacco, E. Farnea, and C. Ur, "Effective size of segmentation lines of an AGATA crystal," *Laboratori Nazionali di Legnaro, Annual Report 2007*, pp. 195–196, 2007.

[22] S.Aydin, *Performance Improvement of an AGATA Segmented Germanium Detector*. PhD thesis, University of Cukurova, 2009.

[23] The Geant4 Collaboration, "G4 — A simulation toolkit," *Nuclear Instruments and Methods in Physics Research Section A*, vol. 506, pp. 250–303, July 2003.

[24] The Geant4 Collaboration, "Geant4 developments and applications," *IEEE Transactions on Nuclear Science*, vol. 53, no. 1, pp. 270–278, 2006.

[25] E. Farnea, *AGATA Simulation Code*, April 2009. http://agata.pd.infn.it/documents/simulations/agataCode.html.

[26] D. Perkins, *Introduction to High Energy Physics*. Addison-Wesley, 4 ed., 2000.

[27] K. Siegbahn, *Alpha-, beta- and gamma-ray spectroscopy/2*. Elsevier Science Ltd, 4 ed., 1972.

[28] Laboratoire National Henri Becquerel, "^{22}Na data sheet," 2009. http://www.nucleide.org/DDEP_WG/Nuclides/Na-22_tables.pdf.

[29] PSA and Characterization Team, "Evo meeting," April 2010.

[30] B. Bruyneel, P. Reiter, A. Wiens, J. Eberth, H. Hess, G. Pascovici, N. Warr, and D. Weisshaar, "Crosstalk properties of 36-fold segmented symmetric hexagonal HPGe detectors," *Nuclear Instruments and Methods in Physics Research Section A: Accelerators, Spectrometers, Detectors and Associated Equipment*, vol. 599, no. 2-3, pp. 196 – 208, 2009.

[31] F. Recchia. private communication, January 2011. University of Padua.

[32] "PSA team meeting," November 2010. 10th AGATA week, Lyon.

[33] M. Berger, J. Hubbell, S. Seltzer, J. Chang, J. Coursey, R. Sukumar, D. Zucker, and K. Olsen, "NIST Standard Reference Database 8: XCOM: Photon Cross Sections Database," 2010.

[34] F. Recchia, D. Bazzacco, E. Farnea, R. Venturelli, S. Aydin, G. Suliman, and C. Ur, "Performance of an AGATA prototype detector estimated by Compton-imaging techniques," *Nuclear Instruments and Methods in Physics Research A*, vol. 604, pp. 60–63, June 2009.

[35] N. Hammond, T. Duguet, and C. Lister, "Ambiguity in gamma-ray tracking of two-interaction events," *Nuclear Instruments and Methods in Physics Research A*, vol. 547, pp. 535–540, Aug. 2005.

[36] F. James, *MINUIT-Function minimization and error analysis.* CERN, Computing and Networks division. CERN Program Library Long Writeup D506.

[37] I. Antcheva, M. Ballintijn, B. Bellenot, M. Biskup, R. Brun, N. Buncic, P. Canal, D. Casadei, O. Couet, V. Fine, L. Franco, G. Ganis, A. Gheata, D. G. Maline, M. Goto, J. Iwaszkiewicz, A. Kreshuk, D. M. Segura, R. Maunder, L. Moneta, A. Naumann, E. Offermann, V. Onuchin, S. Panacek, F. Rademakers, P. Russo, and M. Tadel, "ROOT – A C++ framework for petabyte data storage, statistical analysis and visualization," *Computer Physics Communications*, vol. 180, no. 12, pp. 2499 – 2512, 2009. 40 YEARS OF CPC: A celebratory issue focused on quality software for high performance, grid and novel computing architectures.

[38] W. Stahel, *Statistische Datenanalyse. Eine Einführung für Naturwissenschaftler.* Vieweg+Teubner, 4 ed., 2002.

[39] T. S. Ferguson, *A Course in Large Sample Theory.* Chapman and Hall/CRC, 1 ed., 1996.

[40] W. H. Press, B. P. Flannery, S. A. Teukolsky, and W. T. Vetterling, *Numerical recipes in C (2nd ed.): the art of scientific computing.* New York, NY, USA: Cambridge University Press, 1992.

[41] N. D. Gagunashvili, "Comparison of weighted and unweighted histograms," *ArXiv Physics e-prints*, May 2006.

Danksagung

Zuallererst möchte ich mich bei Herrn Prof. Reiner Krücken bedanken, der mich sehr freundlich am Lehrstuhl aufgenommen hat und mir diese interessante Diplomarbeit ermöglicht hat.
Ein großer Dank geht an Dr. Roman Gernhäuser für die erstklassige Betreuung. Ihm sind durch seine stets offene Bürotür, seiner vielen guten Ideen und durch die durchaus mal längeren Diskussionen über meine Analyse viele wichtige Punkte meiner Diplomarbeit zu verdanken.
Besonders danken möchte ich auch Dr. Michael Schlarb für die Einführung in Narval, JASS, die guten Vorschläge für meine Datenauswertung und das Korrekturlesen. Auch für die schönen Abendessen in Legnaro möchte ich mich bei ihm bedanken.
Ohne Dino Bazzacco, Damiano Bortolato, Enrico Farnea und Francesco Recchia von der italienischen AGATA-Gruppe in Legnaro, die meine Messungen durchgeführt haben, wäre diese Diplomarbeit auch nicht möglich gewesen. Bedanken möchte ich hierbei v.a. für die Durchfürhung meiner zweiten Messung zwischen Weihnachten und Neujahr.
Für das Herunterladen der Messdaten von Italien möchte ich mich auch bei unserem Admin Dr. Ludwig Maier bedanken, der sofort ein Skript für mich geschrieben hat, das mir die Arbeit wesentlich erleichtert hat.
Ein großes Dankeschön geht auch an Kathi, Michael, Max, Josef, Konrad und alle anderen E12 Mitarbeiter für die vielen unterhaltsamen Kaffeepausen, Abende in München und in Münster und Grillabende am Garchinger Weiher. Besonders möchte ich hier auch Janina danken für die zahlreichen gemeinsamen Mittagessen in der Mensa mit anschließender ausfürlicher Kaffeepause und für die vielen aufmunternden Worte, wenn die Arbeit nicht wie gewünscht voran ging.
Danken möchte ich auch "unserem" Büro für die gute Atmosphäre, wodurch ich mich von Anfang an sehr wohl gefühlt habe.
Finally, I want to thank Dr. Aldo Saavedra of the University of Sydney for teaching me a lot of ROOT tricks and introducing me Pearson's χ^2-test which is now an important part of my analysis.
Robert Lang danke ich für unsere langjärige Freundschaft mit vielen netten Ratsch-, Ess- und Videoabenden sowie dafür, dass er sich nie gescheut hat auch mal mit mir Standard und Latein zu tanzen.
Ein riesiges Dankeschön geht auch an meine Eltern, die mich jederzeit während meines Studiums und der Diplomarbeit unterstützt haben. Danke auch für das fleißige Korrekturlesen dieser Arbeit auf Rechtschreibfehler und für die super Versorgung mit selbstgemachter Lasagne und Kuchen.
Meinem kleinen Bruder Maxi möchte ich auch noch danken für die nötige Ablenkung, den Süßigkeiten-Nachschub und den regelmäßigen Abholservice von der S-Bahn.
Der größte Dank gilt meinem Freund Dominik Hellgartner, der mich seit der 13. Klasse in allen Lebenslagen immer unterstützt und ohne den die letzten Jahre noch nicht mal halb so schön gewesen wären.